# IONOTHERMAL SYNTHESIS OF METAL ALUMINOPHOSPHATES

**Mazlina Musa**

**A Thesis Submitted for the Degree of PhD**
**at the**
**University of St Andrews**

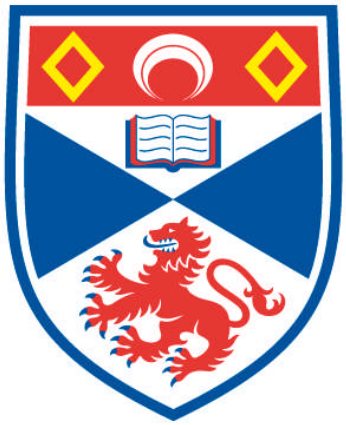

**2014**

# Declaration

I, Mazlina Musa, hereby certify that this thesis, which is approximately 35,316 words in length, has been written by me, that it is the record of work carried out by me and that it has not been submitted in any previous application for a higher degree.

I was admitted as a research student in November 2009 and as a candidate for the degree of Ph.D. in November 2010; the higher study for which this is a record was carried out in the University of St Andrews between 2009 and 2013.

Date: Signature of candidate

I hereby certify that the candidate has fulfilled the conditions of the Resolution and Regulations appropriate for the degree of Ph.D. in the University of St Andrews and that the candidate is qualified to submit this thesis in application for that degree.

Date: Signature of supervisor

In submitting this thesis to the University of St Andrews we understand that we are giving permission for it to be made available for use in accordance with the regulations of the University Library for the time being in force, subject to any copyright vested in the work not being affected thereby. I also understand that the title and the abstract will be published, and that a copy of the work may be made and supplied to any bona fide library or research worker,

that my thesis will be electronically accessible for personal or research use unless exempt by award of an embargo as requested below, and that the library has the right to migrate my thesis into new electronic forms as required to ensure continued access to the thesis. I have obtained any third-party copyright permissions that may be required in order to allow such access and migration, or have requested the appropriate embargo below.

The following is an agreed request by candidate and supervisor regarding the electronic publication of this thesis:

Access to printed copy and electronic publication of thesis through the University of St Andrews.

Date: Signature of candidate

Date: Signature of supervisor

## Courses Attended

The School of Chemistry at the University of St Andrews requires that a postgraduate attend a number of taught courses. The courses attended were:

| | |
|---|---|
| Crystallography | Professor Philip Lightfoot |
| Solid State NMR | Professor Sharon Ashbrook |

# Acknowledgement

Alhamdulillah, all praises to ALLAH for giving me strength and patience to complete this thesis. First of all, I would like to express my sincere thanks to my supervisor Professor Russell Morris for giving me the opportunity to be involved in his research group. I really appreciate his excellent guidance, expertise, understanding and unlimited patience throughout my PhD study, without him it would have been very difficult for me to accomplish this work.

I am thankful for all the great people in REM's group that have helped me over the last 4 years, especially to Dr. Paul Wheatley for his patient answering a lot of questions since I started my project. Big special thanks go to Dr. Farida Himeur Aidoudi, Dr. Laura McCormick and Matthew McPherson for reading through several chapters of this thesis. Thanks also go to Dr. Alistair McKinlay, Dr. Mohamed Infas Haja Mohideen, Dr. Phoebe Allan, Dr. Dave Aldous, Dr. Stewart Warrender, Dr. Catherine Renouf, Mr. Yuyang Tian, Ms. Morven Duncan and Mr. Damiano Cattaneo for their help, kindness and become good friends along the way of this study.

I also would like to thank Professor Sharon Ashbrook for solid state NMR data collected at St. Andrews. Special thanks also must be given to Mr. Daniel Dawson for his time, kindness and helping out so much in collecting and discussion of the solid state NMR data. Thanks also go to the technical staffs at School of Chemistry, St. Andrews University; Mrs. Sylvia Williamson (TGA), Mrs. Melanja Smith (NMR), Mr. Ross Blackley (SEM/EDX), Mr. George Anthony and Mr. Bob Cathcart.

Very special thanks to Sultan Idris Education University (UPSI) that gave this opportunity to me to pursue PhD study at St. Andrews University. To the sponsor of my study; Ministry of Higher Education Malaysia (MOHE) thanks very much for the financial support.

My deepest and gratitude goes especially to my beloved parents and family for being supportive all the time no matter what happened, also for their sacrifices throughout the period of my study. Last but not least, to all my adorable friends; Dr. Nurul Izzaty, Dr. Nurul Liyana, Dr. Vivi Andasari, Dr. Muzirah, Dr. Nadiawati, Dr. Noorshida, Dr. Aimi Hamizah, Dr. Atiqah, Dr. Misbah, Dr. Azra, Dr. Hexiang, Mrs. Rozita, Mrs. Nozriah, Ms. Siti Sabariah and all KMD friends, thank you so much for your joyfulness, motivation support and encouragement throughout of my study life in UK.

# Abstract

The aim of this thesis was to synthesise CoAPO-34 and FeAPO-34 using ionothermal synthesis in the presence of organic amines. Using this method provides an alternative route to prepare such materials under low pressure instead of the higher pressure associated with hydrothermal or solvothermal synthesis. Both materials have chabazite (CHA) topology and they are known to act as catalysts.

CoAPO-34 was ionothermally prepared using 1-ethyl-3-methylimidazolium bromide (EMIMBr) in presence of 1, 6-hexadiamine (HDA). This study has found that when the synthesis was carried out without HDA, AlPO-11 was preferentially obtained instead of CoAPO-34. Broad line signals which appear between 2000 to 5000 ppm in both spin-echo $^{31}$P NMR spectra of as-synthesised and calcined CoAPO-34 confirm that the $Co^{2+}$ ions have been successfully incorporated within the framework of the material.

FeAPO-34 was synthesised under ionothermal conditions using 1-ethyl-3-methylimidazolium chloride in the presence of ethylenediamine (EDA). In the absence of EDA, the synthesis has produced AlPO-34 instead of FeAPO-34. Broad line signals that appear between 1000 to 14000 ppm in spin-echo $^{31}$P NMR spectra of both as-synthesised and calcined FeAPO-34 are direct evidence of isomorphous substitution of framework aluminum by Fe(II) or Fe(III).

Another aim of this study was to explore the ionothermal synthesis of copper containing aluminophoshate of DNL-1 (Cu/DNL-1). This material was attractive to explore because it contains 20 ring extra-large pores and Cu(I) species in the channels of the framework, potentially giving material the ability to simultaneous store NO and to generate NO from $NO_2^-$ anions.

Cu/DNL-1 was successfully prepared under ionothermal conditions using EMIMBr and HDA. Without HDA in the synthesis, AlPO-11 was obtained. In this material, copper ions were not incorporated in the Cu/DNL-1 skeleton framework. This was confirmed by absence of broadline signal at >500 ppm in spin-echo $^{31}P$ NMR spectrum of the sample. The copper ions are expected to be present as extra-framework cations. Extra-framework Cu(I) species that were formed by high temperature calcination of Cu/DNL-1 are active to produce NO from $NO_2^-$. Therefore, the calcined Cu/DNL-1 can be used to simultaneously store and produce NO from nitrite. This has the potential to significantly extend the lifetime of gas delivery in the material to prevent thrombus formation.

# Table of Contents

# CHAPTER 1

# INTRODUCTION

## 1.1: Zeolites

Zeolite based molecular sieves are a vital inorganic material group in industrial application used as ion exchangers, catalysts and adsorbents.[1] These porous material have been known almost 250 years as crystalline aluminosilicates constructed from corner -sharing $TO_4$ tetrahedra (T = silicon or aluminium atom) T= Al/P are also common, although they are not strictly zeolites .[2] The general formula of aluminosilicate zeolite can be represented as follows:

$$\mathbf{M_{y/z}[(SiO_2)_x.(AlO_2)_y].qH_2O}$$

Where **x** and **y** are integer for equal or greater than 1, **M** is cation and **q** is the number of water molecules in each unit cell.[3]

Zeolites are important in catalysis because of the formation of BrØnsted acid sites (shown in Figure 1.1). Every time an Al replaces a Si in the structure; a negative charge is produced, which must be balanced by cation. This can be a proton ($H^+$) as shown in Figure 1.1, or other cations such as $Na^+$, $Ca^{2+}$ and etc.[2]

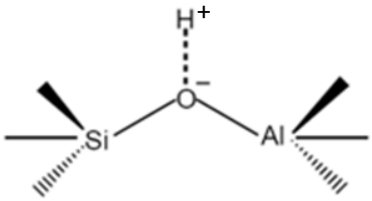


Figure1.1 Basic chemical structure of the BrØnsted acid site zeolite aluminosilicate [4]

The history of zeolites began in 1756 when the Swedish mineralogist Axel Fredrick Cronstedt observed the rapid heating of stilbite, which produced large amounts of steam from the mineral that absorbed water. He named the stone zeolite from the Greek words 'zeo' meaning 'boil' and 'lithos' is 'stone'.[2] Since then, approximately 40 natural zeolite frameworks[2] and 213 unique structures are identified.[5]

Natural zeolites are formed when the volcanic rocks (solidified lava) and ash layers crystalized under reaction with alkaline/ saline lake or ground water.[6] The most common natural zeolites are chabazite, offretite, faujasite and mordenite.[3] Naturally occurring zeolites are contaminated by various degrees of metals, minerals, quartz and other zeolites. Owing to this natural zeolites are often excluded from many essential commercial applications where purity and uniformity are accentuated. However, natural zeolites are often preferred for use in environmental application where they can be employed in the simpler manner where the raw material just crushed into the powder. Zeolites are also used in widespread application as a filler in cement, in paper, in fertilizer and soil conditioner and as dietary supplements in animal husbandry.[6]

Synthetic zeolites were first made by Barrer in late 1940 using higher temperature and pressure to synthesis of modernite. The discovery inspired Milton (1959) and Breck (1964) to synthesis zeolite A, X and Y under milder condition using much lower temperature and pressure than

earlier. In 1954 a number of synthetic zeolites were introduced by Union Carbide as new industrial materials for separation and purification process.[7] Many of new synthetic zeolites with no natural counterpart have larger pores size and higher volume capacity rather than most known natural zeolites. Zeolites with larger pore size have advantages in that larger molecules can be used as reactants.[8]

Zeolite frameworks are based on individual tetrahedral unit ($TO_4$) called a 'Primary building unit (PBU). The PBUs are link together to form secondary building units (SBUs) which consist of n-ring structure. Figure 1.2 shows 20 kinds of SBUs that have been found in tetrahedral frameworks.[9] Each corner in SBUs represent T atoms belonging to $TO_4$ where oxygen (not plotted for clarity) are found near at the middle of the lines joining each pair of T.

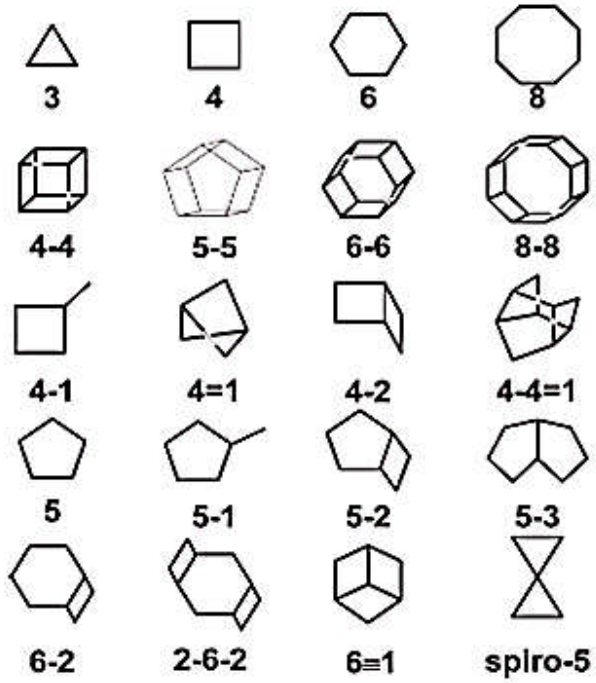


Figure 1.2: Secondary building units (SBUs) and their symbols [9]

SBUs can be linked to form 'tertiary building units' (TBUs). Further connecting TBUs generate large polyhedral building block to form a characteristic pore system. Figure 1.3 shows an example, where the β-cage (sodalite cage) is built by six 4-rings and eight 6-rings. It is a common unit joined together in different arrangements to produce a variety of frameworks e.g SOD, LTA, EMT and FAU.[10] The structure Commission of the International Zeolite Association (IZA-SC) has assigned the three letter codes to all unique frameworks of zeolite topologies.[2]

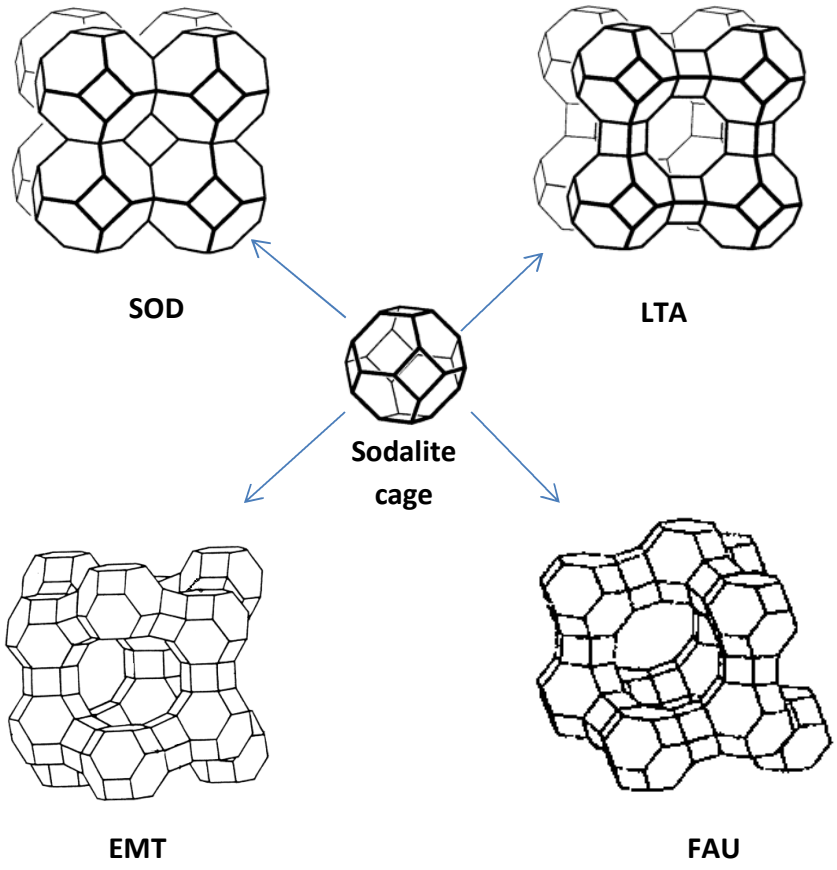


Figure 1.3: Schematic of Sodalite cage frameworks [11]

## 1.2: Applications of zeolites

Zeolites have unique properties including good thermal stability, acidity, ion-exchange capacity, uniform molecular sized channels, adsorption for gas or vapor and catalytic properties. Owing to these properties, zeolites are used widely in many applications such as environmental treatment, laundry detergents, oil refining and petrochemical industries, adsorption, gas separation, agriculture and horticulture.[12] Generally, the main uses of zeolites can be categorized into three functional classifications: ion exchange, catalysis and adsorption-separation.

### 1.2.1: Ion exchange applications

Cation exchange properties of traditional aluminosilicate zeolites arise from the isomorphous positioning of aluminium in tetrahedral coordination within their Si/Al frameworks. This imposes a net negative charge on the framework counterbalanced by cations held within the cavities and channels. This is said to create facile cation exchange "lubricated" by the water molecules also present in the voids within the framework. This certainly is the case for zeolites with open frameworks but in the more narrow-pored frameworks, such as natrolite, cation replacement is slow and difficult.[13]

Cation exchange is exploited in water softening, where alkali metals such as $Na^+$ or $K^+$ in zeolite framework are replaced by $Ca^{2+}$ and $Mg^{2+}$ ions from water. Many commercial washing powders thus contain substantial amounts of zeolites that enhance washing efficiency. LTA is the subject of the largest scale production of synthetic zeolites for use as "builders" in domestic and commercial detergents to remove the calcium and magnesium "hardness".[14]

The unique ion exchange properties of zeolites can also be used for cleaning up of commercial waste water containing heavy metals and nuclear effluents containing radioactive isotopes. In a similar way zeolites can absorb ions and molecules and thus act as a filter for odor control and toxin removal.[13]

## 1.2.2: Adsorption and separation applications

The shape-selective properties of zeolites are the basis for their use in molecular adsorption and separation. The ability preferentially to adsorb certain molecules, while excluding others, has opened up a wide range of molecular sieving applications, for example, an everyday laboratory use as drying agent for organic solvents.[15] This ability to selectively adsorb molecules also allows zeolites to separate gaseous mixtures, for instance, gases containing $CH_4$ and $CO_2$ can be separated by common zeolites such as NaX and CaA.[16] The removal of $CO_2$ from the $CO_2/CH_4$ gas is an important process for industries in upgrading the gas because the presence of $CO_2$ can reduce the heating value and leads to pipeline corrosion in the presence of water.[16, 17]

Water pollution by various organic materials has been a serious environmental problem. Adsorption is one effective technology for wastewater treatment. Zeolites with higher surface area can be used as adsorbent for the removal of organic material from water. For example, MCM-22 can be used to adsorb alcohols from water solutions; enhanced adsorption was obtained for alcohols with longer alkyl chains.[18] This material is also an effective adsorbent for a basic dye, methylene blue, removed from wastewater.[19] Zeolite Y is an efficient adsorbent in the removal of antibiotic contaminants; erythromycin (ERY), carbamazepine (CBZ) and levofloxacin (FLX) in wastewater remediation.[20]

The production of $O_2$ and $N_2$ from air using synthetic zeolites and pressure swing adsorption (PSA) cycles are increasingly important in industrial air separation. In air separation, CaA and NaX zeolites are mainly used as adsorbents. Since the $N_2$ molecule has larger quadrupole moment than $O_2$, it interacts more strongly with extra-framework cations in the zeolites, giving rise to localisation of $N_2$ molecules near accessible cations in contrast to a more diffused $O_2$ distribution. This indicates that cations in the zeolite play a crucial role in the $N_2/O_2$ selectivity.[21] On the other hand, $Li^+$ ion-exchanged X and A zeolites also have higher $N_2/O_2$ selectivity as well as higher $N_2$ capacities.[22] This is because of the smaller ionic radius of $Li^+$ possesses higher charge density and hence higher polarizing power. PSA using LiX zeolites is a highly efficient technology for air separation and is being used in industry.[21]

## 1.2.3: Catalysis applications

Zeolites are extremely useful as solid acid catalysts (e.g., ZSM-5, FER)[23] in many refinery processes including crude oil cracking, isomerisation and hydrocarbon synthesis. Cracking is responsible for the production of gasoline from low-value heavier fractions and isomerization is important for production of *iso*-alkanes or removal of undesired normal or slightly branched alkanes in fuels (e.g., diesel), increasing the octane number.[24, 25]

On the other hand, zeolites also serve as oxidation or reduction catalysts, often after metals have been introduced into the framework, for instances, titanium ZSM-5 zeolite is used in the production of caprolactam[26] and copper containing zeolites are used in the removal of NO from auto-exhaust streams.[27-33]

## 1.3: NO storage and releasing-materials

A number of materials have been proposed as delivery of exogenous nitric oxide (NO) where it may important for medical therapies. Using nitric oxide as a therapy would enable wound-healing times on chronic wounds (such as diabetic ulcers) to be reduced by several days.[34] It also could be used to coat medical instruments to prevent clotting after invasive surgery.[35] A common method of achieving such delivery method is store the gas inside the storage materials such as zeolites, Metal Organic Frameworks (MOFs), polymer etc. Nitric oxide will be discussed in much detail in section 1.12.

## 1.3.1: NO storage and releasing - zeolites

The negative charged framework of zeolites is compensated by cations such as $Na^{+}$, $Ca^{2+}$, $Cu^{2+}$, $Co^{2+}$ and etc . The presence of extra-framework cations in the zeolite can interact with guests and sometimes help to convert the guest into an intermediate or final product.

Interactions of NO with transition metal ion exchanged zeolites are well known in catalytic and separation studies. Most researches studies focus on the destruction of NO, particularly in relation to selective catalytic reduction (SCR) deNOx process, removal of nitrogen oxides (NOx) from exhaust gases or other lean-burn engines. This is important to control global air pollution. Within zeolite families, Cu-ZSM-5 is the most famous catalyst to catalyse NO decomposition. [28, 36, 37]

Recently, zeolites have been proposed to use in NO storage and delivery which is important in medical therapies. NO storage and delivery using zeolites are related to the pressure swing adsorption (PSA) process. PSA have highlighted two types of adsorbed NO, reversible and irreversible.[33, 38, 39] Reversible adsorbed means NO weakly held which is predominantly physisorbed species. Irreversible adsorbed NO is relatively strongly held and it is not spontaneously released from the zeolite even at very low pressure. Irreversible NO is primarily chemisorbed with NO bound with the extra-framework cation residing in the zeolite channel through the nitrogen atom to form either mononitrosyl or dinitrosyl complexes.[40, 41] For example this can be described with Cobalt-NO complex structure in the Co-LTA zeolite[40] shown in Figure 1.4. Irreversible adsorption is a good method for storing gas in the material since it not easily released. The irreversible NO can be released when the zeolites are exposed to the moisture since zeolites have higher affinity to water; water molecules displace the NO bound with cation in the zeolite.[42] NO stored in zeolites also can be released by heating sample to a high temperature. However, this method is biological unfriendly. Recently, Morris and co-workers began storing and releasing NO using zeolites. They found that zeolite-A displays good adsorption NO capacity depending on the extra-framework cations in the zeolites and the amount of exchanged metal present. They also demonstrated the anti-thrombus studies proving that the NO-containing zeolite prevents aggregation of platelets.[41-44] A subsequent publication has shown that trials on human skin were successful and the NO-releasing zeolite causes no harm to the skin while an acidified cream (a competing NO-releasing therapy) actually causes quite severe damage to the skin.[45]

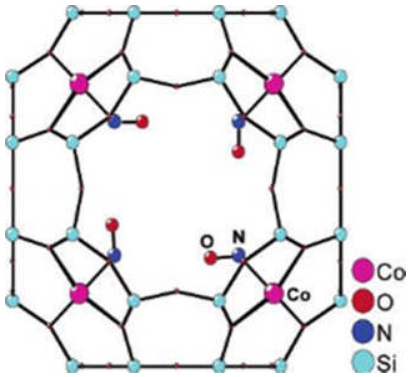


Figure 1.4: Structure of Cobalt-NO complex in Co-LTA zeolites. The cobalt is bound to three oxygen atoms of a six-ring unit in the zeolite framework and bond to the nitrogen of a bent mononitrosyl ligand.[40, 41]

## 1.3.2: NO storage and releasing - MOF

Metal organic frameworks (MOFs) also have a great potential in gases storage due to their high surface area. HKUST1 shows a higher uptake of NO compared with the zeolites but the amount NO release from HKUST-1 is a smaller than the amount actually adsorbed. However, NO-loaded HKUST-1 is still completely inhibits platelet aggregation even though only a small amount of NO has been released.[46] Ni-CPO-27 and Co-CPO-27 have a greater uptake of NO at room temperature with a perfect release upon exposure to the moisture. The adsorption-storage-delivery cycle of the significant amount of NO using M-CPO-27 (M= Ni, Co) shows that it to be active in the vasodilation of porcine arteries.[47]

## 1.3.3: NO delivery using polymer

Another method to deliver exogenous NO is based on polymer or silica functionalized with secondary amines that reacts with NO to form ionic diazeniumdiolates. Two NO molecules react with each amine (giving rise to trivial name NONOate) and are released from the particle

on contact with moisture at an appropriate pH.[35, 41, 48] Another method also explored is light-activated release of NO from metal containing polymer.[49]

### 1.3.4: Simultaneous NO storage and Catalytic NO production using zeolites

Zeolites and MOFs are good for NO storage and delivery agent, however one of the drawbacks of this approach is the reservoir stored NO gas in the materials is finite and cannot be replaced easily especially for longer-term implant. Therefore, an alternative way to deliver the active gas is to produce the gas chemically using catalytic method from suitable substrate. Morris *et.al* have reported that copper containing zeolites such as Cu-X , Cu-ZSM-5 [50] and Cu-MCM-41[51], are not only good for NO storage and delivery, but they also produce the gas by catalytic reaction where the active Cu(I) species in zeolites transform $NO_2^-$ (substrate) to NO.[50, 51] Thus, combining these two methods (gas storage and catalytic gas production) has potential to significantly increase the lifetime of a gas delivery material beyond what is possible with gas storage alone.

## 1.4: Zeotype

Zeotype molecular sieves are a family of solids displaying identical structure to zeolites but different elements composition present in them. [2] For instance, aluminophosphate ($AlPO_4$), titanosilicate (ETS), gallium phosphate (GaPO), silicoaluminophosphate (SAPO), germanosilicate (ITQ-37), metal aluminophosphate (MAPO) and etc. Most zeotypes are found

as synthetic zeotype and they are extensively used in catalysis and absorbent for the molecular separation.[52]

## 1.4.1: Aluminophosphates

In early 1980, Wilson and co-workers reported that aluminophosphate ($AlPO_4$- n) where n refer to discrete structure type;[53] represent the first family of zeotype framework oxide synthesized in the absence of silicon.[54] There are three examples of $AlPO_4$-n analogous to natural zeolite topologies; AlPO-24 (analcime type), AlPO-20 (sodalite type) and AlPO-17 (enrionite/offretite type).[54] The main dissimilarity between AlPO-n and zeolites are fully tetrahedral AlPO-n always have neutral frameworks in contrast to negatively charge of zeolite. Secondly, aluminium atom in AlPO-n can exist in four, five or six coordinated in framework instead of zeolite where the aluminium is always in tetrahedral coordination.[55]

The open frameworks AlPO-n can be categorized into two classes, they are neutral frameworks AlPO-n with Al/P=1 and anionic frameworks AlPO-n with Al/P ≤ 1. Neutral frameworks $AlPO_4$-n are strictly generated by alternating $AlO_4^-$and $PO_4^+$ tetrahedra.[53] As in aluminosilicate zeolites, AlPO-n frameworks are built up from Al-O-P bonds following Löwenstein's rule where Al–O–Al bonds are avoided.[53, 56] The P–O–P bonds are not to be stable in these structures. Thus by avoiding of Al–O–Al and P–O–P bonds, open-frameworks of AlPO-n with even-numbered rings can be formed.[53] The general molecular formula of these materials can be written as $\mathbf{[(AlO_2)_x(PO_2)_x].YH_2O}$.[55] Anionic frameworks AlPO-n molecular sieves are made up from combination of Al-centered polyhedra ($AlO_4$, $AlO_5$, $AlO_6$) and P-centered tetrahedral [$\mathbf{P(O_b)_n(O_t)_{4-n}}$] where **b** denoted a bridging **O**, **t** is a terminal **O** and **n** is an integer. The presence of terminal P-OH and/or P=O groups or $Al(PO)_n$ (n=5,6) in the anionic frameworks AlPO-n has changed the Al/P ratio from the unity of AlPO-n frameworks. The negative charges of anionic framework

AlPOs are normally compensated by protonated organic templates to stabilise the framework. In addition the protonated templates also interact with P-OH and/or P=O groups through H-bonding to stabilise the framework. A notable example of this kind material is JDF-20 with Al/P = 5/6.[53] The anionic frameworks AlPO-n also have various low-dimensional framework structures such as 2D layers with various porous sheets and sheet stacking sequences and 1D chains which might act as fundamental building blocks for complex structures. Generally, the anionic AlPOs are unstable upon removal of the occluded protonated templates by calcination.

## 1.4.2: Silicoaluminophosphates (SAPOs) and Metal aluminophosphates (MAPOs)

Although the three dimensional (3D) AlPO-n materials possess excellent stability at 400 to 600 $^{o}$C,[54] these kind of molecular sieves cannot be used in catalysis directly. This is because they are lacking acid sites due to the neutral framework. Nevertheless, this deficiency can be improved by isomorphous substitution of Al and P atoms in AlPO-n frameworks with other heteroatoms such as $Si^{4+}$, $Mg^{2+}$, $Co^{2+}$, $Mn^{2+}$, $Zn^{2+}$, $Fe^{2+}$and etc. to produce **silicoaluminophosphates (SAPOs)** or **metal aluminophosphates (MAPOs).** For examples SAPO-34[57], SAPO-5[58], MgAPO-20[59], MnAPO-11[60], FAPO-5[61], ZnAPO-LAU[62] and so on. To date about 24 unique pure MAPO zeotype structures belong to AlPO-n analogous have been reported as shown in Table 1.1.[63]

Table 1.1: Structure and composition features of MAPO molecular sieves (D=dimension and R= ring)[63]

| Type Material | Framework type | Metal heteroatom | Channel system | $AlPO_4$-n analogue |
|---|---|---|---|---|
| ACP-1 | ACO | Co, Fe | 3D, 8R | - |
| AlPO-18 | AEI | Co, Mn, Zn, Fe, V, Mg, As, Ga, Ge,Ti, Ni | 3D, 8R | + |
| AlPO-11 | AEL | Co, Mn, Ge, Mg, Nb, Ti, V, Fe, Cu, Ni,Zn, As, Be, Cr, Cd | 1D, 10R | + |
| AlPO-EN3 | AEN | Co, Mn, Cu | 2D, 8R | + |
| AlPO-5 | AFI | Co, Zn, Mn, Fe, Mg, Cr, Ni, V, Cu, Mo. Sn, Ti, Zr, Ca, Sr, Ba, Be, Ge, Li, Ce, Cd | 1D, 12R | + |
| AlPO-14 | AFN | Mn, Mg, Zn, Cr, Co | 3D, 8R | + |
| AlPO-41 | AFO | Co, Mn, V, Zr, Ti | 1D, 10R | + |
| AlPO-40 | AFR | Co, Zn | 2D, 12R x 8R | + |
| MAPO-46 | AFS | Co, Mg, Mn, Ni, Zn | 3D, 12R x 8R x 8R | - |
| SAPO-56 | AFX | Mg | 3D, 8R | - |
| CoAPO-50 | AFY | Co, Zn, Mg, Mn | 3D, 12R x 8R x 8R | - |
| Analcime | ANA | Co | 3D, 8R | + |
| AlPO-C | APC | Co | 2D, 8R | + |
| AlPO-16 | AST | Co, Mn, V, Cr | 0D, 6R | + |
| MAPO-39 | ATN | Zn, Mg, Co | 1D, 8R | + |
| AlPO-31 | ATO | Co, Mn, Zn, Mg, Cr, Cu, Cd, Ti, V | 1D, 12R | + |
| MAPO-36 | ATS | Co, Zn, Mg, Fe, Ti, V, Mn, Be, Ga | 1D, 12R | + |
| AlPO-25 | ATV | Co | 1D, 8R | + |
| AlPO-21 | AWO | Co, Ni, Fe, Cr | 1D, 8R | + |
| Beryllophosphate-H | BPH | Mg | 3D, 12R x 8R x 8R | - |
| Chabazite | CHA | Co, Zn, Mn,Mg, Fe, Ni, Cu, Cr, Be, Li | 3D, 8R | + |
| DAF-1 | DFO | Co, Mg, Ni | 3D, 12R x 10R x 8R | - |
| DAF-2 | DFT | Co | 3D, 8R | - |
| Edingtonite | EDI | Co, Cu | 3D, 8R | - |
| Eironite | ERI | Co, Fe, Mg, V | 3D, 8R | + |
| Faujasite | FAU | Co, Cu, Zn | 3D, 12R | - |
| Gismondine | GIS | Co, Mg, Zn, Mn | 3D, 8R | + |
| CoAPO-CJ40 | JRY | Co, Zn, Mn, Fe | 1D, 10R | - |
| Laumontite | LAU | Co, Zn, Mn, Fe | 1D, 10R | - |
| Levyne | LEV | Co, Zn, Mg | 2D, 8R | + |
| Linde type A | LTA | Co, Zn, Mg, Mn, Fe | 3D, 8R | + |
| Merlinoite | MER | Co | 3D, 8R | - |
| UiO-28 | OWE | Co, Mg | 2D, 8R | - |
| Phillipsite | PHI | Co, Zn | 3D, 8R | - |

Incorporation of divalent or tetravalent heteroatoms with AlPO-n frameworks would generate negative charge thereby creating a potential solid acid catalyst. Normally the negative charged is balanced by $H^+$ ion to form strong Bronsted acid site groups.[64, 65] The metal ion could act as Lewis acid sites when interacting with Bronsted entities as shown in Figure 1.5.[65]

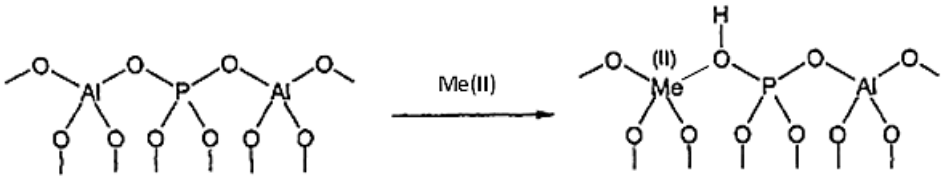


Figure 1.5: Model explaining the way isomorphous substitution of divalent metal generates surface acidity. A surface Bronsted-Lewis interaction is apparent.[66]

There are three types of isomorphous substitution mechanism (SM) of Al and P occurring in AlPO-n which are illustrated in Figure 1.6. First the substitution mechanism 1 (SM I) involves the aluminium substituted with valence atoms +1, +2 and +3 resulting the M-O-P bond. The second substitution mechanism 2 (SM II) is for phosphorus replaced by valence elements +4 or +5 to form M-O-Al bond. The third substitution mechanism 3 (SM III) is substitution of pairs of adjacent Al and P atoms. Only Si exhibitsSM III.[67] Other kinds of the substitutions are not mentioned in Figure 1.6, as they are very unlikely because they would generate either too negative a charge density or high positive charge. Figure 1.6 shows that the negatively charged frameworks generated from the isomorphous substitution also can be balanced by positively extraframework species such as quaternary ammonium cation, protonated amines, hydroxonium ion or transition metal ions.[68] In addition incorporation of transition metal into $AlPO_4$-n framework would produce the isolated redox centre to the material.[69]

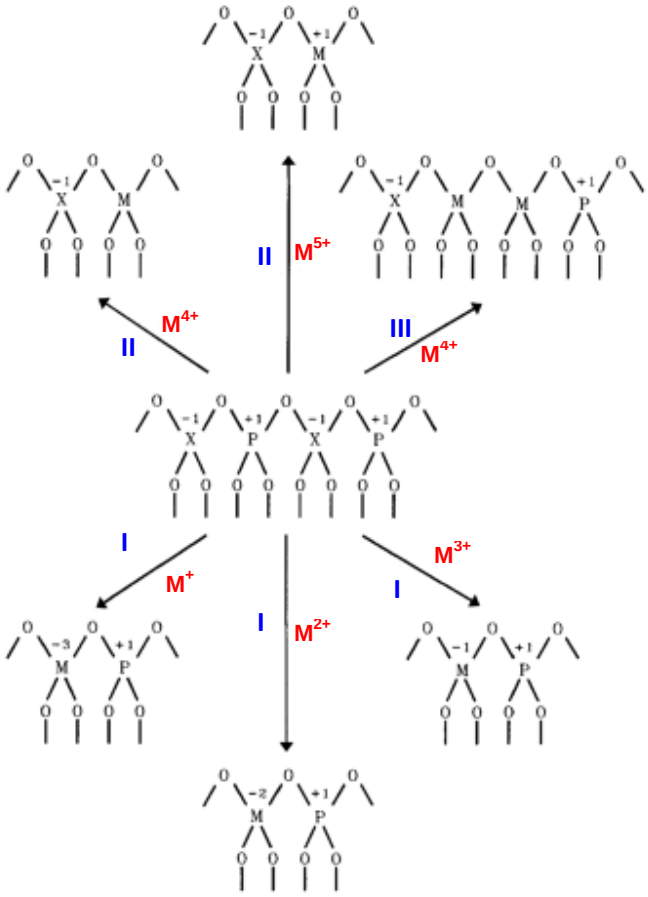


Figure 1.6 : Isomorphic substitution mechanism of in $AlPO_4$-n (X = Al) based frameworks[67]

## 1.5: Application of SAPOs and MAPOs

Microporous crystalline silicoaluminophosphates (SAPOs) and metal aluminophosphates (MAPOs) also represent an important group of inorganic materials because of their large potential as adsorbents and catalysts.

SAPOs have been used in processes such as fluid catalytic cracking, hydrocracking, isomerization, oligomerization, conversion of alcohols or ethers, and the alkylation of aromatics.

The use of SAPOs in conversion of oxygenates to light olefin products, particularly ethylene and propylene, is becoming of greater interest for large scale, commercial production facilities.[70] Among SAPOs, the small-pore SAPO-34 with chabazite (CHA) structure has received great attention in recent years as active catalyst due to its high selectivity in the methanol-to olefin reaction. This material is widely used in industrial practices as well as experimental studies, and has been demonstrated to have a high selectivity toward light olefins at almost 100% methanol conversion.[71-76] On the other hand, the catalytic activity of copper ion exchanged Cu-SAPO-34 exhibits higher activity in selective reduction of NO with $C_3H_6$.[77]

MAPOs are important catalysts in many reactions because of their redox and acid catalytic properties. For example, metal aluminophosphate-36 (MAPO-36) (Me=Mn, Co) is a bifunctional catalyst for converting cyclohexanone to ε- caprolactam, where mutually present $Me^{2+}$ and $Me^{3+}$ ions act as Bronsted and redox sites.[78] MAPOs are also found to be selective catalyst for isomerization of 1-pentene, yielding around 60% of three pentene isomers: 3-methyl-1-butene, 2-methyl-1-butene and 2-methyl-2-butene.[79] Additionally, cobalt aluminophosphate (CoAPO) family are extensively used mainly to catalyse autooxidation of cyclohexane in the liquid phase.[80-83]

## 1.6: Synthesis

Generally, syntheses of zeolite and zeotype molecular sieves are formed by mixing of reactants to a gel and maintaining them at 100 $^oC$ or more for a selected period. The syntheses of these materials normally go through several steps as shown below:[84, 85]

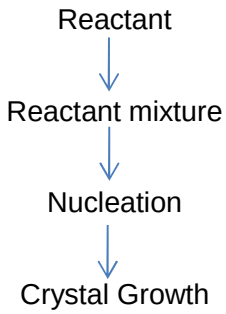


The crystallization mechanisms of zeolites and molecular sieves are very complex due to variation of the equilibria, solubility and chemical reactions occur throughout the heterogeneous synthesis mixture during the process. In 1992 Davis and Lobo proposed two types of extreme synthesis mechanism of zeolite:[2]

*i. Solution-mediated transport mechanism*

Solution-mediated transport mechanism process as shown in Figure 1.7 involves the diffusion of silicate, aluminate, and/or aluminosilicate species from the liquid phase to the nucleation site for crystal growth. Many examples of solution-mediated transport mechanisms occur in the synthesis of zeolite for examples of the mechanism are in the synthesis of zeolite Y, S (GME) and P (GIS) reported by Ueda et al.[86]

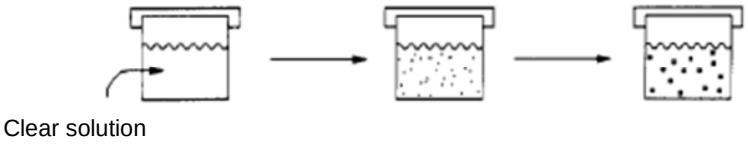


Figure 1.7: Solution-mediated transport solution[2]

*ii. Solid-phase transformation mechanism*

The mechanism involves a solid hydrogel which reorganizes to produce the zeolite structure as shown in Figure 1.8. Examples of zeolite prepared by this type of mechanism are ZSM-35 (FER) and ZSM-5.[87]

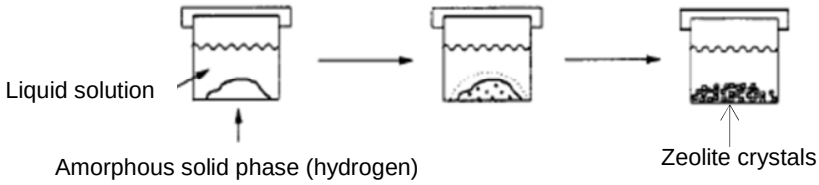


Figure 1.8: Solid-phase transformation crystallization mechanism[2]

## 1.7: Organic Guest Molecule

Usually in the synthesis of molecular sieve, additives such as organic guest molecules are added into the synthesis gel. This additive is generally divided into three categories; (i) true templating, (ii) structure directing and (iii) space-filling. True templating takes place when the zeolite structure must adopt geometric and electronic configurations that are unique to the templating molecule and upon removal of the organic species, the pore in the zeolite remains the shape of molecule.[88] There are very few examples of true templating, the best example being $C_{18}H_{36}N^+$ in the synthesis of ZSM-18.[2] Figure 1.9 shows the schematic illustration of siliceous zeolite formation using tetramethylammonium cations as templates. The reaction relates to the organization of silicate anion around additive to form solution complex and produces the basic geometric organic-inorganic interaction relationship between templates and

zeolite pores during the nucleation of crystal growth. A similar mechanism also can be suggested for microporous aluminophosphate synthesis.[88]

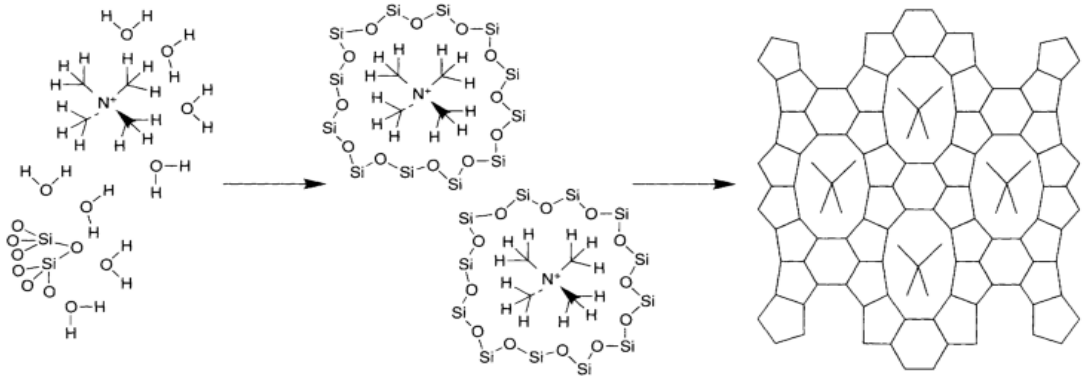

Figure 1.9: Schematic illustration of siliceous zeolite formation using tetramethylammonium cations as template.[88]

Structure directing agents refer to the single organic species that direct the formation of specific zeolite structure. As examples of the structure direction in the synthesis of zeolite (i) N, N, N-trimethyl-ammonium derivative of 1-adamantanamine in the synthesis of SSZ-24 and (ii) 1, 4, 7, 10, 13, 16-hexaoxyacyclooctane (18-crown-6) in the hexagonal faujasite synthesis.[2]

Space filling by the organic additives can enhance the thermodynamic stability of organic-framework composite as compared to the framework alone. This is due to the interaction between organic and inorganic structure through the van der Waal's forces.[88] For example, at least 22 and 13 different organic molecules can be used to synthesize ZSM-5 and ZSM-48, respectively. In this case, clear that the organic molecule prefers to act as space filler rather than structure directing agents.[2]

## 1.8: Ionic liquids

An ionic liquid (IL) is defined as a molten salt typically containing an organic and inorganic cation. The anions and cations are designed to pack poorly together, meaning that the salts remain liquid to very low temperature.[89, 90] Ionic liquids can be classified into two types; (i) room temperature ionic liquids (RTILs) which refer to the compound liquid at room temperature and (ii) near room temperature ionic liquids (nRTILs) where the compound is liquid below a certain temperature, normally 100 $^{o}$ C.[90] Figure 1.10 shows some of cations and anions are commonly used in the formation of ionic liquids. [91]

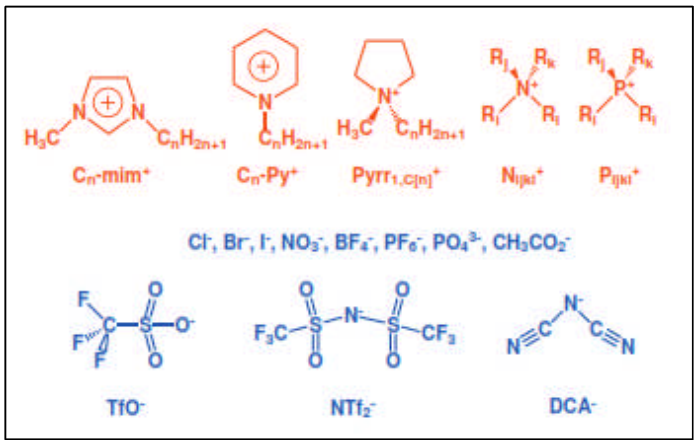


Figure 1.10: Common types of cations (red) and anions (blue) in ionic liquid[91]

The link between ionic liquids and green chemistry is unambiguously related to the fascinating solvent properties of ionic liquids are given below:[92, 93]

i. Owing to the non-volatile and have low vapour pressures, ionic liquids can be utilized at high vacuum systems meaning many containment problems will be eliminated.

ii. Ionic liquids have great solubility properties in a broad range for both organic and inorganic materials. This serves to bring the unusual reagent combinations together in the same phase.

iii. Ionic liquids are often composed of poorly coordinating ions, so they have potential to be highly polar non-coordinating solvents which is particularly important when transition metal based catalysts are used.

iv. They are non –flammable.

v. Ionic liquid often high thermal stability.

vi. They are low melting point

## 1.8.1: Synthesis of ionic liquid

The synthesis of ionic liquids can be generally split into two sections as below:[94] (The diagram shown in Figure 1.11)

*i. Formation of the desired cations*

The formation of the cations may be carried out either by protonation with a free acid or by quaternization of an amine or phosphine, most commonly with a haloalkane. In principle, the quaternization reaction is extremely simple where the amine or phosphine is mixed with the desired haloalkane, and the mixture is stirred and heated. The most common starting material used in a quaternization reaction is 1-alkylimidazole.

*ii. Anion exchange.*

The anion exchange reactions of ionic liquids can really divided into two distinct categories:

a) *Direct treatment of halide salts with Lewis acid*

In general terms treatment of quarternary halide salt ($[Q]^+ X^-$) and Lewis acid ($MX_n$) result in the formation of more than one anion species.

$$[Q]^+X^- + MX_y \leftrightarrow [Q]^+ + [MX_{y+1}]^-$$

An example of this can be illustrated for the reaction between [EMIMCl] and $AlCl_3$ by a equibiliria series as below:

$$[EMIM]^+Cl^- + AlCl_3 \leftrightarrow [EMIM]^+[AlCl_4]^-$$
$$[EMIM]^+[AlCl_4]^- + AlCl_3 \leftrightarrow [EMIM]^+[Al_2Cl_7]^-$$
$$[EMIM]^+[Al_2Cl_7]^- + AlCl_3 \leftrightarrow [EMIM]^+[Al_3Cl_{10}]^-$$

The Lewis acid can be used in order to produce ionic liquid are $AlETCl_2$, $BCl_3$, CuCl and $SnCl_2$.[94]

b) *Formation of ionic liquids by anion metathesis*.

The preparations are related to the air and water-stable ionic liquid reaction with the appropriate silver salts. The first preparation involved the reaction between [EMIM]I and several silver salts such as $AgNO_3$, $AgNO_2$, $AgBF_4$, $Ag(CO_2CH_3)$ and $Ag_2SO_4$ in methanol or aqueous methanol solution. This preparations were reported by Wilkes and Zaworotko in 1992.[95]

In step (ii), the formation of ionic liquids contains only one anion species when exchange reaction is allowed to go to completion. To ensure high purity of ionic liquid, the essential test

using silver nitrate is needed to determine the halide ions presence after ion exchange. For instance of the ionic liquid anions are formed in this way comprise of $NO_3^-$, $BF_4^-$ and $PF_6^-$.[96]

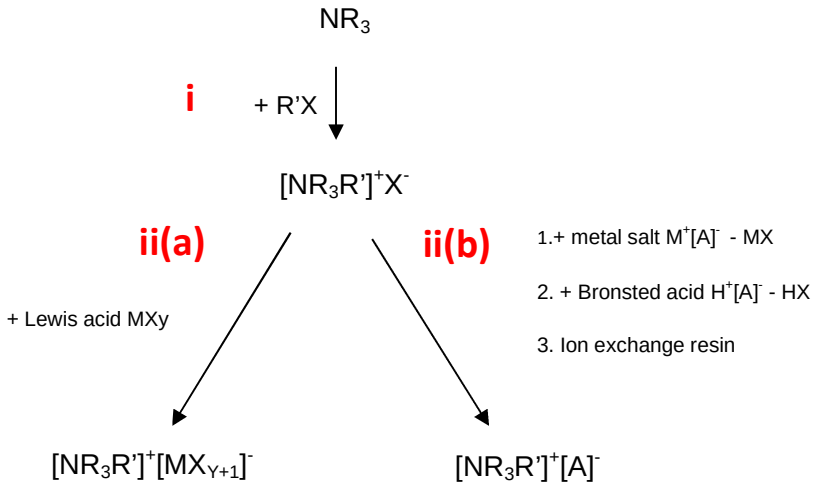


**Figure 1.11:** Typical synthesis path for the preparation of ionic liquids.[94]

## 1.8.2: Miscibility with water

Overall both hydrophilic and hydrophobic ionic liquids can result from the composite properties of cation and anions. Normally, hydrophobicity increases with the length of alkyl chain and larger anion. Most ionic liquids consist of anions such as halide, ethanoate, nitrate, and are trifluoroacetate are soluble in water whilst $[PF_6]^-$ and$[(CF_3SO_2)_2N]^-$ are not. Nevertheless, ionic liquids based on $[BF_4]^-$and $[CF_3SO_3]^-$ can either form biphasic systems ($[C_n mim][BF_4]$, n > 4): where $[C_n mim]$ abbreviated to 1-alkyl-3-methylimidazolium, or are fully miscible with water (e.g., $[C_2 mim][BF_4]$ and $[C_4 mim][BF_4]$. Thus, the anion has a primary effect on water miscibility and the cation as a secondary effect.[97]

Most of the ionic liquids are hygroscopic and can absorb a significant amount of water from the atmosphere, even after a moderate drying process, water can still found to be present.[98]

The presence of water in the ionic liquid may have a dramatic effect on reactivity in many syntheses using ionic liquid media. Recently many studies have been reported regarding ionic liquids that are both air and moisture stable. Rogers and co-workers have studied several types of ionic liquids related to the water content. As an example, hydrophobic ionic liquid; 1-butyl-3-methylimidazolium bis-((trifluoromethyl)sulfonyl)amide [$C_4$mim][$Tf_2$N] still inevitably contains 474 ppm of water even after drying process while 1-butyl-3-methylimidazolium chloride [$C_4$mim][Cl] is hygroscopic ionic liquid contains 2200 ppm water after drying.[99]

## 1.8.3: Eutectic mixture

A eutectic mixture is related to ILs but usually comprises organic halide and hydrogen bonding donors for example amides, amines, alcohol and carboxylic acid.[100] The word eutectic comes from the Greek word 'eutektos' which means 'easily melted'. Generally a eutectic mixture is a mixture of two or more compounds which have a lower melting point than their constituents, for example choline chloride has high melting point about 300$^o$C, but when mixed with urea in 1:2 ratio the melting point of mixture is 12$^o$C.[101] The decrease of the melting point arises from the hydrogen bonding interactions between the chloride ion and the urea molecules.[102] Normally, the compound has the capability of donating and accepting electrons or proton to form hydrogen bond shows the high solubility in the reaction for used in the preparation of different kinds of materials.[100] Table 1.2 shows several examples of deep-eutectic solvents with their constituent compounds and their melting points.

Table 1.2: Melting point of deep-eutectic solvent and their constituents compounds[100]

| H-bond donor (m.p($^{o}$C)) | Ammonium salt (m.p($^{o}$C)) | DES (m.p($^{o}$C)) |
|---|---|---|
| 1,3-dimethyl urea (101-105) | tetraethylammonium bromide (285-290) | 20-25 |
| 1,3-dimethyl urea (101-105) | choline chloride (298-305) | 69-71 |
| tetrahydro-2-pyrimidione (264-266) | choline chloride (298-305) | 150-155 |
| 2-imidazolindone (129-132) | choline chloride (298-305) | 69-73 |
| urea (134) | choline chloride (298-305) | 12 |
| succinic acid (183-187) | choline chloride (298-305) | 73-77 |

## 1.9: Hydrothermal, Solvothermal and Ionothermal Synthesis

The nature of solvent interaction between reacting species is very important to the molecular sieve synthesis outcome. Commonly, in the synthesis of zeolites and molecular sieves, water or non-aqueous solvents are used in so-called hydrothermal or solvothermal synthesis respectively.

Water is utilised in the hydrothermal synthesis of zeolites. In the synthesis, water can also serve as space filler to stabilize the porous lattice of zeolite. In addition it also used in hydrolysis and reformation of T-O-T bonds. Thus, the chemical reactivity is enhanced and the mixture viscosity is decreased. So water not only acts as solvent but also as reactant and catalyst in the synthesis of zeolite.[103] Normally in hydrothermal synthesis the reactants are sealed inside Teflon-lined autoclave which gives the significant autogenous pressure often up 15 bar [16] when heated above 100 $^{o}$C. The important reaction and crystallization processes in hydrothermal synthesis do not necessarily take place in solution but can occur at the surfaces of gels present in the mixtures.[29] The first zeolite was formed under hydrothermal synthesised by Barrer and Milton in 1940.[104]

The non-aqueous route or solvothermal synthesis is another accessible route to synthesise zeolite and molecular sieves. Basically this route employs organic solvent rather than water. The organic solvents are classified into four groups based on their tendency to hydrogen bond; high, high-medium, low-medium and non-hydrogen bonding. The use of high-medium and low medium organic solvents are preferred in the interaction between template and frameworks species because it tends to be most successful in molecular synthesis.[88] The typical organic solvents have been used in the synthesis of molecular sieve material are hexanol, propanol, pyridine, glycerol and glycol.[105] As with water these molecular solvent also produce significant autogenous pressure at elevated temperature.[90]

Ionothermal synthesis refers to using ionic liquids (ILs) as both solvent and structure-directing agent in the crystallization reaction. It has been developed for preparing zeolite analogues also known as 'zeotype' where the first zeotype aluminophosphate was prepared by Morris and co-workers in 2004.[101] Compared with hydrothermal or solvothermal methods, using ionothermal synthesis technique can avoid introduction of volatile solvents since the IL is ionic in nature, thus allowing the reactions take place at near ambient pressure where the safety concerns can be eliminated even can lead new formation of materials frameworks. The most important feature of ionothermal synthesis is the removal of competition between template-framework and solvent framework interaction which present in hydrothermal or solvothermal synthesis .[105] This can be seen in Figure 1.12 where the schematic of hydrothermal and ionothermal synthesis are represented.

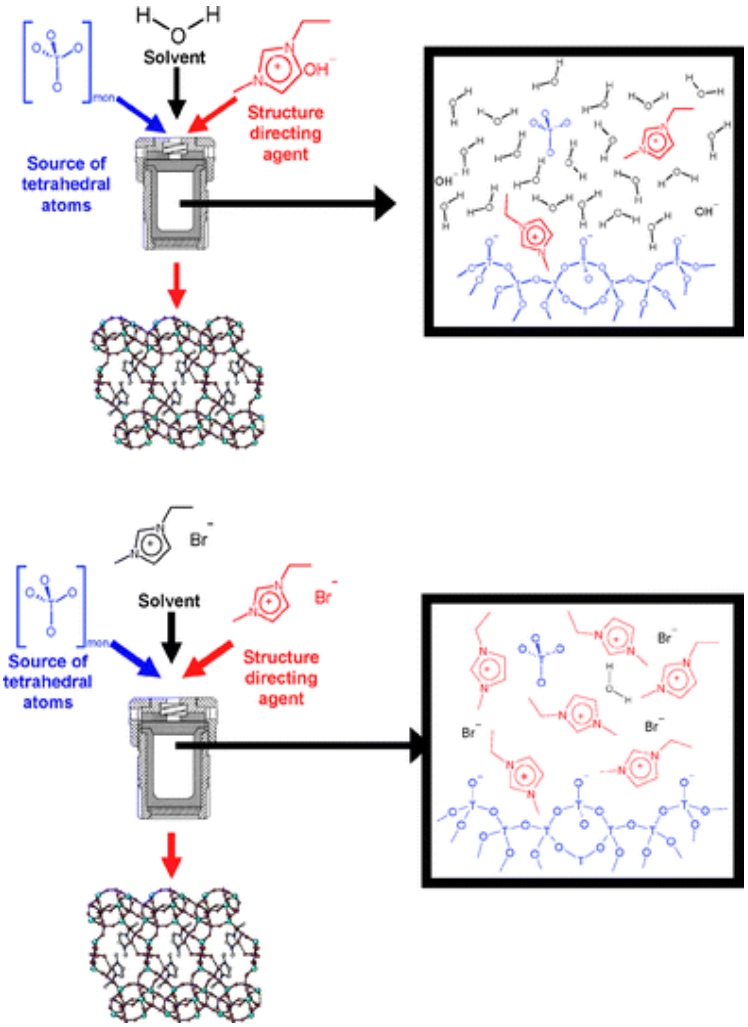


Figure 1.12: Schematic illustrations of the synthesis of tetrahedral framework zeotype under hydrothermal (top) and ionothermal synthesis (bottom). Note in ionothermal synthesis the solvent and structure directing agent are depicted as same species, while is water present in the small amounts.[90]

## 1.10: The role of fluoride ions

Traditionally zeolites are prepared at higher pH condition under hydrothermal synthesis where $OH^-$ is used to solubilize silicate and aluminate species.[2, 106] In 1978 a new route to synthesise zeolite using $F^-$ has been introduced by Flanigen and Patton.[107] The behaviour of fluoride ion is

close to hydroxide ion as a mineralizer and complexing ion to contribute the formation of molecular sieve structure.[106] Several zeolites were crystallized in the presence of fluoride ion; MFI, FER, MTT, MTN and TON. Another particular importance of $F^-$, it is suitable for synthesis of heteroatom-substituted (B, Al, Fe, Ga, Ti) high silica zeolites where usually transition metals e.g. iron species are more stable at lower pH rather than higher pH.[2]

Using $F^-$ in the synthesis of molecular sieve does not necessarily influence the pH in gel but it can lead to slow down the nucleation and growth rates, resulting in larger and few defect crystals. On the other hand, fluoride ion has been found to impart a structure directing and templating effect by interacting with the framework. For instance as shown in Figure 1.13, fluoride ions behave as bidentate ligand linking the two aluminium ions in AlPO-34. Eventually, the anion framework produced requires a cation such as protonated organic amine to balance the charge.[55]

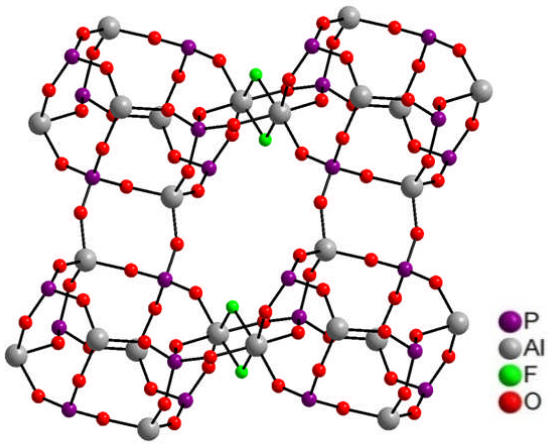


Figure1.13: Fluoride bridges in as-synthesized $AlPO_4$-34

## 1.11: Co-template or Structure Directing Role of Amines in Ionothermal Synthesis

The addition of organic molecules such as amines and quaternary ammonium ion as templates and structure directing agent are important in the synthesis of inorganic porous material. Many efforts have been made in design and utilization of novel organic templates with different size, geometry and polarity to synthesise the new porous materials. Nevertheless, the use of two types of organic templates in the synthesis also has been proved to be promising in the formation of molecular sieves.[108-110] For instance, some 2D layered aluminophosphate materials have been synthesised under hydrothermal or solvothermal condition in the presence of two organic amines.[111, 112] Furthermore, computational studies of host-templates interaction demonstrate that in some cases using mixed organic amines is more energetically favorable than using only one of them as templates.[108, 113]

Recently, the strategy of organic amines or quaternary ammonium ions added to ionothermal systems as an alternative synthesis route has been applied successfully in the preparation of several open-framework phosphates. The addition of amines can alter the original crystallization reaction, leading to the formation of pure and different product structures.[114-117] In some cases it has been demonstrated that the added organic amines or amine IL hybrid/supermolecule produced through hydrogen bonding interaction could help the formation of a specific cages or pores of certain structure.[114] Impressively, there are two novel aluminophosphate materials have been discovered including the first 20-ring extra-large pore of aluminophosphate molecular sieve called as DNL-1 (with –CLO topology)[115] and 3D anionic aluminophosphate framework denoted as JIS-1 with an Al/P ratio of 6:7.[117] These framework materials have been formed by added organic amines act as co-templates or co-SDA together with the ionic liquid.[115, 117]

Hence, these results have stimulated this study to attempt this strategy to synthesise metal aluminophoshate with 3D structures.

## 1.12: Nitric Oxide (NO)

### 1.12.1: Background

Until 1986, nitric oxide was recognized as only a noxious pollutant in car exhaust fumes, fossil fuel smoke and cigarette smoke, which is responsible for acid rain and depletion of the ozone layer.[118, 119] However, the interest in the physiological role of this simple diatomic molecule arose exponentially since the endothelium-derived relaxing factor (EDRF) was introduced by Furchgott and Zawadski in 1980 where it has been first identified as NO by Palmer et al. in 1987. Then in 1992, NO was voted as "molecule of the year" in Science and the scientists Robert F. Furchgott, Louis J. Ignarro and Ferid Murad have earned Nobel Prize in Physiology or Medicine in 1998 for their discoveries concerning "nitric oxide as a signaling molecule in the cardiovascular system".[119]

### 1.12.2: NO properties

Nitric oxide is also known as nitrogen monoxide (IUPAC name) and its molecular formula is NO. This molecule has an unpaired electron in valence shell and means it is classified as free radical. The nature of •NO radical is able to react with other species with unpaired electrons such as $O_2$, superoxide ($O_2^-$) and other radical species. However, •NO has less tendency to react with its self in radical-radical dimerization process. This may seem curious at first glance

since the dimerization would lead to ON-NO structure where the entire atoms possess a full complement of eight valence electrons, so this is satisfy the rule of octet. In order to explain of this anomaly, the molecular orbitals of •NO must be considered. Figure 1.14 shows the molecular orbital diagram of •NO. As can be seen in this diagram, the •NO consists of eleven electrons where five electrons come from nitrogen and six electrons from oxygen. There are eight electrons in bonding orbitals ($\sigma_1$ =2, $\sigma_2$ = 2 and π =4) and three electrons occupy in antibonding orbital ($\sigma_1$*= 2 and π* =1). This gives a bond order of 2.5. As a result the N-O bond length (1.15 Å) is in between double and triple bond distance. When •NO forms a dimer (O=N-N=O), the total molecule bond order is 5. Therefore, since the dimer of •NO does not have any net gain in overall bonding at room temperature and pressure, the entropy would favor the monomer NO. Investigation found that the dimerization energy of two •NO is 2-4 kcal/mol which is indicating the unusual weak N-N bond. This N-N interaction in •NO dimer is also considerably weaker than covalent bond and yet cannot be explained by van der Waals interaction, which provide the stabilization on the order only 10 kcal/mol. In •NO, the unpaired electron is delocalised over both N and O atoms. However, since the nitrogen possess higher orbital coefficient, therefore the radical is predominatly at the nitrogen.[120]

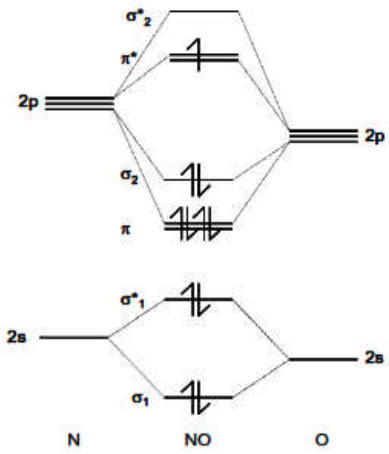


Figure 1.14: Molecular orbital diagram of •NO [121]

In our environment, NO is produced mostly from the combustion engines and small percentage from the lightning strikes. This gas is easily oxidised to the brown gas known as nitrogen dioxide ($NO_2$). [121] In the atmosphere NO, $NO_2$ and other nitrogen oxides exist in a mixture which is known as NOx.[122] This mixture is responsible for the urban smog and depletion of ground level ozone.[123] [124] Another problem of NOx mixture is when it reacts with water in the atmosphere nitric ($HNO_3$)and nitrous acids ($HNO_2$) would be formed which contribute the 'acid rain' that damages buildings and harms the wildlife in lakes and rivers.[121] Therefore, in order to remove NOx from stationary or mobile, most of technologies are using catalysts converters which one of the most efficient methods in terms of relatively high efficiency and low cost.[122]

NO has low solubility ($10^{-3}$ M) but high diffusivity in water ($4.8 \times 10^5$ $cm^2$ s) and lipid media.[125, 126] Accordingly, NO is different from $N_2O_3$ (the anhydride of nitrous acid) and $N_2O_5$ (the anhydride of nitric acid) as it does not undergo any hydrolysis in aqueous environment to form acid. Therefore, this hydrophobic property, enables NO to diffuse unchanged across the biological cell membranes provided there is no oxygen present.[121] However, in oxygenated water or in certain biological media such as blood, NO would be slowly oxidised to nitrite and then quickly oxidise to nitrate.[126]

Another reason why NO is very useful is it is easily oxidised and easily reduced. When the unpaired electron of NO is removed, the nitrosonium ion ($NO^+$) would be formed. For instance, $NO^+$ is very important in biological reaction in transnitrosation process where $NO^+$ from nitrosothiol can be transferred to secondary thiol (see equation 1.1).[127] Since free $NO^+$ cannot exists in cell, therefore nitrosothiol is viewed as molecule carrier of $NO^+$ and also to stabilize the NO reactivity in the mechanism of endothelium-derived relaxing factor (EDRF).[128]

$$R^1SNO + R^2S \longrightarrow R^1S^- + R^2SNO \qquad (1.1)$$

The possibility of nitroxide ions ($NO^-$) in physiological role has been little explored, although it is quite feasible.[127] However, $NO^-$ also shows a biological significant which is used in the altering thiols and also binding with iron in hemoglobin.[121, 127]

In the immune system, NO and superoxide ($O_2$) are simultaneously produced by activated macrophages leading to the formation of peroxynitrite anions ($ONOO^-$), which constitute a harmful agent to kill the diverse of bacteria or pathogens in the body.[129]

## 1.12.3: Biosynthesis of NO

In mammals, NO is produced by the conversion of L-arginine to L-citrulline as shown in Figure 1.15 by using enzyme NO synthase (NOS).[130] NOS is a hemoprotein which contains both oxygenase and reductase domains. Oxygenase domain contains cofactors of tetrahydrobiopterin ($BH_4$) and iron protoporphyrin IX (PPIX, heme), while the cofactors for reductase domain are Flavin Mononucleotide (FMN) and Flavin Adenine Dinucleotide (FAD).[131] There are two steps and five electrons involve in the oxidation process of L-arginine, catalysed by NOS. In the initial step, two electrons are accepted by NOS Falvins (FMN and FAD) from nicotinamide adenine dinucleotide phosphate (NADPH), afterward these electrons are transferred to haem iron in the oxygenase domain to reduce $NOSFe^{3+}$ to $NOSFe^{2+}$.[132] The domains are linked with Calmodulin ($Ca^{2+}$) as activator to enable flow the electrons between them and the FAD and FMN. In this step, L-arginine is hydroxylated to form an enzyme-bound intermediate which noted as $N^{\omega}$-hydroxyl-L-arginine. In the second step, three-electron are take place in oxidation process, where the heme iron binds with $O_2$ and the enzyme employs NADPH to oxidize $N^{\omega}$-hydroxyl-L-arginine to L-citrulline and NO.[132]

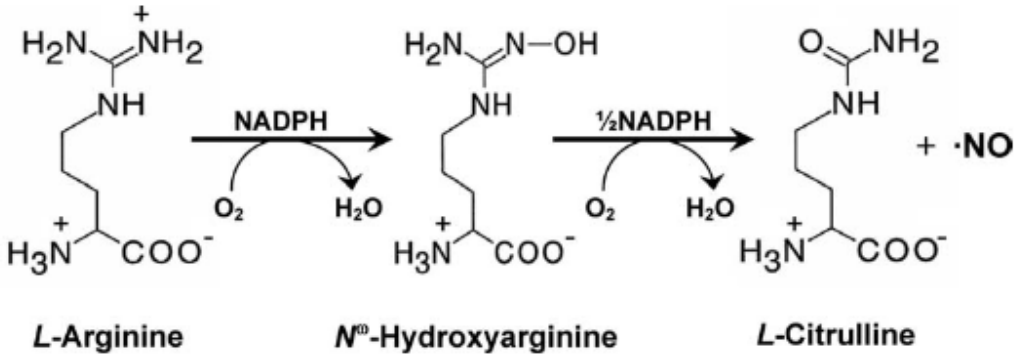


Figure 1.15: Biosynthesis of nitric oxide from L-arginine[132]

## 1.12.4: Different isoforms of NOS

NOS can be categorised in three different isoforms and the names below are refer to the most common isoform of NOS exist in the body.

- Endothelial NOS (eNOS) is responsible to produce NO in the endothelial cells of blood vessel.[133] eNOS also found in platelets, myocardium, and endocardium.[132]
- Neuronal NOS (nNOS) is predominantly active in central and peripheral neurons to produce NO which is substantial for the cell communication.[133]
- Inducible NOS (iNOS) is found primarily in immune cells and glial cells (astrocytes and microglia) and it is activated by response to pathogen recognition and cytokine release. The primary function of iNOS is to use in NO oxidative stress to defend against pathogens.[133]

All the three synthases above have similar structure but the main differences are in their response to Calcium ion ($Ca^{2+}$) concentration in the cell. eNOS and nNOS are classified as

constitutive enzyme (cNOS). The activation of cNOS depends to the elevated intracellular $Ca^{2+}$ levels. When the $Ca^{2+}$ ion levels rise, the $Ca^{2+}$/Calmodulin complex would strongly bound to eNOS and nNOS to form NO. However, in iNOS, the Calmodulin complex is already tightly bound and therefore iNOS activity does not affected by calcium transient.[134] The iNOS appears to be active when the unfriendly agent attacks the body and NO is required to discard any threat.[135] This is different to eNOs and nNOS where they are in large quantity at any time of each lying dormant in the endothelial and neuronal tissue respectively, while there is very little iNOS until it is required.[121]

## 1.12.5: Pathology of NO in the body

NO is one of the smallest molecules found in biological systems. It is essential to the daily activities of many cells and tissues in the body. However, the right amount of NO production is very important for life, if too much or too low can lead life threatening diseases and even can be fatal. Table 1.3 shows the pathology of NO production that can lead many diseases to the body.

Table 1.3: Pathology of NO release

| Nitric Oxide Concentration | |
|---|---|
| Too Low | Too High |
| Hypertension<br>Atheriosclerosis<br>Diabetes<br>Ischemia (stroke, heart Alzheimer's disease)<br>Parkinson's disease<br>Fibrosis<br>Cancer | Septic shock<br>Hypotension<br>Excessive bleeding<br>Meningitis<br>Rheumatoid arthritis |

## 1.12.6: The role of NO in the cardiovascular system

In the cardiovascular system, blood vessel is a transport to flow the blood throughout entire body. It is formed into three distinct layers, as shown in Figure 1.16. The hole in the middle is called lumen where the blood flows, while on the inside of the lumen is a single layer of cells known as the endothelium (endothelial cells) and lastly the wall of the vessel consists mainly of the smooth muscle.

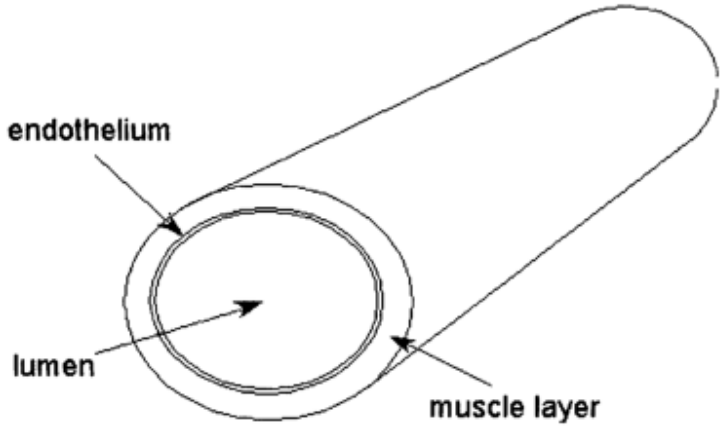


Figure 1.16: Structure of main component of blood vessel [136]

This vessel can be enlarged or dilated depending how much the blood delivered to specific tissue or organ. The smooth muscle wall relaxes when it induced by NO which is produced by endothelial cell. This relaxation enlarges the lumen to allow the blood flows through the vessel. When the blood flow increases, the endothelium releases more NO and vice versa to maintain the sufficient concentration of NO in the blood stream. However, if the inadequate NO releases, the vascular muscles does not relax to the appropriate degree and cause the vasoconstriction or excessive vasodilation which responsible to the hypertension (high blood pressure) or hypotension (low blood pressure), respectively.

When blood vessels are damaged, a repair mechanism called blood clotting or coagulation is triggered. In this mechanism, initially the bleeding is stopped when the vessel walls close the lumen to reduce the blood flows to the injury side. Then the platelets aggregate to the site of the injury and stick together as a "plug". Platelets are discoid anucleate subcellular fragments that can vary in size up to 3 μm in diameter. They arise from the megakaryocyte in the bone marrow and circulate around in blood. Fibrin is insoluble protein[137] also begin to form web-like mesh to trap the blood cell within it. Hence, all these obviously prevent the bleeding, however, if the platelets continuously aggregate, the clot may enlarge to form thrombosis where it could block the blood flow. This is dangerous and sometimes fatal, so the anticoagulant called prostaglandin $I_2$($PGI_2$) is produced by the endothelial-specific cyclooxygenase enzyme system responsible to inhibit the platelet aggregation.[138]

About 70 to 90% of NO released by endothelium is used to prevent platelet aggregation. NO inhibits platelet aggregation depends on the cyclic guanosine monophosphate (cGMP) mechanism which is similar way in smooth muscle relaxation. NO activates soluble guanylate cyclase to catalyse the formation of cGMP from GTP. The decreased formation of NO by dysfunctional endothelium can lead directly to platelet-rich thrombosis. When the endothelium is damaged, the macrophages move to side of damage and die after ingesting the oxidised lipid

present. Then the lipid core left and coating inside the wall of blood vessel. This is the first step of the complex process called as stenosis. If this continues, it can lead severe of narrowing lumen of artery, restricting the blood flow. Generally stenosis occurs in the arteries near to the heart and one of the treatments is stenting, where the stent (tiny collapsible metal devise) is placed inside the artery to enlarge the lumen, as shown in Figure 1.17. However, the insertion of stent that contact with blood can cause thrombosis formation on its surface, reducing the diameter of the artery. This usually treated with the administration of anticoagulants and antiplatelets which can lead to hemorrhagic hazard.[51] Stent coatings that release antithrombotic,[139] antiinflammatory,[140] and antimitogenic[141] agents to reduce in-stent thrombosis or restenosis have had some success. Currently research is ongoing into coating stent and other medical devices with NO releasing material to prevent the thrombus formation.

.

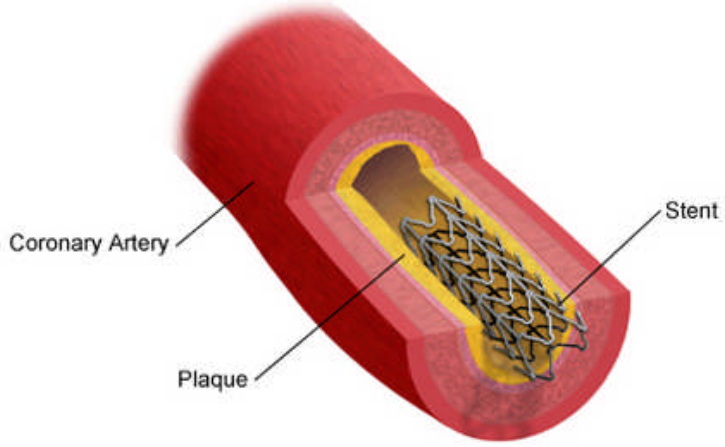


Figure 1.17: A stent placed in the artery

## 1.13: References


1. A. Corma, *Chemical Review*, 1995, **95**, 559-614.
2. M. E. Davis and R. F Lobo, *Chemistry of Materials*, 1992, **4**, 756-768.
3. J. Weitkamp, *Solid State Ionics*, 2000, **131**, 175-188.
4. R. M. Lago. W. O. Haag and P. B. Weisz, *Nature*, 1984, **309**, 589-591.
5. Ch. Baerlocher and L. B. McCusker, *Database of Zeolite Structures*: *http://www.iza-structure.org/databases/*.
6. C. J. Rhodes, *Annual Reports Section "C" (Physical Chemistry)*, 2007, **103**, 287-325.
7. L. B. McCusker and C. Baerlocher, *Studies in Surface Science and Catalysis*, Elsevier, 2007, **168**, 13-37.
8. J. D. Sherman, *Proceeding of the National Academy of Science of the United State of America*, 1999, **96**, 3471-3478.
9. R. E. Morris, *Journal of Materials Chemistry*, 2005, **15**, 931-938.
10. Q. Huo, *Modern Inorganic Synthetic Chemistry*, Elsevier, Amsterdam, 2011, 339-373.
11. S. M. Auerbach, K. A. Carrado and P. K. Dutta, *Handbook of Zeolite Science and Technology*, New York, 2003, 1-19
12. T. Maesen, *Studies in Surface Science and Catalysis*, Elsevier, 2007, **168**, pp. 1-12.
13. A. Dyer, *Studies in Surface Science and Catalysis*, Elsevier, 2007, **168**, 525-553.
14. R. P. Townsend and E. N. Coker, *Studies in Surface Science and Catalysis*, Elsevier, 2001, **137**, 467-524.
15. H. Ghobarkar, O. Schäf and U. Guth, *Progress in Solid State Chemistry*, 1999, **27**, 29-73.
16. Y. Li, H. Yi, X. Tang, F. Li and Q. Yuan, *Chemical Engineering Journal*, 2013, **229**, 50-56.
17. K. Morishige, *Journal of Physical Chemistry. C*, 2011, **115**, 9713-9718.

18. I. M. Dahl, E. Myhrvold, A. Slagtern and M. Stoecker, *Adsorption Science and Technology*, 1997, **15**, 289.

19. S. Wang, H. Li, S. Xie, S. Liu and L. Xu, *Chemosphere*, 2006, **65**, 82-87.

20. A. Martucci, L. Pasti, N. Marchetti, A. Cavazzini, F. Dondi and A. Alberti, *Microporous and Mesoporous Materials*, 2012, **148**, 174-183.

21. R. T. Yang, Y. D. Chen, J. D. Peck and N. Chen, *Industrial & Engineering Chemistry Research*, 1996, **35**, 3093-3099.

22. M. S. A. Baksh, E. S. Kikkinides and R. T. Yang, *Separation science and technology*, 1992, **27**, 277-294.

23. J. Zhu, X. Meng and F. Xiao, *Frontiers of Chemical Science and Engineering*, 2013, **7**, 233-248.

24. C. H. Christensen, I. Schmidt and C. H. Christensen, *Catalysis Communications*, 2004, **5**, 543-546.

25. M.D. Lee, J.F. Lee, C.S. Chang and T.Y. Dong, *Applied Catalysis*, 1991, **72**, 267-281.

26. C. J. M. V. Rijn, *Nano and Micro Engineered Membrane Technology*, 2004.

27. P. A. Wright, *Microporous Framework Solids*, The Royal Society of Chemistry, 2008, 257-311.

28. M. Iwamoto, H. Furukawa and S. Kagawa, *Studies in Surface Science and Catalysis*, Elsevier, 1986, **28**, 943-949.

29. M. Iwamoto, H. Yahiro, T. Kutsuno, S. Bunyu and S. Kagawa, *Bulletin of the Chemical Society of Japan*, 1989, **62**, 583-584.

30. Y. Wan, J. Ma, Z. Wang, W. Zhou and S. Kaliaguine, *Journal of Catalysis*, 2004, **227**, 242-252.

31. C. T. Abreu, C. Henriques, F. R. Ribeiro, G. Delahay and M. F. Ribeiro, *Catalysis Today*, 1999, **54**, 407-418.

32. B. Coq, D. Tachon, F. Figuéras, G. Mabilon and M. Prigent, *Applied Catalysis B: Environmental*, 1995, **6**, 271-289.

33. W. X. Zhang, H. Yahiro, N. Mizuno, J. Izumi and M. Iwamoto, *Langmuir*, 1993, **9**, 2337-2343.

34. A. B. Shekhter, V. A. Serezhenkov, T. G. Rudenko, A. V. Pekshev and A. F. Vanin, *Nitric Oxide*, 2005, **12**, 210-219.

35. L. K. Keefer, *Nature Materials*, 2003, **2**, 357 - 358.

36. B. Wichterlová, J. Dědeček, Z. Sobalík, A. Vondrová and K. Klier, *Journal of Catalysis*, 1997, **169**, 194-202.

37. D. Nachtigallova, P. Nachtigall, M. Sierka and J. Sauer, *Physical Chemistry Chemical Physics*, 1999, **1**, 2019-2026.

38. H. Arai and M. Machida, *Catalysis Today*, 1994, **22**, 97-109.

39. W.X. Zhang, H. Yahiro, M. Iwamoto and J. Izumi, *Journal of the Chemical Society, Faraday Transactions*, 1995, **91**, 767-771.

40. W. V. Cruz, P. C. W. Leung and K. Seff, *Inorganic Chemistry*, 1979, **18**, 1692-1696.

41. P. S. Wheatley, A. R Butler, M. S. Crane, S. Fox, B. Xiao, A. G Rossi, I. L. Megson and R. E. Morris, *Journal of the American Chemical Society*, 2006, **128**, 502-509.

42. P. S. Wheatley, A. R. Butler, M. S. Crane, A. G. Rossi, I. L. Megson and R. E. Morris, *Studies in Surface Science and Catalysis*, Elsevier, 2005, **158**, 2033-2040.

43. B. Xiao, P. S. Wheatley and R. E. Morris, *Studies in Surface Science and Catalysis*, Elsevier, 2007, **170**, 902-909.

44. P. S. Wheatley, A. C. McKinlay and R. E. Morris, *Studies in Surface Science and Catalysis*, Elsevier, 2008, **174**, 441-446.

45. M. Mowbray, X. Tan, P. S. Wheatley, R. E. Morris, R. B. Weller, *Journal Investigative Dermatology*, 2008, **128**, 352–360.

46. B. Xiao, P. S. Wheatley, Z. Zhao, A. J. Fletcher, S. Fox, A. G. Rossi, I. L. Megson, S. Bordiga, L. Regli, K. M. Thomas and R. E. Morris, *Journal of American Chemical Society*, 2007, **129**, 1203-1209.

47. A. C. McKinlay, B. Xiao, D. S. Wragg, P. S. Wheatley, I. L. Megson and R. E. Morris, *Journal of the American Chemical Society*, 2008, **130**, 10440-10444.

48. P. G. Parzuchowski, M. C. Frost and M.E. Meyerhoff, *Journal of the American Chemical Society*, 2002, **124**, 12182-12191.

49. J. T. M. Koch, T. M. Reed and A. S. Borovik, *Angewandte Chemie International Edition*, 2004, **43**, 2806-2809.

50. A. K. Boes, P. S. Wheatley, B. Xiao, I. L. Megson and R. E. Morris, *Chemical Communications*, 2008, 6146-6148.

51. A.K. Boës, B. Xiao, I. Megson and R. E. Morris, *Topics in Catalysis*, 2009, **52**, 35-41.

52. D. S. Wragg, G. M. Fullerton, P. J. Byrne, A. M. Z. Slawin, J. E. Warren, S. J. Teat and R. E. Morris, *Dalton Transactions*, 2011, **40**, 4926-4932.

53. J. Yu and R. Xu, *Chemical Society Reviews*, 2006, **35**, 593-604.

54. S. T. Wilson, B. M. Lok, C. A. Messina, T. R. Cannan and E. M. Flanigen, *Journal of the American Chemical Society*, 1982, **104**, 1146-1147.

55. N. Rajic, *Journal of the Serbian Chemical Society*, 2005, **70**, 371-391.

56. W. Loewenstein, M. Loewenstein and C. S. Paulo, *American Mineralogist*, 1954, **39**, 92-96.

57. B. Chen and Y. Huang, *Microporous and Mesoporous Materials*, 2009, **123**, 71-77.

58. N. Venkatathri, *Journal of Scientific & Industrial Research*, 2005, **64**, 509-514.

59. S. Prasad and J F. Haw, *Chemistry of Materials*, 1996, **8**, 861-864.

60. K. A. Raj, A. Dayalan and V. R. Vijayaraghavan, *Indian Journal of Chemical Technology*, 2006, **13**, 329-333.

61. H. Hentit, K. Bachari, M. S. Ouali, M. Womes, B. Benaichouba and J. C. Jumas, *Journal of Molecular Catalysis A: Chemical*, 2007, **275**, 158-166.

62. X. Song, J. Li, Y. Guo, Q. Pan, L. Gan, J. Yu and R. Xu, *Inorganic Chemistry*, 2009, **48**, 198-203.

63. J. Li, J. Yu and R. Xu, *Proceeding of the Royal Society A*, 2012, **468**, 1955-1967.

64. X. Yang, H. Ma, Z. Xu, Y. Xu, Z. Tian and L. Lin, *Catalysis Communications*, 2007, **8**, 1232-1238.

65. D. Arias, l. Campos, D. Escalante, J. Goldwasser, C. M. López, F. J. Machado, B. Méndez, D. Moronta, M. Pinto, V. Sazo and M. M. R. de Agudelo, *Journal of Molecular Catalysis A: Chemical*, 1997, **122**, 175-186.

66. M. Hartmann and L. Kevan, *Research on Chemical Intermediates*, 2002, **28**, 625-695.

67. J. A. Martens and P. A. Jacobs, *Studies in Surface Science and Catalysis*, Elsevier, 1994, **85**, 653-685.

68. B. M. Weckhuysen, R. R. Rao, J. A. Martens and R. A. Schoonheydt, *European Journal of Inorganic Chemistry*, 1999, **1999**, 565-577.

69. N. Venkatathri and G. P. A. Kumar, *Indian Journal of Chemical Technology*, 2004, **11**, 843-847.

70. J. Q. Chen, *Indian Patent 252421*, 2012.

71. X. M. Chen, J. Xiao, Y. P. Zhu and Z. H. Luo, *Industrial & Engineering Chemistry Research*, 2013, **52**, 130226155651005-130226155653707.

72. L. Travalloni, A. C. L. Gomes, A. B. Gaspar and M. A. P. da Silva, *Catalysis Today*, 2008, **133–135**, 406-412.

73. H. Yang, Z. Liu, H. Gao and Z. Xie, *Journal of Materials Chemistry*, 2010, **20**, 3227-3231.

74. X. Guan, F. Zhang, G. Wu and N. Guan, *Materials Letters*, 2006, **60**, 3141-3144.

75. Q. Wang, L. Wang, H. Wang, Z. Li, H. Wu, G. Li, X. Zhang and S. Zhang, *Asia-Pacific Journal of Chemical Engineering*, 2011, **6**, 596-605.

76. A. T. Aguayo, A. E. S. d. Campo, A. G. Gayubo, A. Tarrío and J. Bilbao, *Journal of Chemical Technology & Biotechnology*, 1999, **74**, 315-321.

77. M. K. T. Ishihara, Y. Mizuhara and Y. Takita, *Chemistry Letters*, 1992, **21**, 2119-2122.

78. S. M. V. Valtchev and M. Tsapatsis, *Ordered Porous Solids Recent Advances and Prospects* 2009.

79. M. Hartmann and L. Kevan, *Research on Chemical Intermediates*, 2002, **28**, 619-619.

80. R. P. Bontchev and S. C. Sevov, *Chemistry of materials*, 1997, **9**, 3155-3158.

81. D. L. Vanoppen, D. E. De Vos, M. J. Genet, P. G. Rouxhet and P. A. Jacobs, *Angewandte Chemie International Edition in English*, 1995, **34**, 560-563.

82. S. S. Lin and H. S. Weng, *Applied Catalysis A: General*, 1993, **105**, 289-308.

83. J. Janchen, M. P. J. Peeters, J. H. M. C. van Wolput, J. P. Wolthuizen, J. H. C. van Hooff and U. Lohse, *Journal of the Chemical Society, Faraday Transactions*, 1994, **90**, 1033-1039.

84. M. Yoshimura and K.Byrappa, *Handbook of Hydrothermal Technology*, 2001, 335.

85. N. Li, G. Cao and S. Xiang, *Studies in Surface Science and Catalysis*, Elsevier, 2004, **154**, 1001-1006.

86. S. K. Ueda and W. Koizumi, *Proceeding of 6th International Zeolite Conference*, 1984.

87. X. Wenyang, L. Jianquan, L. Wenyuan, Z. Huiming and L. Bingchang, *Zeolites*, 1989, **9**, 468-473.

88. R. E. Morris and S. J. Weigel, *Chemical Society Review*, 1997, **26**, 309-317.

89. L. Wang, Y. P. Xu, B. C. Wang, S. J. Wang, J. Y. Yu, Z. J. Tian and L. W. Lin, *Chemistry – A European Journal*, 2008, **14**, 10551-10555.

90. R. E. Morris, *Chemical Communications*, 2009, 2990-2998.

91. J. E. W. Castner and J. F. Wishart, *Journal of Chemical Physics*, 2010, **132**, 120901-120909.

92. T. Welton, *Chemical Reviews*, 1999, **99**, 2071-2084.

93. C. Ye, W. Liu, Y. Chen and L. Yu, *Chemical Communications*, 2001, 2244-2245.

94. T. Welton and P. Wasserscheid, 'Ionic Liquids in Synthesis', *Wiley -VCH*, 2003,

95. J. S. Wilkes and M. J. Zaworotko, *Journal of the Chemical Society, Chemical Communications*, 1992, 965-967.

96. P. A. Z. Suarez, J. E. L. Dullius, S. Einloft, R. F. De Souza and J. Dupont, *Polyhedron*, 1996, **15**, 1217-1219.

97. K. R. Seddon, A. Stark and M. J. Torres, *Pure and Applied Chemistry*, 2000, **72**, 2275-2287.

98. L. Cammarata, S. G. Kazarian, P. A. Salter and T. Welton, *Physical Chemistry Chemical Physics*, 2001, **3**, 5192-5200.

99. J. G. Huddleston, A. E. Visser, W. M. Reichert, H. D. Willauer, G. A. Broker and R. D. Rogers, *Green Chemistry*, 2001, **3**, 156-164.

100. E. R. Parnham, E. A. Drylie, P. S. Wheatley, A. M. Z. Slawin and R. E. Morris, *Angewandte Chemie International Edition*, 2006, **45**, 4962-4966.

101. E. R. Cooper, C. D. Andrews, P. S. Wheatley, P. B. Webb, P. Wormald and R. E. Morris, *Nature*, 2004, **430**, 1012-1016.

102. A. P. Abbott, D. Boothby, G. Capper, D. L. Davies and R. K. Rasheed, *Journal of American Chemical Society*, 2004, **126**, 9142-9147.

103. S. Yang, A. G. Vlessidis and N. P. Evmiridis, *Microporous Materials*, 1997, **9**, 273-286.

104. M. Yoshimura and K. Byrappa, *Handbook of Hydrothermal Technology*, 2001, 331.

105. E. R. Parnham and R. E. Morris, *Accounts Chemical Research*, 2007, **40**, 1005-1013.

106. K. Egeblad, M. Kustova, S. K. Klitgaard, K. Zhu and C. H. Christensen, *Microporous and Mesoporous Materials*, 2007, **101**, 214-223.

107. E. M. Flanigen and R. L. Patton, *U.S Patent*, 1978, **4073**, 864.

108. Y. Wei, B. Marler, L. Zhang, Z. Tian, H. Graetsch and H. Gies, *Dalton Transactions*, 2012, **41**, 12408-12415.

109. M. Castro, R. Garcia, S. J. Warrender, A. M. Z. Slawin, P. A. Wright, P. A. Cox, A. Fecant, C. M. Draznieks and N. Bats, *Chemical Communications*, 2007, **0**, 3470-3472.

110. S. I. Zones, S. J. Hwang and M. E. Davis, *Chemistry – A European Journal*, 2001, **7**, 1990-2001.

111. R. H. Jones, A. M. Chippindale, S. Natarajan and J. M. Thomas, *Journal of the Chemical Society, Chemical Communications*, 1994, 565-566.

112. J. Yu, J. Li, K. Sugiyama, N. Togashi, O. Terasaki, K. Hiraga, B. Zhou, S. Qiu and R. Xu, *Chemistry of Materials*, 1999, **11**, 1727-1732.

113. J. Li, J. Yu, W. Yan, Y. Xu, W. Xu, S. Qiu and R. Xu, *Chemistry of Materials*, 1999, **11**, 2600-2606.

114. L. Wang, Y. Xu, Y. Wei, J. Duan, A. Chen, B. Wang, H. Ma, Z. Tian and L. Lin, *Journal of the American Chemical Society*, 2006, **128**, 7432-7433.

115. Y. Wei, Z. Tian, H. Gies, R. Xu, H. Ma, R. Pei, W. Zhang, Y. Xu, L. Wang, K. Li, B. Wang, G. Wen and L. Lin, *Angewandte Chemie International Edition*, 2010, **49**, 5200-5200.

116. Y. Wei, H. Gies, Z. Tian, B. Marler, Y. Xu, L. Wang, H. Ma, R. Pei, K. Li and B. Wang, *Inorganic Chemistry Communications*, 2010, **13**, 1357-1360.

117. H. Xing, J. Li, W. Yan, P. Chen, Z. Jin, J. Yu and S. Dai, R. Xu, *Chemistry of Materials*, 2008, **20**, 4179-4181.

118. D. K. Jr, *Science*, 1992, **258**.

119. M. McIntyre, D. F. Bohr and A. F. Dominiczak, *American Heart Association Journal*, 1999, **34**, 539-545.

120. L. J. Ignarro, *Nitric Oxide: Biology and Pathobiology*, 2000.

121. A. C. McKinlay, *PhD Thesis*, St. Andrews, 2010.

122. M. Kang, E. D. Park, J. M. Kim and J. E. Yie, *Applied Catalysis A: General*, 2007, **327**, 261-269.

123. Y. Traa, B. Burger and J. Weitkamp, *Microporous and Mesoporous Materials*, 1999, **30**, 3-41.

124. V. I. Pârvulescu, P. Grange and B. Delmon, *Catalysis Today*, 1998, **46**, 233-316.

125. L. Popova and T. Tuan, *Iranian Journal of Science and Technology Transaction A*, 2010, **34**, 173-183.

126. A. R. Butler and P. Rhodes, *Uses of Inorganic Chemistry In Medicine*, 1999.

127. A. R. Butler, F. W. Flitney and D. L. H. Williams, *Trends in Pharmacological Sciences*, 1995, **16**, 18-22.

128. J. S. Stamler, D. I. Simon, J. A. Osborne, M. E. Mullins, O. Jaraki, T. Michel, D. J. Singel and J. Loscalzo, *Proceedings of the National Academy of Sciences*, 1992, **89**, 444-448.

129. W. R. Pavanelli and J. J. N. Silva, *The Open Nitric Oxide Journal*, 2010, **2**, 1-6.

130. Q. Liu and S. S. Gross, *Methods in Enzymology*, 1996, **268**, 311-324.

131. U. Siddhanta, A. Presta, B. Fani, D. Wolan, D. L. Rousseaui and D. J. Stuehr, *Journal of Biological Chemistry*, 1998, **273**, 18950–18958.

132. E. B. Manukhina, H. F. Downey and R. T. Mallet, *Experimental Biology and Medicine*, 2006, **231**, 343-365.

133. A. B. Knott and B. B. Wetzel, *Antioxidants & Redox Signaling*, 2009, **11**, 541-553.

134. J. Loscalzo and G. Welch, *Progress in Cardiovascular Diseases*, 1995, **38**, 87-104.

135. D. Chakravortty and M. Hensel, *Microbes and Infection*, 2003, **5**, 621-627.

136. A. Butler and R. Nicholson, *Life, Death and Nitric Oxide*, The Royal Society of Chemistry, 2003, 1-11.

137. *Encyclopaedia Britannica Online*, 2013.

138. J. B. Lefkowitz, MD, *An Algorithmic Approach to Hemostasis Testing,* 2008.

139. R. K. Aggarwal, D. C. Ireland, M. A. Azrin, M. D. Ezekowitz, D. P. de Bono and A. H. Gershlick, *Circulation*, 1996, **94**, 3311-3317.

140. E. P. Strecker, A. Gabelmann, I. Boos, C. Lucas, Z. Xu, J. Haberstroh, N. Freudenberg, H. Stricker, M. Langer and E. Betz, *CardioVascular and Interventional Radiology*, 1998, **21**, 487-496.

141. A. Colombo, J. Drzeweicki, A. Banning, E. Grube, K. Hauptmann, S. Silber, D. Dudek, S. Fort, F. Schiele, K. Zmudka, G. Guagliumi and M. E. Russell, *Circulation*, 2003, **108**, 788-794.

# CHAPTER 2

# TECHNIQUES

## 2.1: X-Ray Diffraction[1-3]

### 2.1.1: Introduction and X-ray Generation

X-rays are electromagnetic radiation of wavelength about 1 Å ($10^{-10}$ m) and were discovered in 1895. Characteristic X-rays are generated when an energetic beam of electrons interacts with the inner shell electrons by inelastic scattering with enough energy to excite inner shell electrons to an outer shell, leaving inner-shell vacancies (Figure 2.1 (A)). These vacancies are subsequently filled by an electron from the higher energy level with emission characteristic called as X-ray photons (Figure 2.1 (B)).

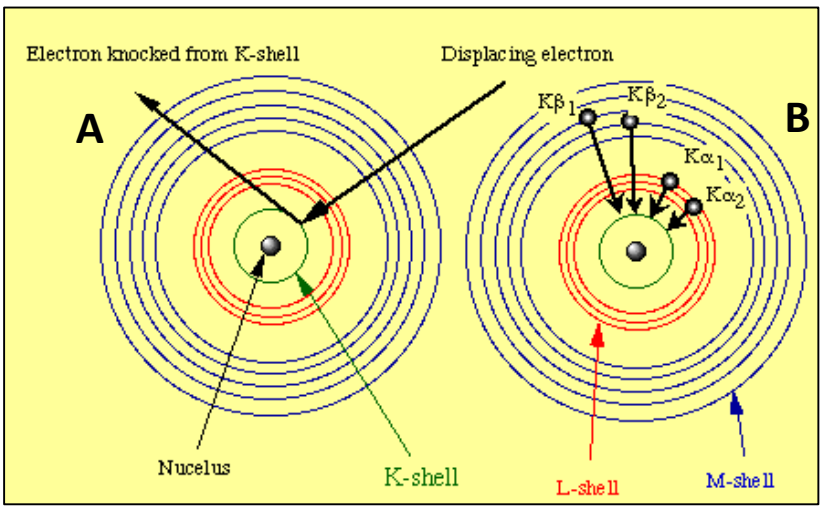


Figure 2.1: Generation of characteristic X-ray

Figure 2.2 shows a spectrum where the Kα-series is due to the photon emission when the electron transits from L to K-shell, while the Kβ-series is for the electron transits from M to the K-shell. Kα-series comprises three energy levels; $K\alpha_1$, $K\alpha_2$ and $K\alpha_3$ which are closely separated. However, they are not equally strong as $K\alpha_3$ is much weaker than $K\alpha_1$ and $K\alpha_2$ is half as intense as $K\alpha_1$. Therefore, in the spectrum Kα signal only shows two peaks and is denoted as Kα-doublet.[3]

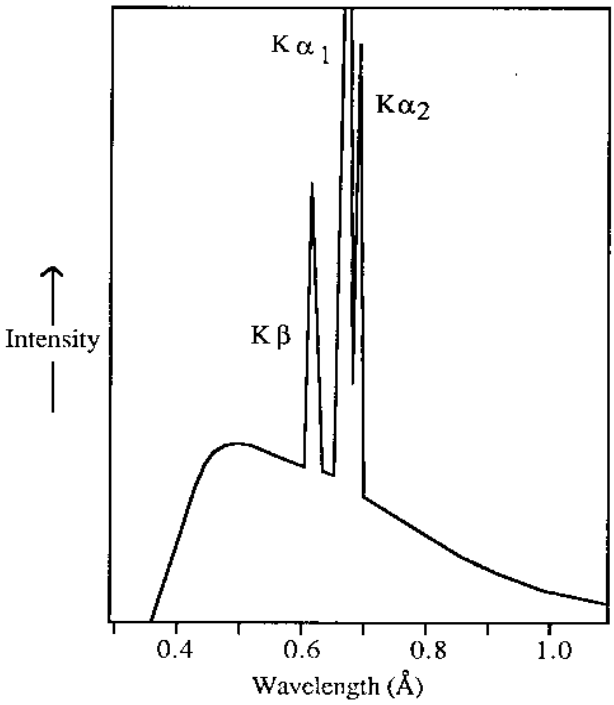


Figure 2.2: A typical spectrum of emitted X-rays from an X-ray tube.

## 2.1.2: Crystallography

A crystal is made up from a periodically repeating structural motif known as the unit cell. The unit cell as shown in Figure 2.3 is defined by six parameters, the length of the unit cell (a, b, c) and the angles between them (α, β, γ). This is the basic component of the structure, which, when repeated in three dimensions by translational moves only, makes up the complete structure (Figure 2.4).

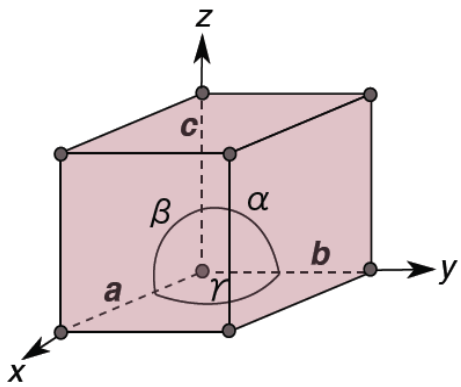


Figure 2.3: Representation of unit cell dimension with distance a, b, c along x, y and z and interaxial angles

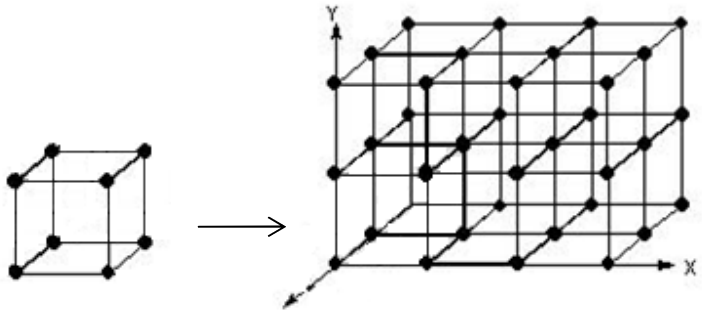


Figure 2.4: Representation of unit cell is repeated or translated by an integer number to form the whole crystal

There are seven crystal systems which can be identified by the constraints on the unit cell parameters (a, b, c, α, β, γ) as shown in Table 2.1. These seven crystal systems can be expanded into fourteen Bravais lattices by introducing additional centering: primitive (P), face centered (F), body centered (I) and side centered (A, B or C) lattices.

Symmetry elements can be defined by a point, line or plane. Symmetry operations are applied on symmetry elements, such as inversion through a point, rotation about a line and reflection in a plane lead to an arrangement that is the same as the initial arrangement. Each symmetry element provides a number of possible symmetry operators. The accumulation of symmetry elements that are compatible with translational symmetry give a 3-dimensional crystal, called a point group. There are 32 point groups of symmetry in the crystal systems. The combination of point groups and translation symmetries give 230 space groups that crystal structures can adopt. They are fully described in the International Tables for Crystallography.[4]

Table 2.1: The seven different crystal system

| **Crystal System** | **Bravais Lattice** | **Unit Cell Dimensions** | **Required Symmetry element** |
|---|---|---|---|
| Triclinic | P | $a \neq b \neq c$ , $\alpha \neq \beta \neq \gamma$ | None |
| Monoclinic | P, C | $a \neq b \neq c$ , $\alpha = \gamma = 90^{O} \neq \beta$ | One 2-fold axis or one symmetry plane |
| Orthorhombic | P,C, I, F | $a \neq b \neq c$, $\alpha = \beta = \gamma = 90^{O}$ | Any combination of three mutually perpendicular 2-fold axes or planes of symmetry |

| | | | |
|---|---|---|---|
| Rhombohedral | P | a = b = c, α = β =γ ≠ $90^O$ | One 3-fold axis |
| Trigonal | R | a = b ≠ c, α = β= $90^O$, γ = $120^o$ | |
| Hexagonal | P | a = b ≠ c, α = β= $90^O$, γ = $120^o$ | One 6-fold axis |
| Tetragonal | P, I | a = b ≠ c, α = β=γ = $90^O$ | One 4-fold axis |
| Cubic | P, I, F | a = b = c, α =β =γ = $90^O$ | our 3-fold axes |

## 2.1.3: Powder X-ray Diffraction

X-ray diffraction is constructed by the interaction of incident between beam of X-rays and the sample, which produces constructive interference when conditions satisfy Bragg's law ($n\lambda=2d \sin\theta$). This law relates to the wavelength of electromagnetic radiation (X-ray) to the diffraction angle and lattice spacing in the crystalline sample. Figure 2.5 illustrates Bragg's Law with the relationship between the incident beam of radiation and two parallel planes. Using the hypotenuse of the triangle ABz and applying trigonometry Bragg's law can be derived. The derivation of Bragg's law is shown below:

$$n\lambda = AB + BC \quad (2.1)$$

$$AB = d \sin\theta \quad (2.2)$$

Because $AB = BC$, so $n\lambda = 2AB$ (2.3)

Substituting equation (2.3) with (2.2):

$$\therefore \quad n\lambda = 2\,d\,\sin\theta \tag{2.4}$$

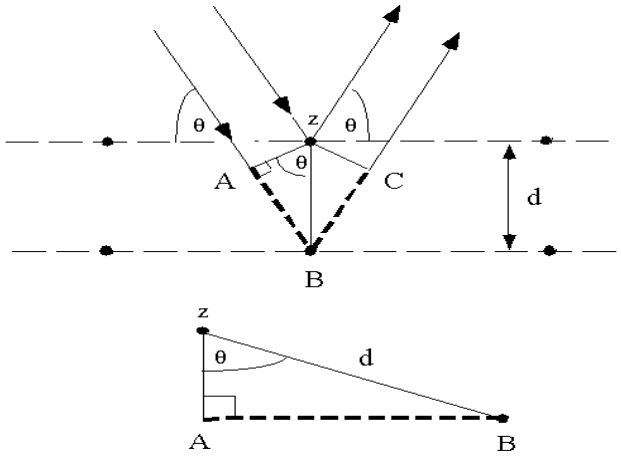


Figure 2.5**:** Bragg's Law as shown by interaction of two parallel planes

Powder X-ray Diffraction (PXRD) is an analytical technique used to characterise crystalline materials. The sample is typically a powdered material (polycrystalline) containing a very large number of small crystals, are known as crystallites, which are randomly oriented to each other. Figure 2.6 shows that when the sample is placed in the path of a monochromatic X-ray beam, the diffraction would occur from the planes in those crystallites that are oriented at the correct angle to fulfill Bragg's law. This figure also shows that the diffracted beam makes an angle 2θ with the incident beams which form cones of diffraction called Debye-Scherrer cones (Figure 2.7) with semi-apex angle equal to the deflection angle 2θ. Subsequently, the intersections of cones appear as rings on the flat area detector (Figure 2.8). This is different to single crystal sample where the X-ray diffraction gives single diffraction spots on the flat area detector. Finally

the angle and the intensity of the diffracted beam are recorded by the detector and plotted as intensity against 2θ to obtain a powder diffraction pattern.

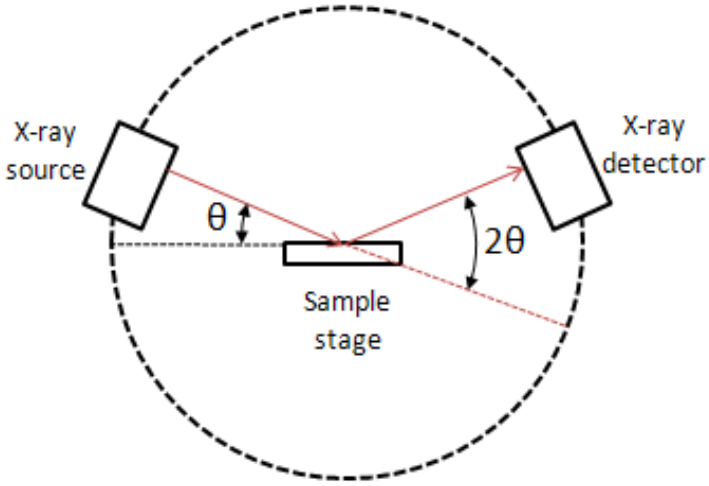


Figure 2.6**:** Schematic diagram of X-ray Diffractometer

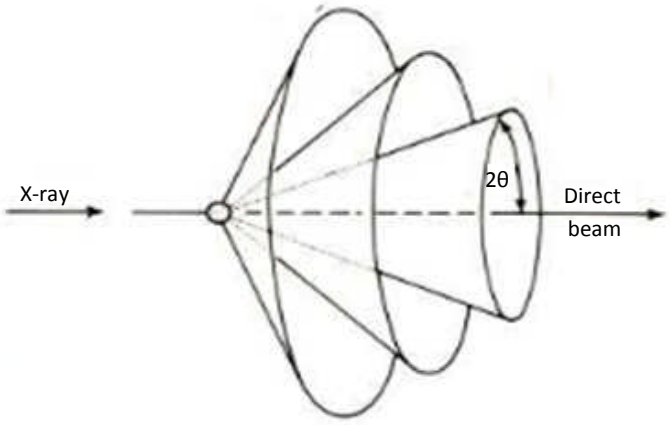


Figure 2.7: Debye-Scherrer cones

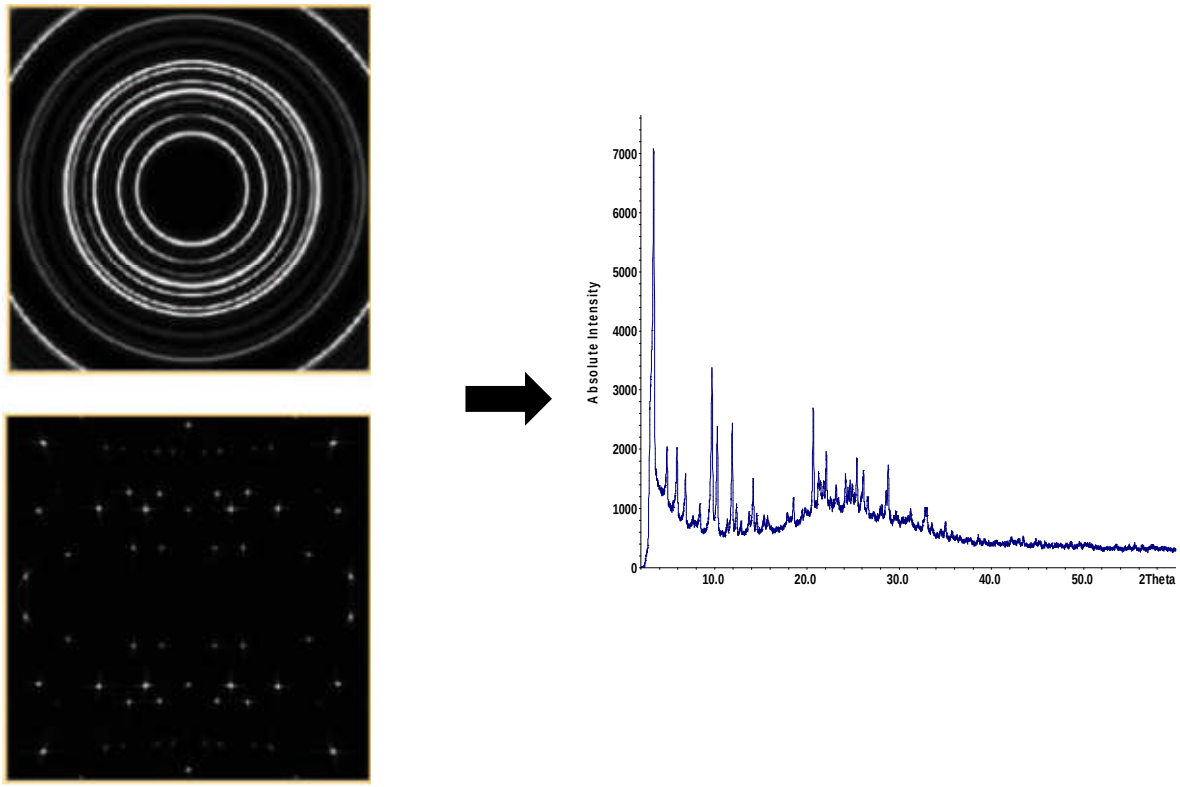


Figure 2.8: Example showing the difference between single crystal (bottom) and powder diffraction (top). The right is an example of a powder diffraction pattern

PXRD is primarily used for phase identification since the powder pattern can be seen as a finger print of the specific structure. This can be carried out by comparing the resultant experimental patterns with the theoretical patterns produced by using the Diamond 3 crystal visualisation software. The unit cell, space group and atom coordinates are inserted into the program to produce theoretical pattern that can used to compare to an experimental pattern. Instead of using this program, theoretical pattern also can be produced by using the existing cif file as an input.

The experimental powder pattern can be refined to fit a known structure model by that using a Rietveld refinement in General Structure Analysis System (GSAS)[5] program. The Rietveld method was introduced by Rietveld in 1969.[6] It is based on linear least-squares minimization on the residual (S) given by the equation 2.5:

$$S = \sum w_i |y_{io} - y_{ic}|^2 \quad (2.5)$$

Where, $y_{io}$ ,$y_{ic}$ and $w_i$ are the observed and calculated intensities respectively, and a suitable weight at the ith step.

The parameters that can be refined by this method include the lattice parameters, the atomic coordinates, temperature factors, peak shapes and intensity corrections. By refining profile parameters that only involve the diffractometer zero point, background shape and peak shape, the accurate lattice parameters can be obtained from a structure-less model. This is known as a Le Bail refinement and can also be used to extract intensities to obtain *hkl* file.

The reliability of the refinement can be judged by the calculation of several R-factors, the profile $R_p$ and the weighted profile $wR_p$:

$$R_p = \frac{\sum |y_{io} - y_{ic}|}{\sum y_{io}} \quad (2.6)$$

$$wR_p = \sqrt{\frac{\sum w_i - (y_{io} - y_{ic})^2}{\sum w_i y_{io}^2}} \quad (2.7)$$

$R_{exp}$ is a measure of the data quality; this factor should be close to the refined $wR_p$

$$R_{exp} = \sqrt{\frac{N-P}{\sum_i^N w_i y_{io}^2}} \quad (2.8)$$

Where, N and P are number of profile points and refined parameters respectively. This can be illustrated in the goodness of fit function $\chi$. This can be thought as a measure of how well the model structure fits the observed data (equation 2.9). A value that converges to unity indicates a good refinement.

$$\chi = \sqrt{\frac{\sum_i^N w_i (y_{io} - y_{ic})^2}{N-P}} = \sqrt{\frac{wR_P}{R_{exp}}} \quad (2.9)$$

Sometimes these factors can be misleading, so it is often helpful to examine at a plot of the observed and calculated profiles and their difference plot.

In this study the PXRD patterns were collected on a STOE STADI-P powder diffractometer using monochromated Cu $K\alpha_1$ (1.5406 Å) X-ray radiation as shown in Figure 2.9.

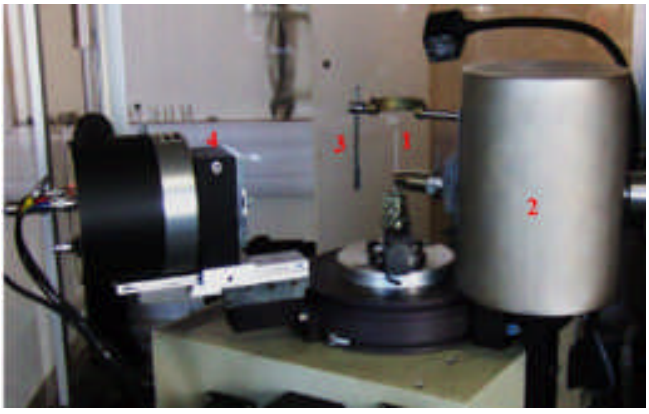


Figure 2.9: STOE STAD-P Powder X-ray Diffractometer; (1) sample holder (glass capillary), (2) X-ray source, (3) Beam Stop and (4) Detector [7]

## 2.2: Thermogravimetric Analysis

Thermogravimetric Analysis (TGA) is useful to quantify the mass change of sample with increasing temperature in a controlled manner under a gaseous atmosphere such as nitrogen or air. The procedure for analysis includes pre-weighing and zeroing alumina crucible before a few mg of sample is transferred into the crucible and re-weighed. Then the quantitative measurement of mass change in a material is recorded by the instrument. The mass change is associated with the material transition and thermal degradation of species in the material. Accordingly, the thermal stability and decomposition of material also can be determined. In this study, the samples have been analysed by using NETZSCH TG 209 instrument under air atmosphere and heated at rate of 10 °C $min^{-1}$to a maximum temperature of 650 °C.

## 2.3: Scanning Electron Microscopy and Energy Dispersive X-ray Analysis[1]

The scanning electron microscope (SEM) uses a focused beam of high-energy electrons to generate a variety of signals at the surface of solid specimens. The electron beam is produced by heating a filament, and focused by magnetic field in high vacuum. The high vacuum is required to prevent interaction of the beam with any extraneous particles in the atmosphere. The signals that derive from electron-sample interactions give information regarding the external morphology, chemical composition and crystalline structure of the sample. In most applications, the data are collected over a selected area of the sample surface. The 2-dimensional image of the material is generated and displayed electronically.

In electron microscopy, the elements present in the sample also emit characteristic X-rays. The X-ray are separated by a silicon-lithium detector where the each signal is collected, amplified and corrected for absorption and other effects. The signal gives both quantitative and qualitative analysis of the elements present (for the atomic number greater than 11) in the irradiated particle. This technique is known as energy dispersive X-ray analysis (EDAX or EDX).

In this study the SEM and EDX analysis of samples have been performed using a higher resolution transmission microscope Jeol JSM 5600 SEM.

## 2.4: Nuclear Magnetic Resonance [8, 9]

Nuclear Magnetic Resonance (NMR) is another spectroscopic technique using radio waves as the electromagnetic radiation to obtain chemical and structural information of a compound. In NMR the radio waves are adsorbed by atomic nuclei when placed in a strong magnetic field, resulting in a transition between nuclear spin states. Only atomic nuclei with non-zero spin quantum number (***I***) (Table 2.2) possess a magnetic moment and are amenable to NMR observation. When atomic nuclei with spin $I \neq 0$ are placed into a magnetic field, they exhibit quantisation of their orientation, depending on ***I***. Thus, when the magnetic field is applied to atomic nuclei with $I \neq 0$, the nuclei can adopt $(2I + 1)$ orientations in the field.

Table 2.2: Atomic nuclei and spin

| Atomic Number | Mass number | Spin, I | Examples (natural abundance/%) |
|---|---|---|---|
| Even | Even | 0 | $^{12}$C(98.89), $^{16}$O (99.76), $^{32}$S (95.04) |
| Odd/even | Odd | ½, 3/2, 5/2, etc. | $^{1}$H (99.99), $^{13}$C (1.11), $^{19}$F(100), $^{31}$P (100), all *I*= ½ |
| Odd | Even | 1, 2, 3, etc. | $^{14}$N(99.64), $^{2}$H(0.015) both *I*=1 |

When a nucleus with spin $\boldsymbol{I}$ = ½ (e.g. $^{1}$H, $^{l3}$C, $^{l9}$F and $^{31}$P) is placed in an applied magnetic field, $\boldsymbol{B_o}$, two spin states arise ($\boldsymbol{m_I}$ = +1/2, $\boldsymbol{m_I}$ = -1/2) which make NMR spectroscopy possible, as shown in Figure 2.10

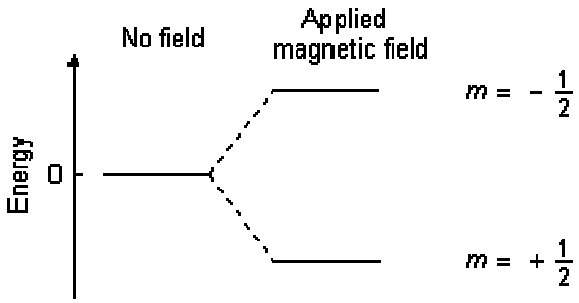


Figure 2.10: Energy levels for a nucleus with spin quantum number ½

The difference in energy between these two states is given below:

$$E = \frac{\gamma h B o}{2\pi} \qquad (2.10)$$

Where $B_o$ is the strength of the applied magnetic field, $\gamma$ is the gyromagnetic ratio for the nucleus and $h$ is Plank's constant. The radiation frequency, $\nu$, which corresponds to the energy, and it also called as resonance frequency is given by equation 2.11.

$$\nu = \frac{\gamma Bo}{2\pi} \tag{2.11}$$

## 2.4.1: Chemical Shift

Chemical shift is an important characteristic of NMR because it helps to differentiate between nuclei. It arises when the effective magnetic field ($B_{eff}$) experienced by the nucleus is not equal to the applied magnetic field ($B_0$). This is due to motion of electrons surrounding the nucleus, which results in induced magnetic fields. Therefore the nucleus is said to be 'shielded' from the external field by its surrounding electrons. The $B_{eff}$ field at the nucleus can be expressed as in equation 2.12.

$$B_{eff} = B_o(1 - \sigma) \tag{2.12}$$

Where, $\sigma$ is shielding constant. The actual resonance frequency of the nucleus can then be written as shown in equation 2.13.

$$\nu = \frac{\gamma Bo(1-\sigma)}{2\pi} \tag{2.13}$$

The variation in resonance frequency due to the electronic environment of a nucleus is called the chemical shift and it is shown in parts per million (ppm). This can be expressed in equation 2.14.

$$\delta = \frac{V - V_{ref}}{V_{ref}} \, x \, 10^6 \qquad (2.14)$$

Where, $V$ is the resonance frequency of the nucleus of interest and $V_{ref}$ is a reference resonance frequency.

## 2.4.2: Solution NMR

Solution NMR is very useful in identification and characterization of organic molecules. In this study both $^{1}H$ and $^{13}C$ solutions NMR have been used to characterise the phase and purity of the ionic liquids. These analyses have been performed using Bruker Avance 300 and Bruker Avance II 400 spectrometers which operate at frequencies of 300 MHz and 400 MHz, respectively. All the data have been collected by using Topspin2 NMR software.

## 2.4.3: Solid State NMR [10-14]

Solid state NMR has significant differences from solution state NMR. In solution NMR, spectra consist of a series of very sharp, narrow and well-defined peaks (Figure 2.11) due to the rapid tumbling of molecules in the liquid, giving an average isotropic value of zero. By contrast, in the solid state, there is no random diffusion or tumbling of molecules. The nuclear spin interactions in solid state such as dipolar coupling, chemical shift anisotropy and quadrupolar interaction result in a broadening of the spectral lines of NMR (Figure 2.11). All these factors depend on the

crystallites orientation which are said to be anisotropic (orientation dependent). The resulting broad peak is composed of millions of single crystals with different orientation, with respect to $B_o$. These broadenings can be overcome by using techniques such as magic-angle spinning and high power decoupling.

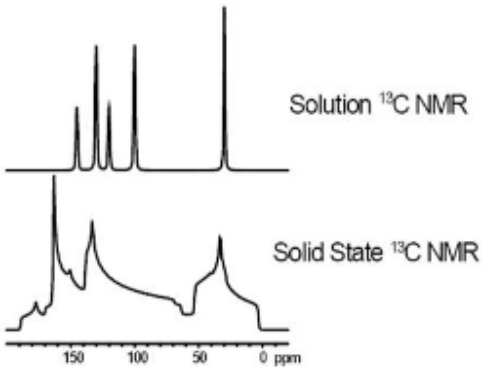


Figure 2.11: Comparison of Solution State NMR and Solid State NMR

## 2.4.3.1: Dipolar interaction

Nuclear spins have a magnetic moment and in a collection of spins these can interact with each other. This is called dipolar interaction. In solution this interaction is averaged to its isotropic value of zero by molecular tumbling. However this is not the case in solids where this interaction is a major cause of line broadening.

The strength of the dipolar interaction between two spins j and k can be expressed in equation 2.15. The strength of the interaction is proportional to the gyromagnetic moments of the nuclei and inversely proportional to the cubed distance between spins.

$$B_{jk} = \left(\frac{\mu_0}{4\pi}\right)\frac{\hbar\,\gamma_j\,\gamma_k}{r_{jk}^3} \tag{2.15}$$

For spins $(\hat{I})$ of the same isotopic species, e.g. homonuclear species, the dipole-dipole interaction is given by equation 2.16:

$$\hat{H}_{jk}^{DD}(\theta_{jk}) = B_{jk}\frac{1}{2}\left(3cos^2\theta_{jk} - 1\right)\left(3\hat{I}_{jx}\hat{I}_{kx} - \hat{I}_j\hat{I}_k\right) \tag{2.16}$$

Where, $\theta_{jk}$ is the angle between the spin vector and $B_0$, which is shown in Figure 2.12.

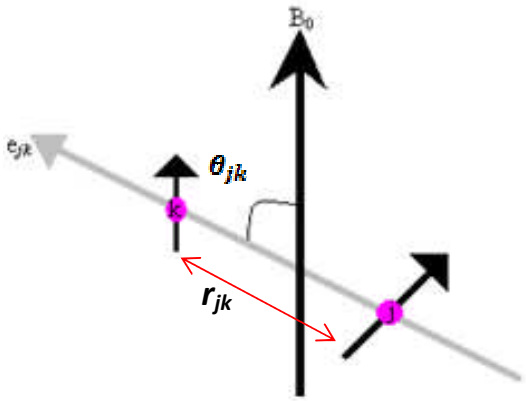


Figure 2.12: Illustration of two spins k and j that may interact in the formation of $\theta_{jk}$.

For spins of different isotopes, e.g., heteronuclear species, the dipole-dipole interaction is given by equation 2.17:

$$\hat{H}_{jk}^{DD}(\theta_{jk}) = b_{jk}\frac{1}{2}\left(3cos^2\theta_{jk} - 1\right)2\hat{I}_{jx}\hat{I}_{kx} \quad (2.17)$$

Both equations of homo- and heteronuclear dipole-dipole interactions include dipole-dipole coupling as defined in equation 2.18:

$$d_{jk} = b_{jk}\frac{1}{2}\left(3cos^2\theta_{jk} - 1\right) \quad (2.18)$$

Dipolar coupling is equal to zero when $\theta_{jk}$ satisfies the equation 2.19:

$$\left(3cos^2\theta_{jk} - 1\right) = 0 \quad (2.19)$$

The solution to equation 2.19 is known as the magic angle (θ = 54.74º).

## 2.4.3.2: Quadrupolar interaction

Over two thirds of elements in the periodic table have a spin quantum number (I) greater than ½. These nuclei are known as quadrupolar nuclei. Those with an odd half integer spin quantum number, i.e. I = 3/2, 5/2, 7/2 etc, are abundant in inorganic materials and give rise to a quadrupole moment (eQ) which interacts with the electric field gradient ($V_{zz}$) present at the nucleus. This interaction is anisotropic in nature and therefore orientation dependent with respect to $B_0$, producing broad lines in solids, but it is averaged in liquids by the rapid molecular motion. The magnitude of this interaction is defined by the Quadrupolar coupling constant ($C_Q$) and measured in Hertz (equation 2.20).

$$C_Q = eQV_{zz}/h \tag{2.20}$$

A quadrupolar constant equal to zero demonstrates the high symmetry, the symmetry of the system decreases when $C_Q$ increases. The broadening from quadrupolar interactions can be very large and sometimes be known as the dominant interaction in solid-state NMR.

## 2.4.3.3: Chemical Shift Anisotropy

In a single crystal all molecules have the same orientation with respect to $B_0$. Different single crystals will have a different orientation with respect to $B_0$ and so they have different chemical shift (δ) (Figure 2.13 (a)). Powder sample composed of millions of single crystals with different orientations resulting in a characteristic broad powder pattern lineshape (Figure 2.13 (b)), which difficult to resolve.

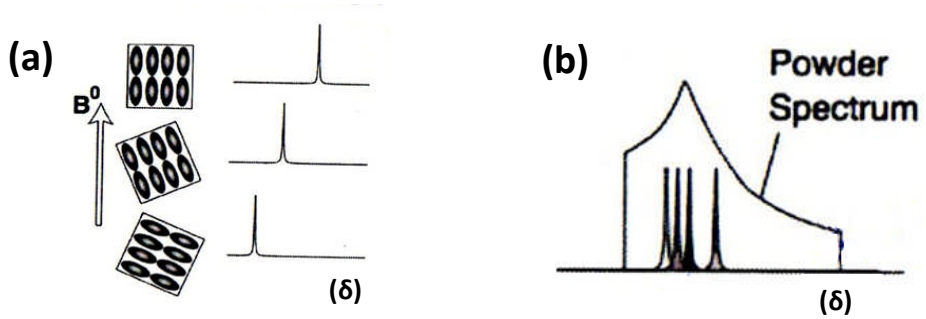


Figure 2.13: (a) Chemical shift of single crystal with different orientation and (b) Characteristic powder pattern of solid state NMR.

## 2.4.3.4: Paramagnetic effect[15]

Paramagnetic centres result from the unpaired electrons that exist in organic radicals and many transition metal ions. The interaction between paramagnetic centre with surrounding nuclear spins change the appearance of NMR spectra by altering chemical shifts and increasing relaxation rates. The arising of paramagnetic effect depends on the nature of the metal's electronic configuration and the structure of the molecule. It therefore, provides variety information on the electronic states of the paramagnetic center, as well as number its surrounding environment.

## 2.4.3.5: Magic Angle Spinning

Magic Angle Spinning (MAS) exploits the fact that dipolar couplings and chemical shift anisotropy have similar orientation dependence. In order to remove the broadening in a powdered sample, all the crystallites must have the same orientation simultaneously. It has been noted that the anisotropic effects of the chemical shift and dipolar interaction are averaged to zero when the sample is oriented at 54.74˚ of magic angle spinning (Figure 2.14) and spun very fast. Consequently the resolution and sensitivity of the spectrum is improved.

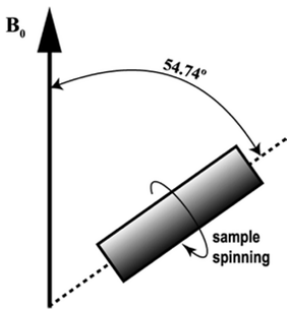


Figure 2.14:- Magic Angle Spinning (MAS)

## 2.4.3.6: Cross Polarisation

Cross polarization technique can be used to perform some spectral editing and to obtain information on which dilute spins that are close in space. Observing dilute spins such as $^{13}C$ or $^{15}N$ presents a number of problems which including poor signal-to ratio due to the low abundance. In addition, the relaxation times of the low abundance nucleus tend to be very long. This is due to the absence of strong homonuclear dipolar interactions which can stimulate relaxation transition. Only weaker heteronuclear dipolar interactions are present. Long relaxation times indicate that the long gaps must be left between scans, normally of the order of minutes. When several thousand scans are required to lower the noise to a suitable level, collecting spectra can take a very long time. Therefore, to solve these particular problems, the polarization from abundant spins such as $^{1}$ H or $^{19}F$ is transferred to dilute spins such as $^{13}C$ or $^{15}N$. This technique is known as cross polarization. After magic angle spinning, cross polarization is one of the most widely used technique in solid state NMR.

For cross polarization to work, there must be dipolar coupling between H and X. The technique requires a double channel probe as both spin systems must be excited. The pulse sequence, shown in Figure 2.15, starts with a short 90° pulse on the H-channel, then promptly followed by a pulse application on y-channel, i.e. one which is phase shifted by 90º to the original pulse. This is called a spin-lock pulse. Within this time the pulse is applied to the X-channel for a period of time which known as the contact time. After the contact time, a FID is obtained in the X-channel during proton decoupling. This is known as the acquisition time.

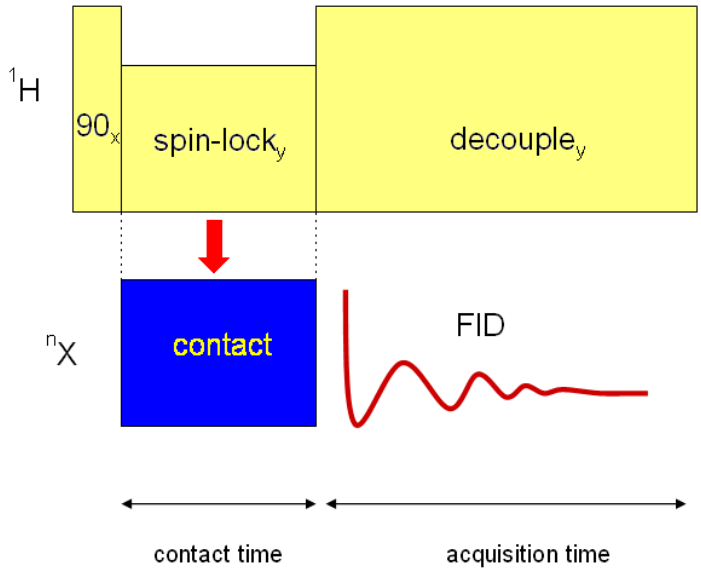


Figure 2.15: Cross Polarisation; The Pulse Sequence.[13]

## 2.4.3.7: $^{31}$ P NMR Spin-echo mapping technique[16-20]

Relaxation time is a property of the nucleus that reflects its properties and environment. The mechanisms of relaxation of the individual nuclear spins can be categorized into longitudinal relaxation time ($T_1$) that describes the return of the z-component of magnetisation to its thermal equilibrium state and $T_2$, which is the time of transverse (x,y) relaxation of magnetization component. In solids, generally $T_2$ is shorter than $T_1$. In materials that contain paramagnetic ions *e.g* in AlPO, the strong pseudocontact and hyperfine interaction of unpaired electrons of paramagnetic transition cations with $^{31}$P nuclei increases the rate of time nuclear relaxation ($T_1$ and $T_2$) drastically broadens the spectrum line width and observed shift. Consequently, the $^{31}$P signal produced is very low and cannot be detected using a conventional $^{31}$ P MAS NMR

sequence. In order to overcome this problem, spin-echo technique can be applied to record the total $^{31}P$ NMR spectrum. Schematically, spin- echo mapping consists of recording a series using Hahn echo sequence at different frequencies (Figure 2.16). In Hahn echo sequence the spin flips 90$^{o}$, followed by an inter-pulse delay time, (τ), then the spin flip 180$^{o}$, followed by a second inter-pulse delay (τ). A whole "spin echo" is acquire at echo time, 2τ. Once the spectrum acquired, the intensity is corrected, taking into account the relaxation of the magnetization before acquisition of the signal. The total signal is obtained by the sum of all individual spectra.

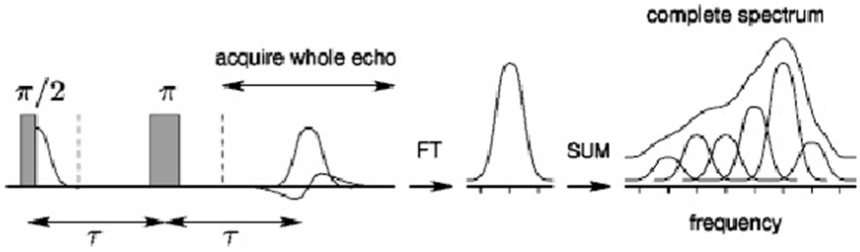


Figure 2.16: Schematic diagram of spin-echo mapping technique used in recording broad phosphorus NMR spectra. The vertical dashed lines correspond to the instrumental dead time after each radio frequency pulse

As mentioned, the $^{31}P$ NMR spectrum is affected by unpaired electrons of paramagnetic transition metal ions. The influence of the single paramagnetic centre can be expressed through an effective magnetic field formed in the equation below:

$$B_{en} = \frac{2\pi A_{iso}}{\gamma_n}\langle S\rangle + \mu_0\mu_B g\frac{3cos^2\theta-1}{r^3}\langle S\rangle \qquad (2.21)$$

Where, $A_{iso}$ is the constant of isotropic hyperfine coupling, $\gamma_n$ is the nuclear gyromagnetic ratio, $\mu_B$ is the Bohr magneton, $r$ is the separation between electronic and nuclear spins, $S$ is spin polarization and $\theta$ is the angle between the electron-nucleus vector and the external magnetic field.

According to the equation 2.21, the first term come from the hyperfine coupling which is responsible for isotropic shift of $^{31}$P NMR lines. The second term comes from the electron-nucleus pseudocontact which has angular dependence and thus causes broadening of the $^{31}$P NMR lines in powders.

Only samples with low levels of metal ions experiences the interaction with single paramagnetic centres. For samples with higher level of transition metal ions, the contribution of several paramagnetic centers should be considered, where the rapid electron spin relaxation also has be taken into account in the equation above. Therefore, the electron spin quantum number can be replaced with average electron spin polarisation $\langle S \rangle$. This can be defined as:

$$\langle S \rangle = \frac{\mu_B g B_0 S(S+1)}{3kT} \tag{2.22}$$

This indicates that transition metal ions with bigger spin quantum number $S$ will increase NMR line broadening and, if $A_{iso}$ is fixed, a larger paramagnetic shift is produced.

In this study, spin-echo mapping has been performed using Bruker Avance III spectrometer equipped with a 9.4 T wide-bore superconducting magnet, operating at Larmor frequency of 161.976 MHz for $^{31}$P. The radio frequency power was ~180 kHz (90 degree pulse of 1.4 ms) and the echo delay was 10 ms. Signal averaging was carried out for 10240 transients for each frequency step with a repeat interval of 0.1 s. Frequency stepping was carried out as needed

and spectra for each frequency step were processed and then codded to give the final spectrum.

## 2.5: CHN Analysis

CHN elemental analysis has been used to establish the percentage amount of carbon, hydrogen and nitrogen in samples. It is useful to determine whether organic molecules are present within the sample frameworks. The elemental analysis was performed by using a Carlo Erba 1106 CHN elemental analyser.

## 2.6: NO Analyser

In this study, the amount of nitric oxide (NO) released from samples was measured using a 280i chemiluminescence Nitric Oxide Analyser from Siever instruments. This instrument is provided with a sensitive detector to measure NO based on a gas-phase chemiluminescent reaction between NO and ozone ($O_3$):

$$NO + O_3 \longrightarrow NO_2^{\bullet} + O_2$$

$$NO_2^{\bullet} \longrightarrow NO_2 + hv$$

The emission from the electronically exited nitrogen oxide is in the red and near-infrared spectrum region are detected by a red-sensitive photomultiplier.

## 2.7: References


1. L. E. Smart and A. Moore, *Solid State Chemistry - An Introduction*, Taylor & Francis, 2005.
2. P. Muller, R. H. Irmer, A. Spek, T. Schneider and M. Sawaya, *Crystal Structure Refinement: A Crystallographer's Guide to SHELXL*, Oxford University Press, 2006
3. C. Hammond, *The Basic of Crystallography and Diffraction,* Oxford University Press, 2009.
4. M. G. Rossman and E. Arnold, *International Tables for Crystallography*, Kluwer Academic Publisher, 1996.
5. A. C. Larson and R. B. V. Dreele, *Los Alamos Nationality Laboratory Report LAU,* 2004, 86-748.
6. P. H. J. Latiere, *Journal of Applied Crystallography*, 1969, **2**, 52-55.
7. M. I. H. Mohideen, *PhD Thesis*, St Andrews, 2011.
8. R. J. Anderson, D. J. Bendell and P. W. Groundwater, *Organic Spectroscopic Analysis*, The Royal Society of Chemistry, 2004, **22**, 51-119.
9. A. K. Briston, *Inorganic Spectroscopic Methods,* Oxford Chemistry Primers, 1998.
10. S. P. Brown and L. Emsley, *Handbook of Spectroscopy*, Wiley-VCH Verlag GmbH & Co. KGaA, 2005.
11. M. J. Duer, *Introduction to Solid State NMR Spectroscopy*, Wiley, 2004.
12. P. J. Byrne, *PhD Thesis*, St Andrews, 2009.
13. S. R. Miller, *PhD Thesis*, St Andrews, 2008.
14. M. J. Duer, *Solid-State NMR Spectroscopy Principles and Applications*, Blackwell Science, 2002.
15. G. Pintacuda and G. Kervern, *Modern NMR Methodology*, 2013, **335**, 157-200.

16. A. R. Gregor Mali, A. Ristic and V. Kaućić, *The Journal of Physical Chemistry B*, 2005, **109**, 10711-10716.

17. Y. Y. Tong, *Journal of Magnetic Resonance, Series A*, 1996, **119**, 22-28.

18. M. T. Sananes and A. Tuel, *Solid State Nuclear Magnetic Resonance*, 1996, **6**, 157-166.

19. M. T. Sananes and A. Tuel, *Journal of the Chemical Society, Chemical Communications*, 1995, 1323-1324.

20. L. Canesson and A. Tuel, *Chemical Communications*, 1997, 241-242.

# CHAPTER 3

# IONOTHERMAL SYNTHESIS AND CHARACTERISATION OF CoAPO-34

## 3.1: Introduction

As mentioned in Chapter 1, the alternation of $Al^{3+}$ and $P^{5+}$ means that aluminophosphates (AlPOs) with ratio of Al:P equal to 1:1 are chemically neutral.[1] However, a charge imbalance can occur when a heteroatom such as a transition metal cation with a different charge (e.g $Fe^{2+}$, $Co^{2+}$, $Cu^{2+}$ etc.) is incorporated within the framework, and subsequently the framework may become catalytically active. The material formed by this substitution is called metal aluminophosphate (MAPO).

Cobalt-substituted aluminophosphate (CoAPO) is extensively studied mainly due to its potential use as a solid-acid catalyst and the possibility of redox reaction.[2] A Brønsted acid site in CoAPO material is generated by substitution of $Al^{3+}$ with $Co^{2+}$ ion and the negative charge produced is compensated by a proton. Normally the redox properties of CoAPO are expected from the possible reversible oxidation of $Co^{2+}$ to $Co^{3+}$. [2]

Several reports of CoAPOs have appeared and mainly the compounds were prepared under hydrothermal synthesis. For example CoAPO-36 with the ATS topology [3] as shown in Figure 3.1, possesses high acidity and displays good catalytic performance in the conversion of aliphatic and aromatic hydrocarbon especially in the conversion of 3-methylpentane and o-xylene.[4]

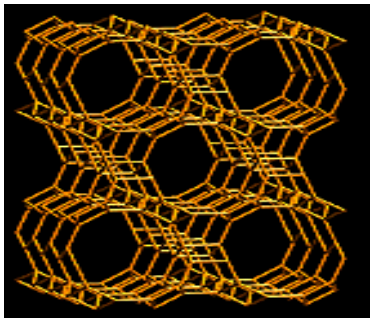

Figure 3.1: AST topology [5]

Another good example is CoAPO-18. This compound has the AEI framework structure[6] (Figure 3.2), is very active and serves as a selective Bronsted acid catalyst for methanol conversion to light olefins.[7]

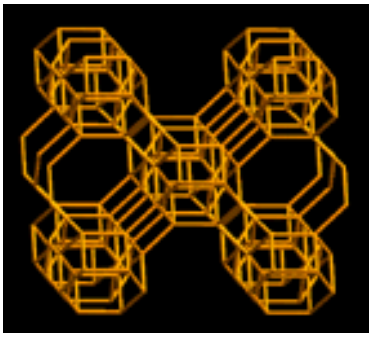

Figure 3.2: AEI topology [5]

Recently, ionothermal synthesis has been developed to prepare CoAPO molecular sieves since the peculiar properties of IL or eutectic mixture (EM)/deep-eutectic solvent (DES) endow many interesting features and potential advantages over the traditional method in synthesis of porous material. As examples, in the ionothermal synthesis, IL or EM/DES can act as both solvent and template in the reaction. Furthermore, the low vapor pressure of IL or DES allows the synthesis occur at ambient pressure, therefore eliminating the safety concern associated with high hydrothermal pressure.[8]

To date several studies have been reported concerning the synthesis of CoAPOs using IL such as SIZ 8 (AEI), SIZ 9 (SOD), and SIZ 7 as shown in Figure 3.3. These materials have been prepared using an IL of 1-ethyl-3- methylimidazolium bromide (EMIMBr). They are interesting materials because they have potential to use in gas separation and gas storage application.[9]

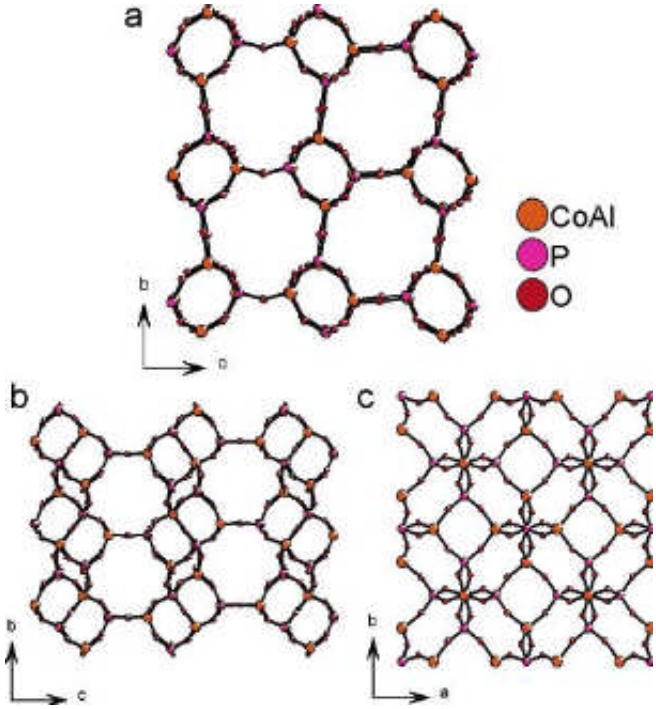


Figure 3.3: Diagram of the three cobalt aluminophosphates zeolite framework (a) SIZ 7, (b) SIZ 8 (AEI) and (c) SIZ 9 (SOD).[9]

Moreover, three CoAPO materials (Figure 3.4) have been successfully prepared using choline chloride–succinic acid EM. They are CoAPO zeolite analogous to levyne (LEV) structure (SIZ 14), a novel material (SIZ 15) and unusual zeolite-related layered material which the cobalt atoms are ordered with Co-Cl bond (SIZ 13). Normally a Co-Cl bond in zeolite compound is not accessible when made hydrothermally because it is extremely sensitive to hydrolysis in the

presence of excess water. However, this problem has been solved under ionothermal condition using DES where the deactivation of water by strong interaction with the anion in DES appeared to reduce hydrolysis activity hence allowing the synthesis of Co-Cl bond in the zeolite material. Clearly, using ionothermal synthesis reveals many new possibilities in the synthesis of zeolites, zeolite analogues and other areas.[10]

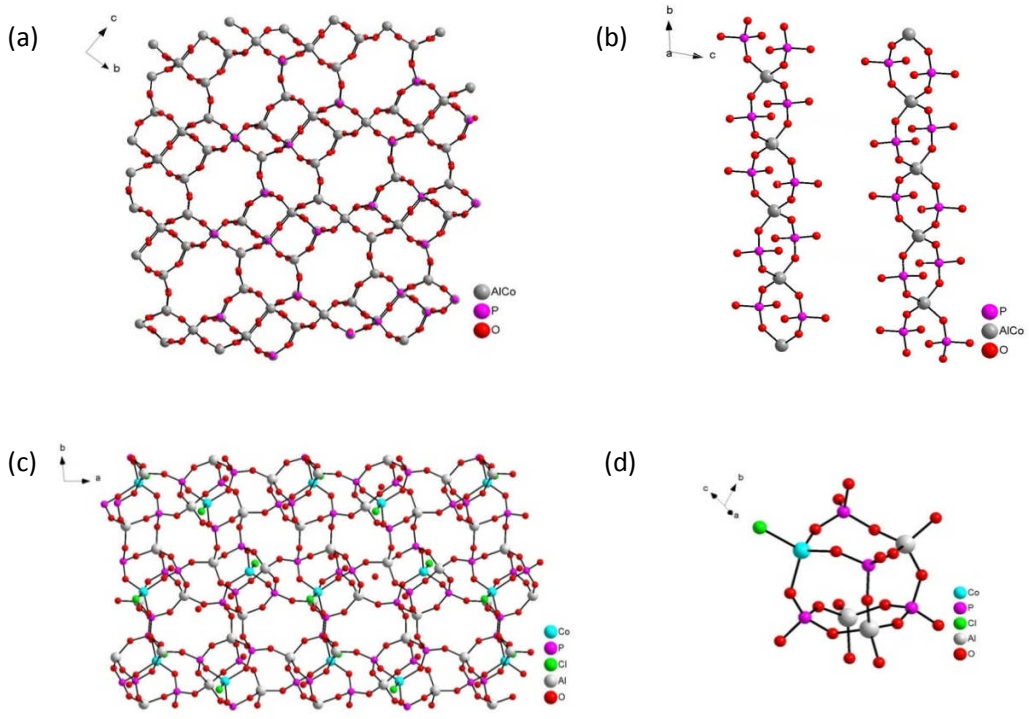


Figure 3.4: The structure of (a) SIZ 14 (LEV), (b) SIZ 15, (c) SIZ 13 and (d) ring-opened unit in SIZ 13 [10]

In this study, ionothermal synthesis of CoAPO-34 using 1-ethyl-3-methylimidazolium bromide (EMIMBr) (Figure 3.5) in the presence of 1,6-hexadiamine (HDA) (Figure 3.6) has been explored. This compound has usually been hydrothermally prepared and the first synthesis has been reported by Union Carbide in 1985. [11] To date there has been no report of the ionothermal synthesis of CoAPO-34. Therefore, in this study the ionothermal synthesis is explored to provide an alternative route to prepare CoAPO-34 under low pressure instead of higher pressure which is associated with hydrothermal or solverthermal condition.

CoAPO-34 is chosen because this material is topologically identical to the aluminophosphate-34 ($AlPO_4$-34) with the chabazite (CHA) structure[12]. AlPO-34 framework contains 8, 6 and 4 rings as shown in Figure 3.7.[13] This structure can also feature fluoride atom bridging two Al atoms (increasing Al coordination number to six) and the double-6-rings (D6R) connected through 4-membered rings, resulting in a three dimensional structure of CHA cages.[14] The fluoride ions present charge balance the protonated organic molecule located in the CHA cage.[15] CHA-like aluminophosphate have found interest for their adsorptive and catalytic properties[12] while CoAPO-34 is used as catalyst in oxidation of NO to $NO_2$ [16] and also used in the conversion of methanol to olefin.[17]

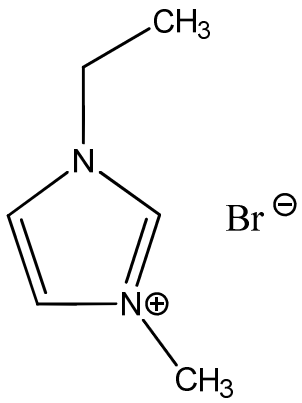


Figure 3.5: 1-ethyl-3-methylimidazoliumbromide (EMIMBr)

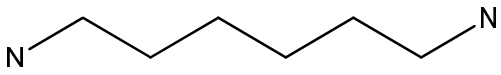


Figure 3.6: 1, 6-hexadiamine

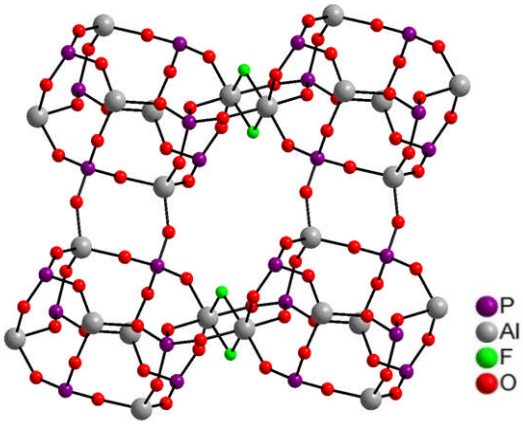


Figure 3.7: The triclinic structure of $AlPO_4$-34[13]

## 3.2: Aims

The aim of this study is to explore the ionothermal synthesis of CoAPO-34 using 1-ethyl-3-methylimidazoliumbromide (EMIMBr) ionic liquid (IL) and addition of 1, 6-hexanediamine (HDA). Any effect upon to the structure produced by using different amounts of HF, varying amounts of EMIMBr and the absence of HDA in the reaction are reported. The materials are characterised using PXRD, TGA, SSNMR, elemental analysis using EDX and CHN and SEM.

## 3.3: Materials and Methodology

### 3.3.1: Synthesis of 1-ethyl-3-methylimidazolium bromide (EMIMBr)

EMIMBr was synthesized according to the Reference 18 with the following modification. Under inert atmospheric conditions, degassed ethylbromide (75.70 g, 0.7mol, Aldrich) was added to 48.00 g (0.6mol) of *N*-methyl imidazole (Aldrich, 99%) with constant stirring. This mixture was refluxed at 40 $^{o}$C for 3 hours and allowed to cool to room temperature. Then ethylacetate (Fisher, 99%) was added to the solution and the product crystallised from the solution. The white product is filtered and washed with ethylacetate. The product was dried under vacuum 40$^{o}$C for 10 hours and stored under an inert atmosphere. Then the product was determined using Nuclear Magnetic Resonance (NMR) analysis. Product: $^{1}$HNMR ($CD_3COCD_3$): δ 1.39 (t, 3H, CC*H*$_3$), 3.83 (s,3H, NC*H*$_3$), 4.25 (q, 2H, NC*H*$_2$), 7.75 (d, 2H, NC(*H*)C(*H*)N), 9.06 (s, 1H, NC(*H*)N). $^{13}$CNMR ($D_2O$): 16.2 (*C*$H_3$), 36.9 (N*C*$H_3$), 45.6 (N*C*$H_2$), 123.3, 124.8 (N*CC*N), 138.5 (N*C*N). NMR values are compared with those in the literature.[18]

## 3.3.2: Ionothermal Synthesis of Cobalt Aluminophosphate-34 (CoAPO-34)

A beaker was charged with $H_3PO_4$ (0.395 g, 0.004 mol, Sigma Aldrich, 99%), HF (0.175 g, 0.009 mol, Alfa Aesar, 48% ), EMIMBr (26.4 g, 0.138 mol), $Al[OCH(CH_3)_2]_3$ (0.547g, 0.0027 mol, Alfa Aesar, 98%) and $Co(NO_3)_2.6H_2O$ (0.3498 g, 0.0012 mol, LSR, 96%). The reaction was stirred and heated to 110 $^{o}$ C for 1 hour. Subsequently, 1, 6 hexadiamine (HDA) (0.2 g, 0.0017 mol, Sigma Aldrich, 98%) added into the solution and stirred for 5 minutes. Then the final mixture was transferred into Teflon-lined autoclaves and heated in the oven at 210 $^{o}$ C for 2 hours. The blue product was centrifuged, washed thoroughly with distilled water and methanol. Afterward, dry the product for overnight at 110 $^{o}$ C.

## 3.3.3: Characterization

The Powder X-ray diffraction (PXRD) pattern of materials was collected using a STOE STADIP diffractometer operated with monochromated CuKα X-ray (λ = 1.5406 Å) radiation. A JEOL JSM 5600 SEM, integrated with an EDX system was used to image morphology and for elemental analysis. Elemental analysis was also carried out using CHN analyser. Thermal analysis was completed using Thermogravimetric Analyser (TGA) Netzsch STA 449C under air condition. Analysis of $^{13}C$ solid-state CP MAS NMR spectra of sample were acquired at a magnetic field strength of 14.1 T. Samples were packed into 2.5 or 4 mm rotors and rotated at MAS rates of 12.5 kHz. Spectra were acquired using cross polarization (CP) from $^{1}H$ using optimised contact pulse of 1 ms ramped from 90-100% for $^{1}H$, and two-pulse phase modulation (TPPM) $^{1}H$ decoupling during acquisition with an rf field strength of ~100 kHz. Signal averaging was carried out for 12824 transients with recycle intervals of 0.5 s. For analysis of $^{27}Al$ solid-

state MAS NMR spectra were acquired at a magnetic field strength of 14.1 T. Samples were packed into 2.5 mm rotors and rotated at MAS rates 20-25 kHz. Signal averaging was carried out for 1024 transients and the spectra were acquired using recycle intervals of 1 with typical rf field strengths of ~100 kHz. Analysis of $^{31}P$ solid-state MAS NMR spectra were acquired at a magnetic field strength of 14.1 T. Samples were packed into 2.5 mm rotors and rotated at MAS rates of 25 kHz. Signal averaging was carried out for 16 transients and the spectra were acquired using recycle intervals of 1 s with typical rf field strengths of 100-110 kHz. In this study, all the MAS NMR analyses were performed using a 400MHz HFXY Bruker Avance III spectrometer. Determination of cobalt isomorphic substitution in the compound has been confirmed by $^{31}P$ NMR using static-spin echo mapping technique. The experiment has been conducted using Bruker Avance III spectrometer equipped with a 9.4 T wide-bore superconducting magnet, operating at Larmor frequency of 161.976 MHz for $^{31}P$. The radio frequency power was ~180 kHz (90 degree pulse of 1.4 ms) and the echo delay was 10 ms. Signal averaging was carried out for 10240 transients for each frequency step with a repeat interval of 0.1 s. Frequency stepping was carried out as needed and spectra for each frequency step were processed and then codded to give the final spectrum.

## 3.4: Result and Discussion

### 3.4.1: Powder X-ray Diffraction (PXRD) of as-synthesised CoAPO-34

The CoAPO-34 structure was confirmed by Powder X-ray Diffraction (PXRD). Figure 3.8 illustrates the good match of the powder pattern of as-synthesized CoAPO-34 to the theoretical

pattern of triclinic CHA-an indicating that the material is isostructural with AlPO-34 (Figure 3.8, the inset).

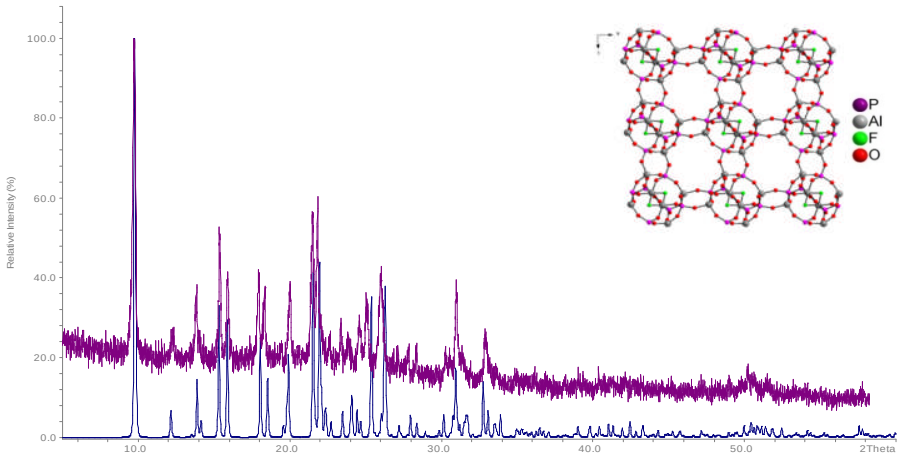


Figure 3.8: PXRD pattern of the as-synthesised CoAPO-34 with triclinic CHA structure. The inset illustrates the CHA structure of AlPO-34

As shown in Figure 3.9 the powder pattern of CoAPO-34 was fitted by the 'Le Bail'[19] method using the General Structure Analysis System (GSAS)[20] suite of programs. The refinement was carried out in space group P-1 and gave reasonable lattice parameter for triclinic CHA topology of CoAPO-34: a = 9.1248 (5) Å, b = 9.2880 (3) Å, c = 9.3217 (4) Å, α = 77.374 $^{o}$(4), β = 87.725 $^{o}$ (3), γ = 89.254 $^{o}$ (4) with agreement factor of *w**R**p* = 0.0987 and ***R**p* = 0.0774. This is within agreement of the verified unit cell for the triclinic CHA topology:[13] a = 9.0897 Å, b = 9.2075 Å, c = 9.2914 Å, α = 76.546 $^{o}$, β = 87.299 $^{o}$, γ = 89.411 $^{o}$. The lattice parameter of CoAPO-34 shows that the unit cell is slightly larger compare to CHA, suggesting that the $Co^{2+}$ ions incorporate in the framework.

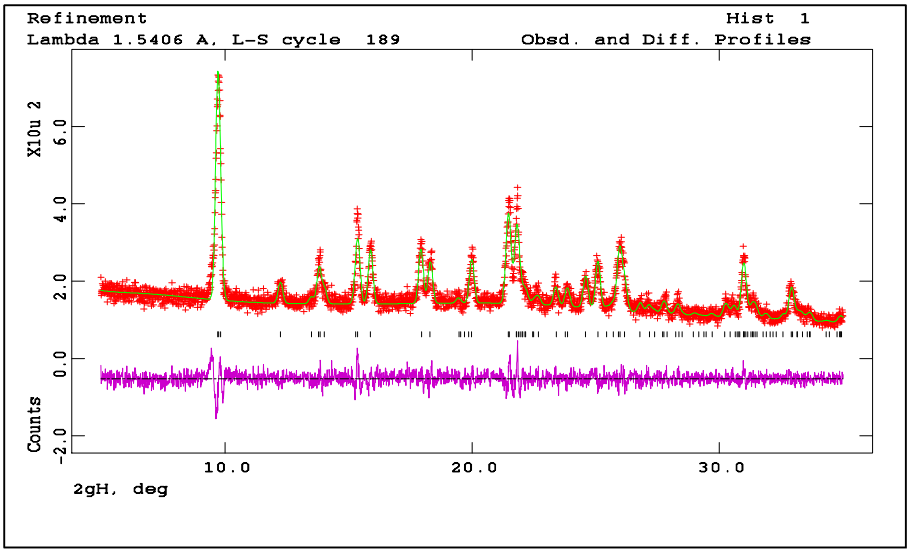


Figure 3.9: Structureless PXRD (and other figures of that type) 'Le Bail' refinement of as-synthesised CoAPO-34 (red crosess indicate experimental data, the green line is the calculated data and the purple line is the difference profile between them)

## 3.4.2: $^{13}$C CP/MAS NMR of CoAPO-34

The general formula of as-synthesised CoAPO-34 can be defined as $[Co_xAl_{n-x}PO_4]_6F_2.R_2$ where n+x ≈ 1 and R is the template. In this study, the EDX result of cobalt composition (in mol) of CoAPO-34 was obtained approximately 0.05 %. Therefore, the empirical formula of this material can be assumed as $[Co_{0.05}Al_{0.95}PO_4]_6$ $F_2.R_2$. This formula helps to determine the template presence in the material (Table 3.1).

The $EMIM^+$ and HDA templates present in CoAPO-34 were determined using $^{13}$C CP/MASS NMR. The solution $^{13}$C NMR spectra of EMIMBr and HDA shown in Figure 3.10 are used as reference to help this analysis. $^{13}$C CP/MASS NMR is shown in Figure 3.11 shows that the $EMIM^+$ resonances are clearly visible but the HDA signals around 26.5 to 28 ppm corresponded to $C_b$ and $C_c$ cannot be observed, indicating that only $EMIM^+$ from the ionic liquid is occluded in

the CoAPO-34 channel. This is in agreement with the CHN analysis (shown in Table 3.1) where the experimental carbon, hydrogen and nitrogen percentages of 16.2 %, 2.0 % and 6.2 %, respectively are very close to the theoretical values obtained for $[Co_{0.05}Al_{0.95}PO4]_6F_2.[C_6H_{11}N_2]_2$. N. Rajic *et.al* in 1997, also reported that two templates of piperidine present in the CoAPO-34 cage, where this material had been prepared under hydrothermal condition.[12] Although HDA was not present as template but it plays important role as co-SDA in the reaction in order to form CoAPO-34. This is because when the HDA was absent in the synthesis, the white crystals of AlPO-11 are preferentially formed instead of the blue crystals of CoAPO. There are two possible explanations as to why this is happening; probably $Co^{2+}$ is too soluble in the ionic liquid and stays in the solution or it is not soluble enough in the solution so it is never in the correct form to be incorporated into AlPO framework. Therefore, when the HDA was added into the solution, it seems 'optimises' or 'fixes' the solubility of $Co^{2+}$ in solution then allows the cation to be incorporated into the CoAPO-34 framework. The colour changes also can be observed from this synthesis, where once HDA was added into the solution the dark blue colour appeared. To confirm the $Co^{2+}$ incorporation within the CoAPO-34 skeleton framework, the spin echo mapping technique in solid state NMR has been used. This will discussed further in Section 3.4.11.

Table 3.1: Elemental Analysis: Carbon, Hydrogen and Nitrogen Percentage of CoAPO-34

| Molecular formula of CoAPO-34 | Template expected | Calculation % | | | Experiment % | | |
|---|---|---|---|---|---|---|---|
| | | C | H | N | C | H | N |
| $[Co_{0.05}Al_{0.95}PO_4]_6F2.[C_6H_{11}N_2]..[C_6H_{16}N_2]$ | 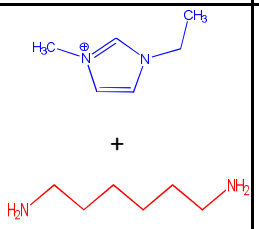 | 14.3 | 2.7 | 5.5 | 16.2 | 2.0 | 6.2 |
| $[Co_{0.05}Al_{0.95}PO_4]_6F_2.[C_6H_{11}N_2]_2$ | 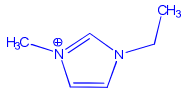 | 15.0 | 2.3 | 5.8 | | | |

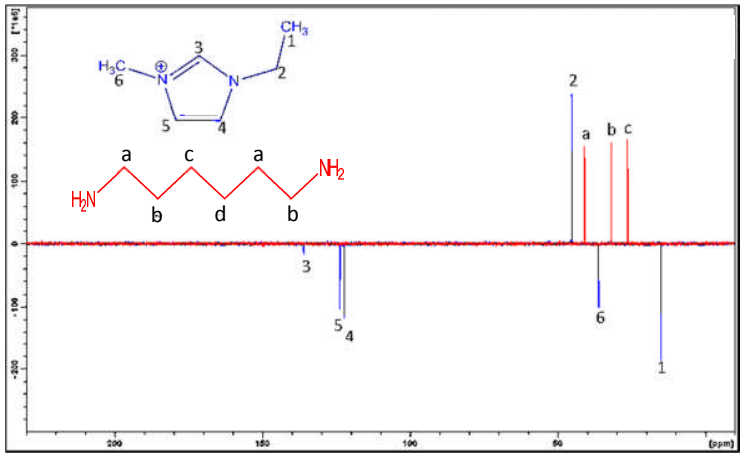


Figure 3.10: Solution $^{13}C$ DEPTQ CP/NMR spectrum of EMIMBr (blue) and HDA (red)

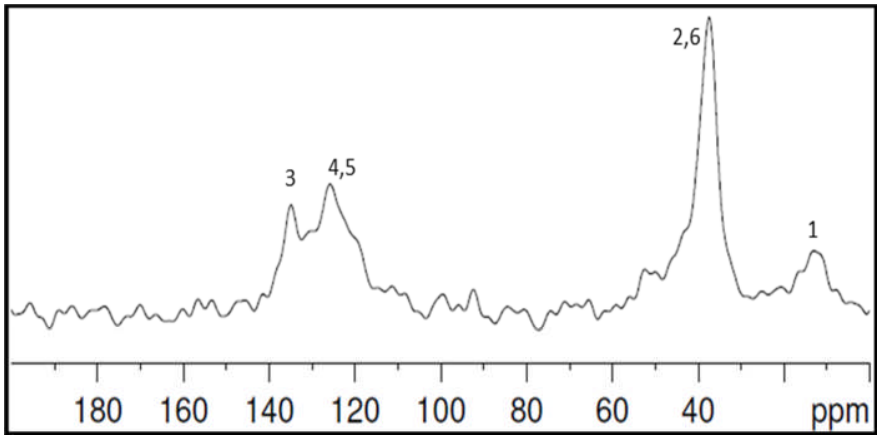


Figure 3.11: $^{13}C$ CP/MAS NMR spectrum of as-synthesized CoAPO-34

## 3.4.3: Other elements included in experiment

In this study, the same experimental method has been attempted with other metal nitrates and silicon ($SiO_2$) (shown in Table 3.2) in place of the $Co^{2+}$ to target MAPO and SAPO materials. Unfortunately this method was not successful for them. When the syntheses were using $Mg^{2+}$, $Zn^{2+}$ and $Fe^{2+}$, the white crystals of AlPO-34 were formed whilst for $Ni^{2+}$ and $Cu^{2+}$ an amorphous product was acquired. On the other hand, for $Si^{4+}$, the product obtained is AlPO material with cloverite (CLO) topology. This probably occurs because the HDA is not good enough at solublising the metals/silicon in the solution in order to incorporate the cations into the AlPO framework. Although silicon is present in a significant amount of 0.02 mol %, it is present as unreacted silica. The presence of unreacted silica is confirmed by $^{29}Si$ MAS NMR (shown in Figure 3.12), which only shows a single peak at -110 ppm.[14] If the silicon had been incorporated into the framework, other peaks corresponding to $Si(OAl)_n$ environments would be present at -90 ppm (n=4), -94.5 ppm (n=3), -98.8 ppm (n=2) and -104.9 ppm (n=1).[21-23] It is clear

that AlPOs and CoAPO-34 are more accessible under this ionothermal condition while it is much trickier for other metals or silicon soluble in this solution in order to form MAPOs or SAPOs.

Table 3.2: Composition of products obtained from metals inclusion experiments

| **Metal Ion** | **Compound Obtained** | **Powder colour** | **Mol composition (%) of metal from EDX** |
|---|---|---|---|
| $Mg^{2+}$ | AlPO-34 | White | 0.007 |
| $Fe^{2+}$ | AlPO-34 | White | 0.001 |
| $Zn^{2+}$ | AlPO-34 | White | 0.002 |
| $Ni^{2+}$ | amorphous | white | - |
| $Cu^{2+}$ | amorphous | white | - |
| $Si^{4+}$ | AlPO-CLO (DNL-1) | White | 0.020 |

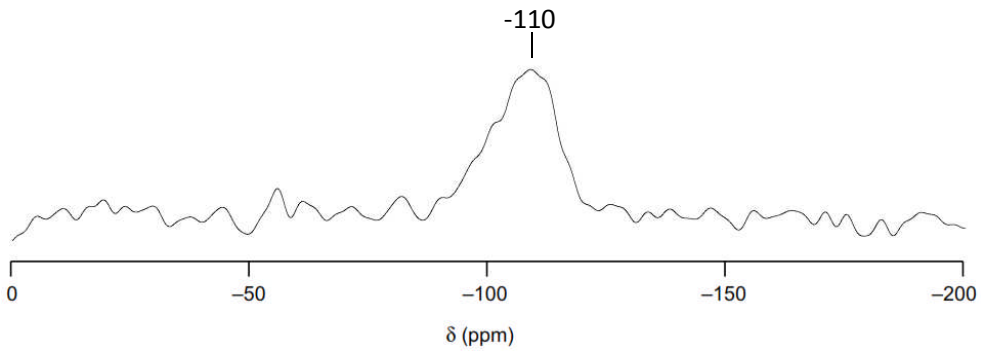


Figure 3.12: $^{29}$ Si MAS NMR spectra of Si containing AlPO-CLO

## 3.4.4: AlPO-11

As mentioned, the absence of HDA in the reaction leads to the formation of white crystals of AlPO-11. The EDX elemental analysis result of AlPO-11 shows that the cobalt percentage obtained is less than 0.001%, indicating that the cobalt not present in the AlPO-11 material. The PXRD pattern shown in Figure 3.13 confirms that the crystal structure of AlPO-11 is analogous to the theoretical AEL topology of AlPO-11.

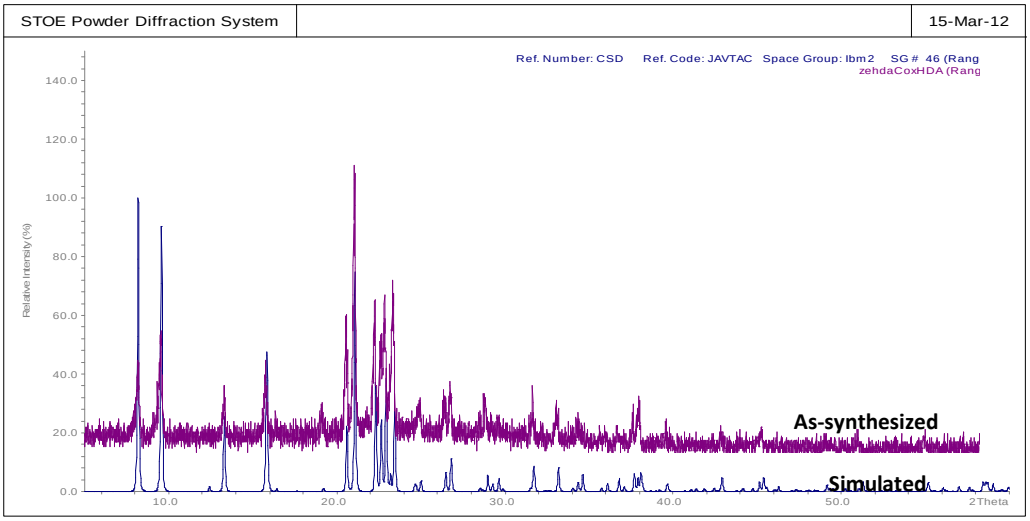


Figure 3.13: PXRD pattern of as-synthesized AlPO-11

The 'Le Bail' method within the GSAS program has been used to fit the powder pattern of the as-synthesised AlPO-11 material to the theoretical pattern for the AEL topology of AlPO-11 as shown in Figure 3.14. The index refinement using space group *Ibm2* gives orthorhombic unit cell parameters to AlPO-11: a = 13.3232 (7) Å, b = 18.5612 (10) Å, c = 8.4279 (4) Å, α = 90°, β = 90°, γ = 90°. The residual factors of refinement are *wRp* = 0.0557 and ***Rp*** = 0.0416. These lattice parameters are in accordance with the verified unit cell for the SIZ-3 (AlPO-11) topology a = 13.292 Å, b = 18.469 Å, c = 8.421 Å, α = 90°, β = 90°, γ = 90°.[13]

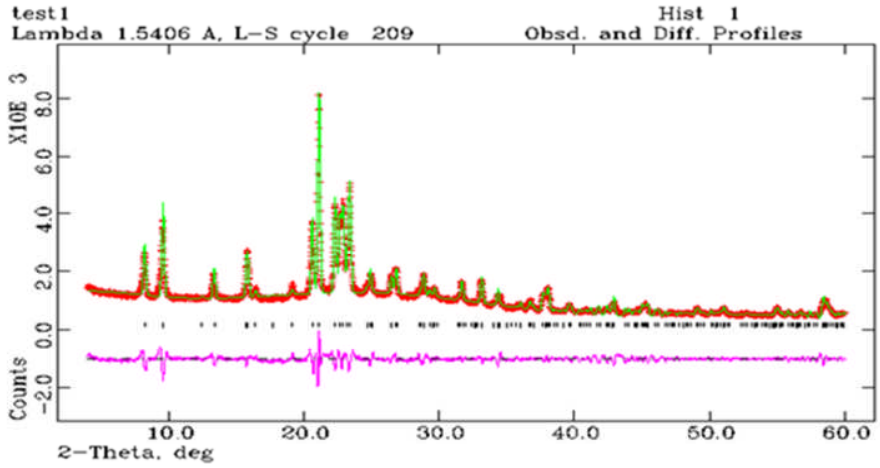


Figure 3.14: Structureless PXRD (and other figures of that type) 'Le Bail' refinement of AlPO-11 (red crosses indicate experimental data, the green line is the calculated data and the pink line is the difference profile between them)

Figure 3.15 shows the AlPO-11 framework can be described one-dimensional 10-membered ring pores with an elliptical pore opening of around 6.3 Å × 3.9 Å.[24] Each pore is isolated from the adjacent pore by a wall composed of linked 4 and 6-rings of alternating aluminium and phosphorus tetrahedra. The fluoride observed in an $AlO_4F$ unit, which form an Al-F-Al linkage.[25]

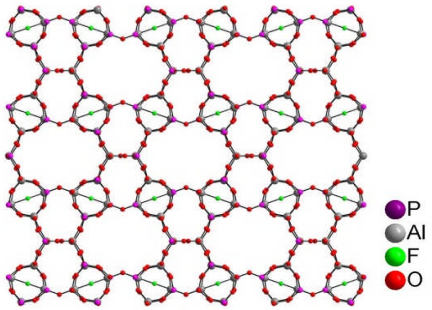


Figure 3.15: The AEL structure of AlPO-11

## 3.4.5: Thermogravimetric Analysis (TGA) CoAPO-34

The thermal stability of as-synthesised CoAPO-34 was analysed using Thermogravimetric Analysis (TGA). Under this analysis the sample was heated to 650 $^{o}$C. The TGA curve (Figure 3.16) shows an initial mass loss of about 4.42% between 25 $^{o}$C and 320$^{o}$C, which can be attributed to the physically adsorbed water.[26] The remaining weight loss between 320 $^{o}$C and 550 $^{o}$C of 20.73 % is corresponding to the loss of one equivalent of 1-ethyl-3-methylimidazolium cation and fluoride ion per $[Co_{0.05}Al_{0.95}PO_4]_6$ formula unit (cal. 23 %).[13, 26]

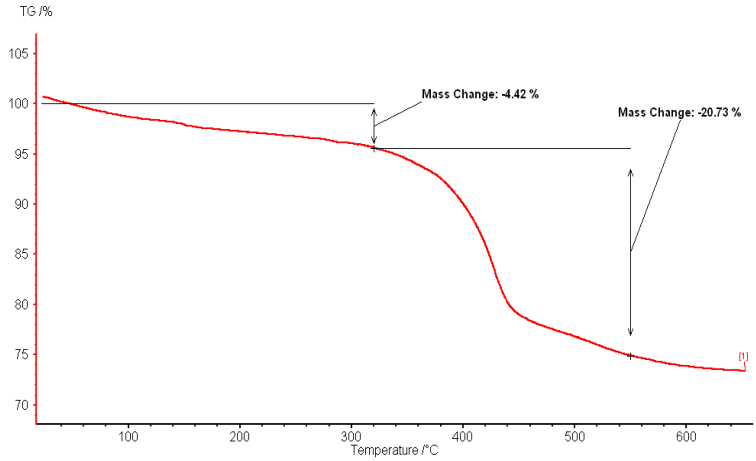


Figure 3.16: The TG curve of as-synthesised of CoAPO-34

## 3.4.6: Calcined CoAPO-34

The triclinic CoAPO-34 was calcined at 550 $^{o}$C, removing the templates to give various forms of chabazite depending on the degree of hydration that occurs when the cooled sample in exposed to the air. Extra peaks are detected in the powder pattern (Figure 3.17 (a)), indicating that two different hydrated phases with triclinic symmetry were formed in the sample.[15] According to the observation, the blue color of calcined CoAPO-34 has turned to the greenish color when

exposed to the air which denoted that Co(II) has been oxidised to Co(III).[12] This sample was treated at 200 $^{o}$C under overnight vacuum after which it adopts the rhombohedral structure. The powder pattern of this dehydrated sample shown Figure 3.17(b) is perfectly matched with the theoretical pattern of rhombohedral symmetry of CHA topology (Figure 3.17 (simulated), in the inset). This agreed by fitting the powder pattern using the 'Le Bail' method within the GSAS program as shown in Figure 3.18. The index refinement of dehydrated CoAPO-34 was performed in space group *R-3* that gave the rhombohedral unit cell parameter: a = 13.7081 (4) Å, c = 14.8717(6) Å, α = 90$^{o}$ and, γ = 120$^{o}$. The residual factors of refinement were *wRp* = 0.0956 and *Rp* = 0.0730. These lattice parameters are closely to the rhombohedral unit cell parameter of the CHA topology: a = 13.6750 Å, b = 13.6750 Å, c = 14.7670 Å, α = 90 and, γ = 120$^{o}$.[5]

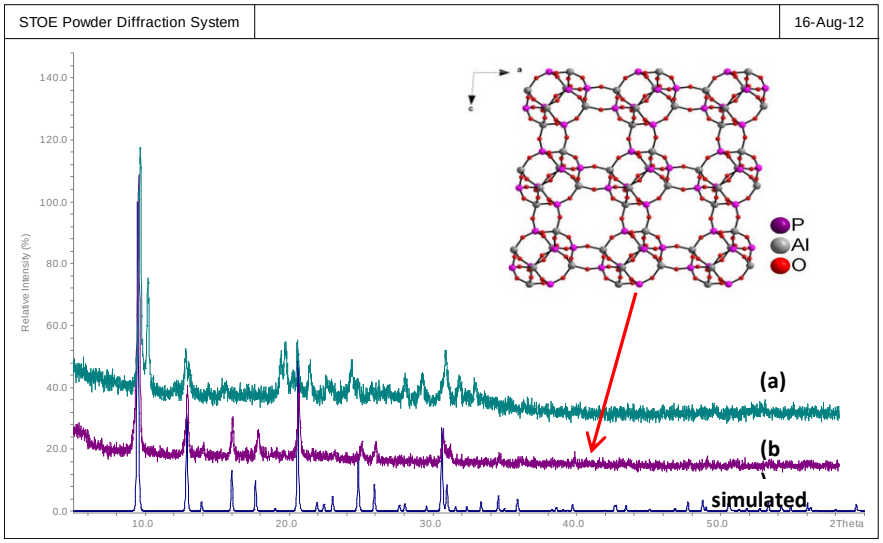


Figure 3.17: PXRD pattern of (a) rehydrated CoAPO-34 and (b) dehydrated CoAPO-34 with rhombohedral CHA structure. Inset shows the rhombohedral CHA structure of AlPO-34

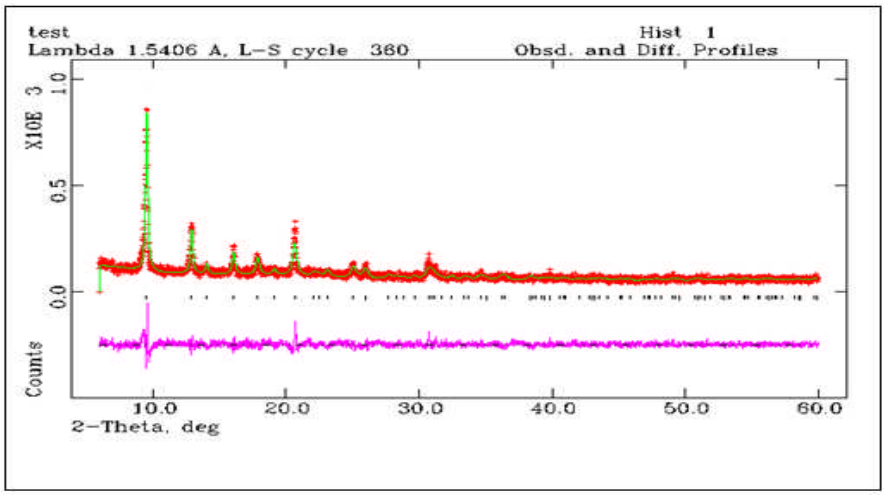


Figure 3.18: Structureless PXRD (and other figures of that type) 'Le Bail' refinement of dehydrated CoAPO-34(red crosses indicate experimental data, the green line is the calculated data and the pink line is the difference profile between them)

## 3.4.7: Effect of HF

The formation and crystallinity of CoAPO-34 has been investigated by using different amounts of hydrofluoric acid (HF) in the synthetic experiments. Figure 3.19 shows the PXRD patterns of CoAPO-34 materials prepared using with different amounts of HF. Clearly, from this figure the crystallinity of CoAPO-34 increases with the increasing amount of added HF. The CoAPO-34 started to form when the synthesis consumed 0.0005 mol of HF eventually the highest crystallinity and purity of the material was achieved when HF increased to 0.0035 mol. When the synthesis was carried out without HF, an amorphous material was preferentially obtained. This indicates that HF is a very important additive in the formation of CoAPO-34 to solubilize the starting material and leads to slow nucleation process. Additionally, the fluoride ions also impart a structure-directing and templating effect which has found as bridges of Al atoms of 4

membered rings in CHA-like aluminophosphate[12] (Shown in Figure 3.7). In this study, the synthesis reaction also was carried out without both HF and HDA. The product was obtained from this synthesis is amorphous. This indicates that the presence of both HF and HDA are important additives to crystallise CoAPO-34.

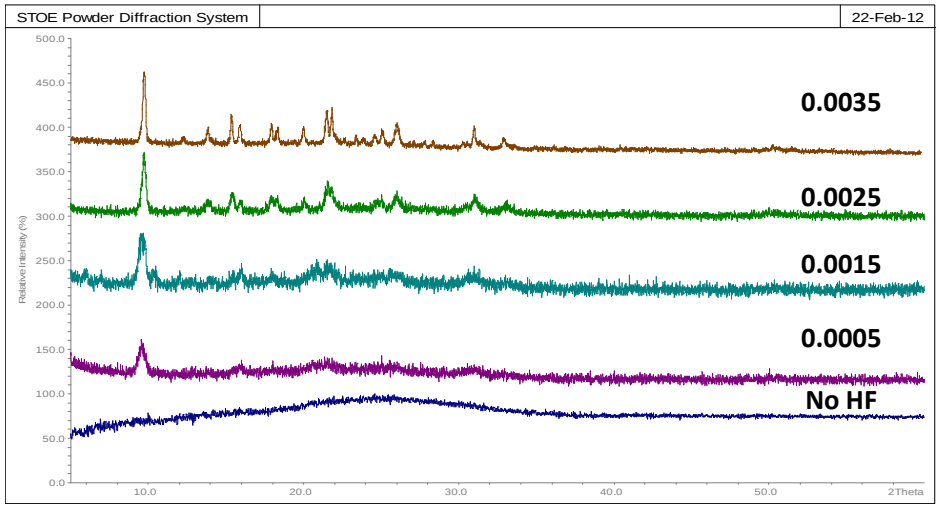


Figure 3.19: PXRD pattern of CoAPO-34 at different molar quantities of HF

## 3.4.8: Effect of amount EMIMBr in synthesis

Initially, the preparation of CoAPO-34 was carried out using 26.4 g of EMIMBr. Since this amount is relative large and the cost of EMIMBr is about £1.50 per g,[27] the quantity of EMIMBr has been reduced, primarily for economic reasons. Figure 3.20 shows the diffraction patterns of CoAPO-34 made with different amounts of EMIMBr. By comparing these powder patterns it may be seen that there have been no significant changes to the sample structure, however, the synthesis using 26.4 g of EMIMBr, results in better crystallinity of the CoAPO-34. This figure

also shows that even when 20% (5 g) of the original amount of EMIMBr was used in the reaction, the pure CoAPO-34 still successfully formed despite the crystallinity of sample being reduced. This indicates that lower reaction mixture concentrations correlate to more crystalline solid products. When comparing the reaction in 5g of ionic liquid instead of 26.4 g ionic liquid, the cost per reaction may be reduced by approximately 80% with only a small loss of crystallinity in the final product. Moreover, the yields of these two reactions are also quite similar with typical yields of approximately ~ 0.2 g (e.g., 0.5 g of EMIMBr ≈ 0.18 – 0.23 g of yield and 26.4g of EMIMBr ≈ 0.20 – 0.24 g of yield). Of course most applications will require the best crystalline sample to achieve good results but in some cases it may be not necessary, as all these depend on the kind and the purpose of application.

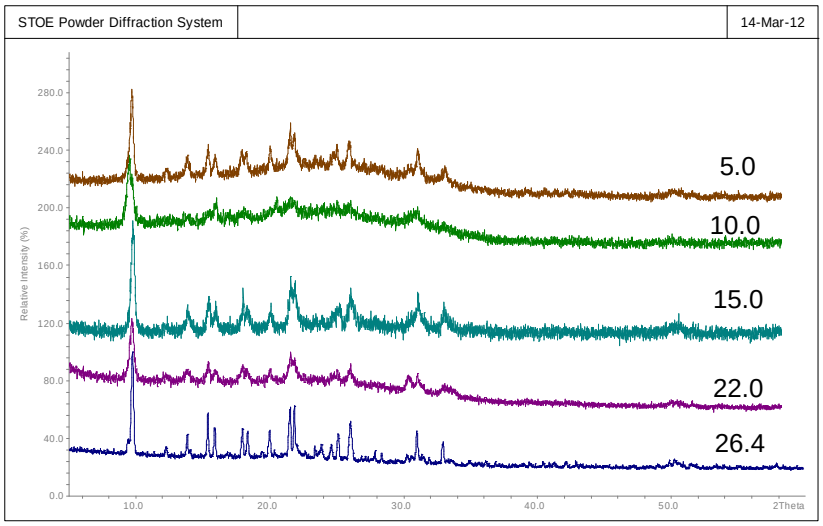


Figure 3.20: PXRD pattern of CoAPO-34 at different amount of EMIMBr in gram (g)

## 3.4.9: $^{27}$Al MAS NMR CoAPO-34

The $^{27}$Al magic angle spinning (MAS) NMR spectrum of the as-synthesized CoAPO-34 is shown in Figure 3.21 (a). The chemical shift of $^{27}$Al peaks at 41.5 and -7.5 ppm are assigned to tetrahedral $Al(OP)_4$ and octahedral aluminium, respectively.[12] Octahedral coordination is due to $^{27}$Al bonded with four oxygens and directly attached with two fluorines in the framework.[14] However, after calcination (Figure 3.21(b)) the octahedral resonance disappeared and only one tetrahedral resonance existed near to 40 ppm which surely corresponds to the alternating of $AlO_4^-$ and $PO_4^+$ in the framework.[12] This indicates that the bond between aluminium and two fluorines has broken when heated up to 450 $^oC$.[13] The elemental analysis from EDX gave agreement in that no fluorine signal appeared in Figure 3.23(b).

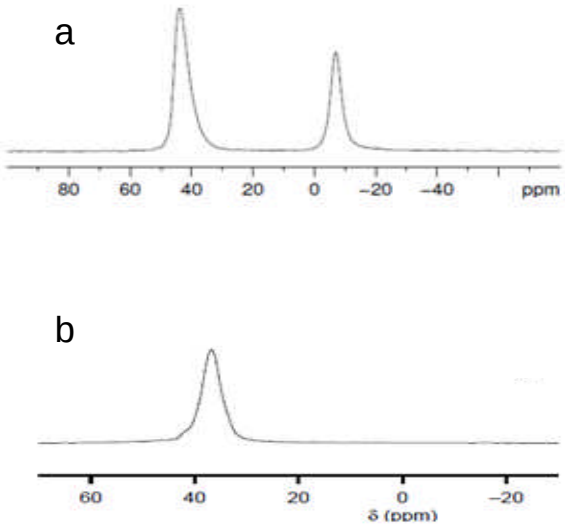


Figure 3.21: $^{27}$Al MAS NMR of (a) As-synthesized CoAPO-34 and (b) Calcined CoAPO-34

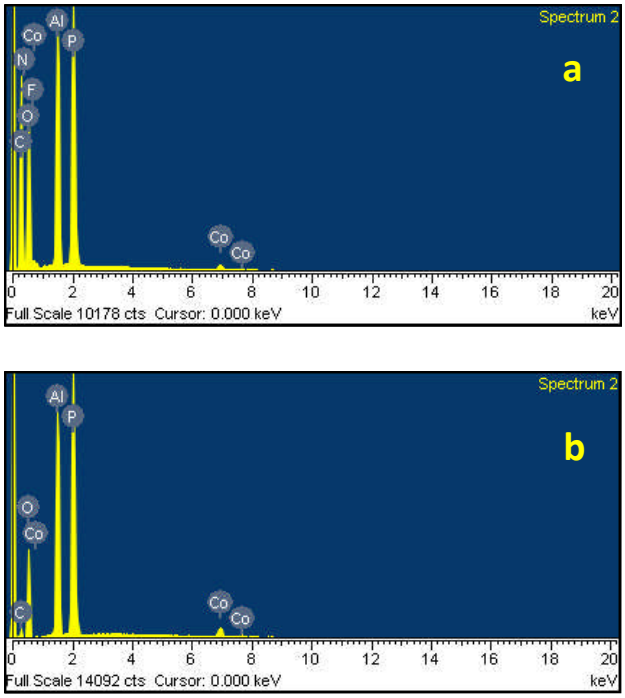


Figure 3.22: EDX spectrum of (a) As-synthesised CoAPO-34 and (b) Calcined CoAPO-34

## 3.4.10: $^{31}$P MAS NMR

Figure 3.23(a) shows the $^{31}$P MAS NMR spectrum of CoAPO-34 contains of the three distinct resonances at -7.5, -23.0 and -29.0 ppm which are due to the different phosphorus sites of P $(OAl)_4$ tetrahedra that are consistent with the triclinic structure of AlPO-34.[12, 13] The very low field resonance at -7.5 ppm is due to the phosphorus nearest the fluoride bridges in the structure.[13, 14] Figure 3.23 (b) shows that the calcined CoAPO-34 spectrum has a single $^{31}$P resonance at -30 ppm. This indicates that only one distinguishable type of tetrahedral phosphorus is present in the sample structure. [28]

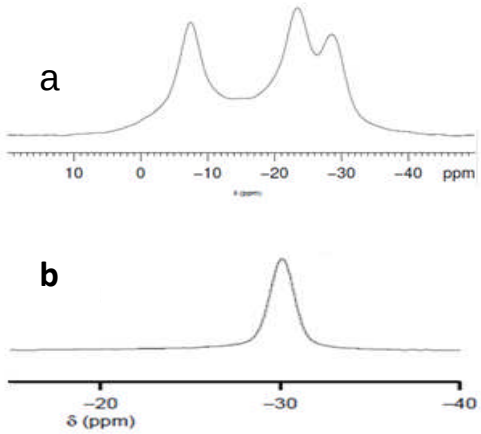


Figure 3.23: $^{31}$P MAS NMR spectrum of (a) As-synthesized CoAPO-34 and (b) Calcined CoAPO-34

## 3.4.11: Broad line $^{31}$P NMR of CoAPO-34

Figure 3.24 a(i) and a(ii) show the $^{31}$P MAS NMR of both as-synthesised and calcined CoAPO-34. Since the interaction of unpaired electrons from paramagnetic $Co^{2+}$ or $Co^{3+}$ with $^{31}$P nuclei increases the rate of relaxation of nuclei, the $^{31}$P signal is drastically broadened and changes the chemical shifts. Thus, the $^{31}$P signal produced is very low and cannot be detectable by conventional $^{31}$P MAS NMR. The presence of intense sidebands in $^{31}$P MAS NMR spectra for both CoAPO-34 samples (shown in Figure 3.25) also sometimes can be considered as a proof for the Co substitution in AlPO framework.[29-31] However, this is ambigious because these sidebands also can be observed for AlPO samples which impregnated with a cobalt salt solution (extra-framework Co).[32-34] Therefore, to overcome these problems, in this study the spin-echo mapping technique has been used to detect the $^{31}$P close to the paramagnetic cobalt centers in CoAPO-34. This technique also was applied for the characterisation of many paramagnetic catalysts such as VPO, CoAPO-5, NiAPO-34, and etc.[34-38] Using this method the hyperfine

interaction between unpaired electrons of paramagnetic Co(II)/Co(III) ions and framework $^{31}P$ nuclei in CoAPO-34 can be detected by the broad line $^{31}P$ NMR spectrum. In this study, the broad lined static spin-echo $^{31}P$ NMR spectra for both as-synthesised and calcined CoAPO-34 are shown in Figure 3.24(b). Figure 3.24(b(i)) shows that the single signal at $\delta \approx 0$ ppm is due to the three in-equivalent phosphorus crystallographic signal of as-synthesised CoAPO-34 (shown in $^{31}P$ MAS NMR spectrum in Figure 3.24 (a(i)), while the single signal at $\delta \approx 0$ ppm for the calcined sample (shown in Figure 3.24(b(ii)) is assigned to one distinguishable type of tetrahedral phosphorus (shown in $^{31}P$ MAS NMR spectrum in Figure 3.24 a(ii)) . This single signal of $P(OAl)_4$ environment possess as slower transverse relaxation than for phosphorus nuclei in the $P(OAl)_{4-n}(OCo)_n$ environment . The broad line $^{31}P$ signal appears between 2000 to 5000 ppm and is due to $P(OAl)_{4-n}(OCo)_n$ environment, attributing to pseudocontact interaction and hyperfine coupling of unpaired electrons from paramagnetic Co(II)/Co(III) with P. Typically the chemical shift of the broadline $^{31}P$ NMR signal depends on the number of Co atoms in the first coordination sphere around the P nucleus, where the signal will shifted towards low fields by following the order of $P(OAl)(OCo)_3 > P(OAl)_2(OCo)_2 > P(OAl)_3(OCo)$. This chemical shift of the broadline is proportional to the number of unpaired electrons of Co atoms on the P nucleus.[34, 37] Figure 3.24(b(i)) clearly shows that the broadline $^{31}P$ NMR signal appears around 2500 ppm is suggested to be due to the $P(OAl)_3(OCo)$ environment, as found in CoAPO-5 by L. Cannesson and A. Tuel in 1997. They reported that this signal is approximately one quarter of 9500 ppm of the $^{31}P$ signal of P atoms that are surrounded exclusively by four Co in DAF-2[34], cobalt phosphate made of alternating $CoO_4$ and $PO_4$ tetrahedra.[39] In this study the empirical formula of CoAPO-34 has been expected as $[Co_{0.05}Al_{0.95}PO_4]F_2$. $R_2$, assuming that each site occupation is independent (i.e. there is no clustering of Co etc), then the probability of any one Al being replaced by Co is 0.05. The probability of having a $P(OAl)_3(OCo)$ unit is therefore $4 \times 0.95^3 \times 0.05 = 0.17$.

The line shape is also slightly modified upon calcination of CoAPOs. Cannesson and Tuel found that the common trends of the line intensity of CoAPOs in the range between 500 to 1500 ppm of CoAPOs increases upon calcination whilst the range above 2500 ppm decreases. This is also observed in the calcined CoAPO-34 spectrum shown in Figure 3.24 b(ii). The observed shift is probably depends on the geometry and electronic density around P atoms, and such modification might be explained by changes in bond angles and lengths or by partial oxidation of Co(II) and Co(III) species upon calcination. Indeed, oxidation is expected to reduce the electron density on the phosphorus nuclei and thus decrease the observed NMR shift as also already reported for VPO[40] and CoAPO-50[34].

In this study, the CoAPO-34 product was in blue and it is well known that the blue color of CoAPOs is typical for the incorporation of tetrahedrally coordinated $Co^{2+}$ into AlPO frameworks,[29, 41, 42] suggesting that the broadline appears in the static spin-echo $^{31}P$ NMR spectrum of the samples are corresponding to the interaction of unpaired electrons of Co(II) with P nuclei. This confirm that the isomorphous substitution of $Al^{3+}$ with $Co^{2+}$ ions in CoAPO-34 framework has successfully achieved with the form of Co-O-P bridges.

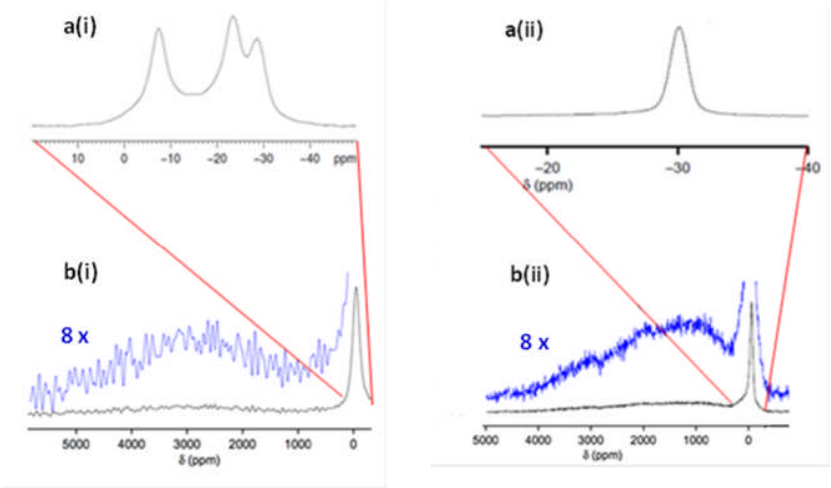


Figure 3.24: $^{31}P$ MAS NMR spectrum of (a(i)) As-synthesized, (a(ii)) Calcined CoAPO-34 , Static $^{31}P$ of spin-echo spectrum of (b(i)) as-synthesised and (b(ii) calcined CoAPO-34. The blue

broad line spectrum was scaled up to 8 magnifications is identical with black spectrum.

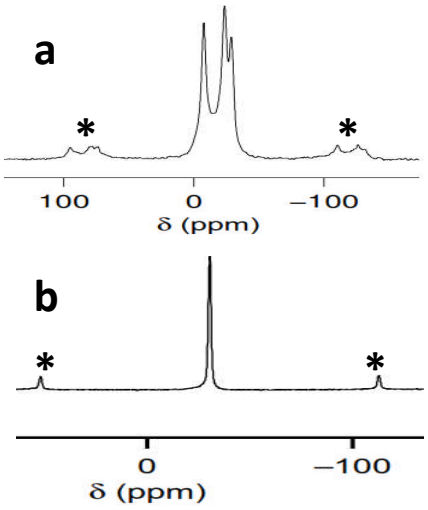


Figure 3.25: Sidebands (*) in $^{31}$P MAS NMR spectrum of (a) As-synthesized CoAPO-34 and (b) Calcined CoAPO-34

## 3.4.12: Morphology of CoAPO-34

SEM characterisation was done for both as-synthesised and calcined CoAPO-34 in order to see the morphology differences of the samples. The images of both samples taken at 600x magnification (see Figure 3.26 a(i) and b(i)) show that these samples possess similar morphology with different crystal shapes and the cubic is the main shape. From these pictures, it is clear that the sample not only retains its crystallinity after calcination (see PXRD pattern in Figure 3.17), but also the morphologies of the particles remain mainly the same. A selected cubic crystal image for both samples taken at 4000 x magnification are shown in Figure 3.26 (a(ii) and b(ii)). These figures also show that small particles present on the top of the cubic crystal.

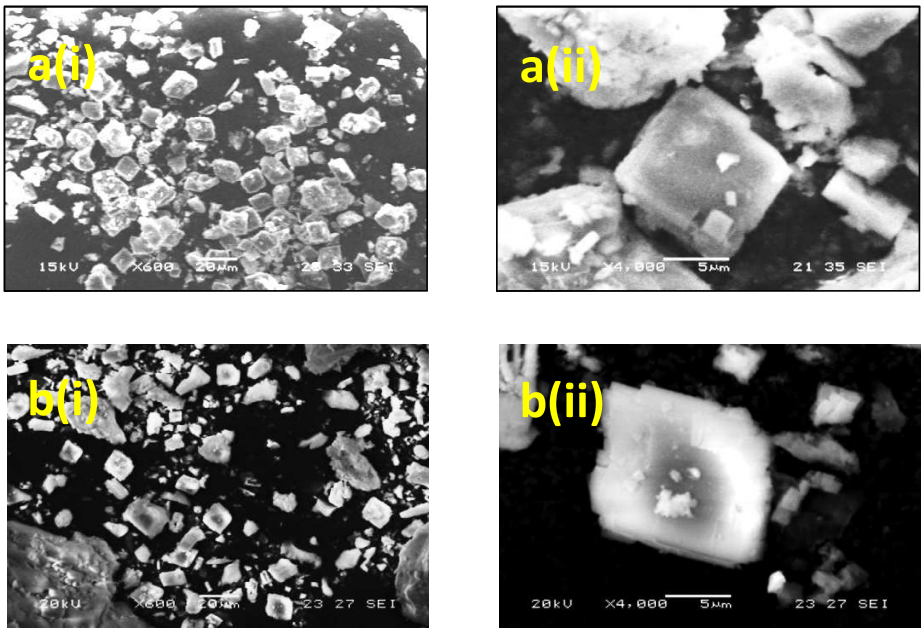


Figure 3.26: Morphology of CoAPO-34; as-synthesised a(i) 600 x, a(ii) 4000 x, cacined b(i) 600 x and b(ii) 4000 x magnification.

## 3.5: Conclusion

As conclusion, in this study, CoAPO-34 with CHA structure has been successfully prepared under ionothermal condition using EMIMBr assisted by HDA. The pure CHA structure of CoAPO-34 was confirmed by the PXRD pattern. This indicates that CoAPO-34 also can be prepared under low pressure instead of higher pressure associated with hydrothermal synthesis, which provides an alternative route for the formation of CoAPO-34. From this study, it also found that reducing amount of EMIMBr, CoAPO-34 can be prepared with no significant differences in PXRD pattern of the resulting materials.

As is typical for AlPO or MAPO with CHA structure properties, CoAPO-34 prepared under this ionothermal synthesis is triclinic as-made but has distorted to rhombohedral CHA structure after the removal of templates under the calcination process. This rhombohedral structure is particular sensitive to air moisture and generates the hydrated phase with triclinic symmetry. However, the structure changes are commonly reversible, and the original material can be rebuilt by evacuation at low temperature.

According to the $^{13}C$ NMR, CHN and TGA analyses, only $EMIM^{+}$ was found occluded in the CoAPO-34 cage while HDA stays in the solution. However, HDA plays an important role to optimise the solubility of $Co^{2+}$ in the reaction solution. Without HDA in the reaction, AlPO-11 was preferentially obtained. According to this, the addition of amine again proves that it can alter the original crystallisation reaction which then enables in formation of different products.

HF also plays important additive in order to form CoAPO-34, in the absence of HF in the synthesis reaction, only amorphous sample was obtained. The use of different amount of HF has a great on CoAPO-34 crystallinity, where the product crystallinity increases with higher amount of added HF.

In this study, the broadline $^{31}P$ NMR spectrum provides direct evidence of the incorporation of Co(II) into the aluminium framework sites in the CoAPO-34. The broadline signal is strongly suggested that the presence of Co-O-P bridges in CoAPO-34 framework probably necessary to delocalize the unpaired electrons of the metal on $^{31}$ P nuclei.

According to the SEM image, there has no significant difference between morphology of as-synthesised and calcined CoAPO-34. Both samples possess mixed crystal shapes and the main shape is cubic.

In this study, similar reaction were also carried out using several metals such as $Mg^{2+}$, $Ni^{2+}$, $Fe^{2+}$ and $Cu^{2+}$. However, this method was not successful for those metals to incorporate in AlPO

framework. The products obtained from this experiments are AlPOs and amorphous. This suggests that probably the HDA is not suitable or not good enough at solublising these metals under the same condition as $Co^{2+}$ to form MAPOs. As similar to $Si^{4+}$ also was unsuccessfully incorporated into the AlPO framework to form SAPO, where according to $^{29}Si$ MAS NMR of resulting material suggested that the silica only exist as unreacted silica which is probably stick on the sample surface. It is well known that $Si^{4+}$ shows poor solubility in commonly used ionic liquid; however with suitable modification and condition it is possible to solublise silicon in ionic liquid solution to form SAPOs or silica based materials.[43-45]

Finally, even though the CoAPO-34 is the only catalyst that was successfully prepared from this study, several other interesting materials such as AlPOs (AlPO-34, AlPO-CLO and AlPO-11) were also made ionothermally and they could be used as adsorbent in the gas adsorption and separation.

## 3.6: References


1. J. Yu and R. Xu, *Chemical Society Reviews*, 2006, **35**, 593-604.
2. R. P. Bontchev and S. C. Sevov, *Chemistry of Materials*, 1997, **9**, 3155-3158.
3. D. B. Akolekar and R. F. Howe, *Journal of the Chemical Society, Faraday Transactions*, 1997, **93**, 3263-3268.
4. D. B. Akolekar, *Catalysis Letters*, 1994, **28**, 249-262.
5. Ch. Baerlocher and L. B. McCusker, *Database of Zeolite Structures*: *http://www.iza-structure.org/databases/*.
6. M. Anpo, *Nova*, 2000, 64.
7. J. Chen and J. M. Thomas, *Journal of the Chemical Society, Chemical Communications*, 1994, 603-604.
8. X. Zhao, C. Kang, H. Wang, C. Luo, G. Li and X. Wang, *Journal of Porous Materials*, 2011, **18**, 615-621.
9. E. R. Parnham and R. E. Morris, *Journal of the American Chemical Society*, 2006, **128**, 2204-2205.
10. E. A. Drylie, D. S. Wragg, E. R. Parnham, P. S. Wheatley, A. M. Z. Slawin, J. E. Warren and R. E. Morris, *Angewandte Chemie International Edition*, 2007, **46**, 7839-7843.
11. S. J. Hill, C. D. Williams and C. V. A. Duke, *Zeolites*, 1996, **17**, 291-296.
12. N. Rajić, A. Ristić, A. Tuel and Kaučič, *Zeolites*, 1997, **18**, 115-118.
13. E. R. Cooper, C. D. Andrews, P. S. Wheatley, P. B. Webb, P. Wormald and R. E. Morris, *Nature*, 2004, **430**, 1012-1016.
14. Z. Yan, B. Chen and Y. Huang, *Solid State Nuclear Magnetic Resonance*, 2009, **35**, 49-60.
15. A. Tuel, S. Caldarelli, A. Meden, L. B. McCusker, C. Baerlocher, A. Ristic, N. Rajic, Gregor Mali, and V. Kaucic, *The Journal of Physical Chemistry B*, 2000, **104**, 5697-5705.

16. L. Marchese, E. Gianotti, B. Palella, R. Pirone, G. Martra, S. Coluccia and P. Ciambelli, *Studies in Surface Science and Catalysis*, Elsevier, 2000, **130**, 3005-3010.
17. S. Oh and W. Lee, *Korean Journal of Chemical Engineering*, 1992, **9**, 37-44.
18. E. R. Parnham and R. E. Morris, *Chemistry of Materials*, 2006, **18**, 4882-4887.
19. A. Le Bail, *Journal of Solid State Chemistry*, 1989, **83**, 267-271.
20. B. H. Toby, *Journal of Applied Crystallography*, 2001, **34**, 210-213.
21. S. Ashtekar, S. S. V. Chilukuri and D.K. Chakarbraty, *Journal of physical chemistry*, 1994, **98**, 4878-4883.
22. J. Tan, Z. Liu, X. Bao, X. Liu, X. Han, C. He and R. Zhai, *Microporous and Mesoporous Materials*, 2002, **53**, 97-108.
23. A. M. Prakash and S. Unnikrishnan, *Journal of the Chemical Society, Faraday Transactions*, 1994, **90**, 2291-2296.
24. Y. H. Yeom and S. C. Shim, *Journal of Molecular Catalysis A: Chemical*, 2002, **180**, 133-140.
25. E. R. Parnham, C. D. Andrews, P. S. Wheatley, P. B. Webb, P. Wormald and R. E. Morris, *Studies in Surface Science and Catalysis*, Elsevier, 2005, 158, 247-254.
26. A. Ristić, N. N. Tušar, I. Arčon, F. T. Starzyk, D. Hanžel, J. Czyzniewska and V. Kaučič, *Microporous and Mesoporous Materials*, 2002, **56**, 303-315.
27. S. Aldrich, 2013, 89483-89450G-F.
28. N. N. Tušar, V. Kaučič, S. Geremia and G. Vlaic, *Zeolites*, 1995, **15**, 708-713.
29. B. Chen and Y. Huang, *Microporous and Mesoporous Materials*, 2009, **123**, 71-77.
30. C. Montes, M. E. Davis, B. Murray and M. Narayana, *Journal of physical chemistry*, 1990, **94**, 6425-6430.
31. S. H. Chen, S. P. Sheu and K. J. Chao, *Journal of the Chemical Society, Chemical Communications*, 1992, 1504-1505.

32. M. P. J. Peeters, J.W. de Haan, L. J. M. van de ven and J.H.C. van Hooff, *Colloids and Surfaces A: Physicochemical and Engineering Aspects,*, 1993, **72**, 87-104.

33. B. K. Czarnetzki, W. G. M. Hoogervorst, R. R. Andrea, C. A. Emeis and W. H. J. Stork, *Journal of the Chemical Society, Faraday Transactions*, 1991, **87**, 891-895.

34. L. Canesson and A. Tuel, *Chemical Communications*, 1997, 241-242.

35. M. T. Sananes and A. Tuel, *Journal of the Chemical Society, Chemical Communications*, 1995, 1323-1324.

36. Y. Y. Tong, *Journal of Magnetic Resonance, Series A*, 1996, **119**, 22-28.

37. G. Mali, A. Ristić and V. Kaučić, *The Journal of Physical Chemistry B*, 2005, **109**, 10711-10716.

38. M. T. Sananes and A. Tuel, *Solid State Nuclear Magnetic Resonance*, 1996, **6**, 157-166.

39. J. Chen, S. Natarajan, J. M. Thomas, R. H. Jones and M. B. Hursthouse, *Angewandte Chemie International Edition in English*, 1994, **33**, 639-640.

40. M. T. Sananes, A. Tuel, G. J. Hutchings and J. C. Volta, *Journal of Catalysis*, 1994, **148**, 395-398.

41. S. Thomson, V. Luca and R. Howe, *Physical Chemistry Chemical Physics*, 1999, **1**, 615-619.

42. J. Chen, G. Sankar, J. M. Thomas, R. Xu, G. N. Greaves and D. Waller, *Chemistry of Materials*, 1992, **4**, 1373-1380.

43. X. Zhao, H. Wang, C. Kang, Z. Sun, G. Li and X. Wang, *Microporous and Mesoporous Materials*, 2012, **151**, 501-505.

44. Y.P. Xu, Z. J. Tian, S. J. Wang, Y. Hu, L. Wang, B. C. Wang, Y. C. Ma, L. Hou, J. Y. Yu and L. W. Lin, *Angewandte Chemie*, 2006, **118**, 4069-4074.

45. P. S. Wheatley, P. K. Allan, S. J. Teat, S. E. Ashbrook and R. E. Morris, *Chemical Science*, 2010, **1**, 483-487.

# CHAPTER 4

# IONOTHERMAL SYNTHESIS AND CHARACTERISATION OF FeAPO-34

## 4.1: Introduction

In chapter 1 it has been mentioned that the acidity and redox properties of aluminophosphates (AlPOs) can be altered by inserting metals into the AlPOs framework. The substitution of iron in AlPOs framework can lead to a catalyst for various reactions. There are several examples of iron aluminophosphates (FeAPOs) with microporous structure such as FeAPO-5, FeAPO-11 and FeVPI-5 which are interesting materials because of their activity in oxidation of aromatic compounds. Normally all these materials are prepared under hydrothermal synthesis.[1]

In recent years, ionothermal synthesis has increasingly attracted the interest of chemists working in the field of the synthesis of microporous FeAPOs. As mentioned, ionothermal synthesis can take place at ambient pressure where the IL have extremely low vapor pressure, wide liquid range, strong solvent power for organic or inorganic compounds and high thermal stability during the reaction.[2]

Owing to these peculiar properties of IL, Zhao *et.al* in 2011 and 2012 were inspired to synthesis FeAPO-16 and FeAPO-5, respectively, under ionothermal condition using microwave irradiation.[3, 4] Han *et.al* in 2008 reported that the iron-substituted aluminophosphate with sodalite (SOD) topology was successfully prepared using 1-ethyl-3-methylimidazoliumbromide (EMIMBr) IL in a sealed autoclave.[2]

In this study, the ionothermal synthesis of FeAPO-34 has been explored using 1-ethyl-3-methylimidazoliumchloride (EMIMCl) (Figure 4.1) in the presence of ethylenediamine (EDA)

(Figure 4.2). Owing to the special properties of IL, in this study, ionothermal synthesis was attempted to provide an alternative route to prepare FeAPO-34 under low pressure instead of higher pressure which associated with hydrothermal synthesis. Additionally there are very few studies reported about the synthesis of this material. Traditionally, FeAPO-34 was synthesized under hydrothermal condition using fluoride medium and piperidine as a structure-directing agent (SDA) which was reported by Ristic *et.al* in 2002.[5] FeAPO-34 is interesting material because it is one of the selective catalysts used in the preparation of olefin from methanol.[6, 7] The CHA topology of FeAPO-34 as shown in Figure 4.3 is similar structure to AlPO-34 [8] as described in Chapter 3.

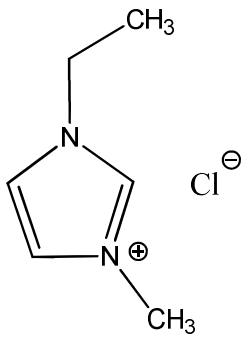


Figure 4.1: 1-ethyl-3-methylimidazoliumchloride (EMIMCl) IL

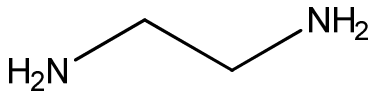


Figure 4.2: Ethylenediamine (EDA)

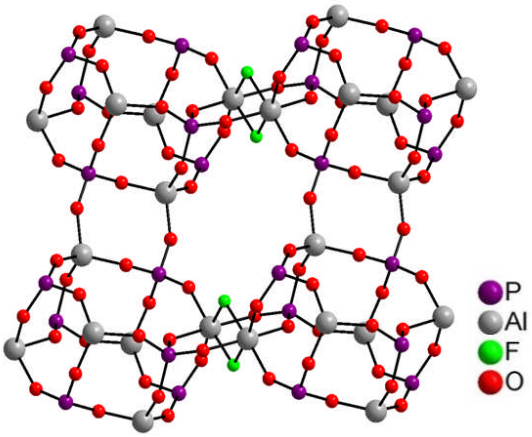


Figure 4.3: The triclinic structure of AlPO-34 [8]

## 4.2: Aims

The aim of this study is to synthesis FeAPO-34 under ionothermal conditions using 1-ethyl-3-methylimidazoliumchloride (EMIMCl) ionic liquid (IL) with addition of ethylenediamine (EDA). In this study, the synthesis also was carried out in the absence of EDA and hydrofluoric acid (HF) to observe any effect obtained on to the structure. The characterization of FeAPO-34 has been carried out using PXRD, TGA, EDX, CHNS, SEM and SSNMR.

## 4.3: Materials and Methodology

## 4.3.1: Ionothermal synthesis of FeAPO-34

A Teflon-lined autoclave (23 ml) was charged with $Al[OCH(CH_3)_2]_3$ (0.1899 g, 0.0009 mol, Alfa Aesar, 98%), $H_3PO_4$ (0.474 g, 0.0048 mol, Sigma Aldrich, 99%), HF (70 µl, 0.0034 mol, Alfa Aesar. 98%), EMIMCl (4g, 0.0272 mol, Sigma Aldrich, 98%), $Fe(C_2H_3O_2)_2$ (0.122 g, 0.0007 mol, Sigma Aldrich, 95%) and ethylenediamine (0.1 g, 0.0016 mol, Sigma Aldrich, 99%). Subsequently the autoclave was heated at 210 $^oC$ for 3 days in the oven. Afterward the autoclave was cooled to room temperature. The brown product was filtered, washed thoroughly with distilled water and methanol. Finally, the product was dried at room temperature.

## 4.3.2: Characterization

The PXRD pattern of the sample was collected by using STOE STADI-P diffractometer operated with monochromated $CuK\alpha_1$ X-ray (λ= 1.5406 Å). The image morphology of sample has been examined using JEOL JSM 5600 SEM. Using the same model of SEM integrated with EDX system the type of elements present in the sample has been determined. Besides that, CHN analysis also has been carried out for the elemental determination. The thermal analysis was investigated by using Thermogravimetric Analyser (TGA) Netzsch STA 449C under air. In solid state NMR analyses, $^{13}C$ solid-state CP MAS NMR spectra were acquired at a magnetic field strength of 14.1 T. Samples were packed into 2.5 or 4 mm rotors and rotated at MAS rates of 12.5 kHz. Spectra were acquired using cross polarization (CP) from $^1H$ using optimised contact pulse durations of 0.25 ms. ), ramped from 90-100% for $^1H$, and two-pulse phase modulation (TPPM) $^1H$ decoupling during acquisition with an rf field strength of ~100 kHz. The

signal averaging was carried out for 5120 transients with recycle intervals of 3 s. For the $^{27}Al$ solid-state MAS NMR spectra were acquired at a magnetic field strength of 14.1 T. The samples were packed into 4 mm rotors and rotated at MAS rates of 12.5-14 kHz. Signal averaging was carried out for 128 transients and the spectra were acquired using recycle intervals of 5 with typical rf field strengths of ~100 kHz. $^{31}P$ solid-state MAS NMR spectra were acquired at a magnetic field strength of 14.1 T. Samples were packed into 4 mm rotors and rotated at MAS rates of 12.5-14 kHz. Signal averaging was carried out for 1024 transients and the spectra were acquired using recycle intervals of 10 with typical rf field strengths of 100-110 kHz. All the MAS NMR analyses were performed by using 400MHzHFXY Bruker Avance III spectrometer. Determination of iron isomorphic substitution in the compound has been confirmed by $^{31}P$ NMR using spin echo mapping technique. The experiment was conducted using a Bruker Avance II spectrometer equipped with a 9.4 T wide-bore superconducting magnet, operating at a Larmor frequency of 161.976 MHz for $^{31}P$. The radio frequency power was ~180 kHz (90 degree pulse of 1.4 ms) and the echo delay was 10 ms. Signal averaging was carried out for 10240 transients for each frequency step with a repeat interval of 0.1 s. Frequency stepping was carried out as needed and spectra for each frequency step were processed and then codded to give the final spectrum.

# 4.4: Result and Discussion

## 4.4.1: Powder X-ray Diffraction (PXRD) pattern as-synthesized of FeAPO-34

Figure 4.4 illustrates the X-ray diffraction pattern of as-synthesized triclinic CHA structure of FeAPO-34. As shown in this figure, the experimental PXRD of FeAPO-34 is perfectly matched

with the CHA simulated pattern. This demonstrates that FeAPO-34 is analogous to the triclinic CHA structure of AlPO-34 (Figure 4.4, the inset)

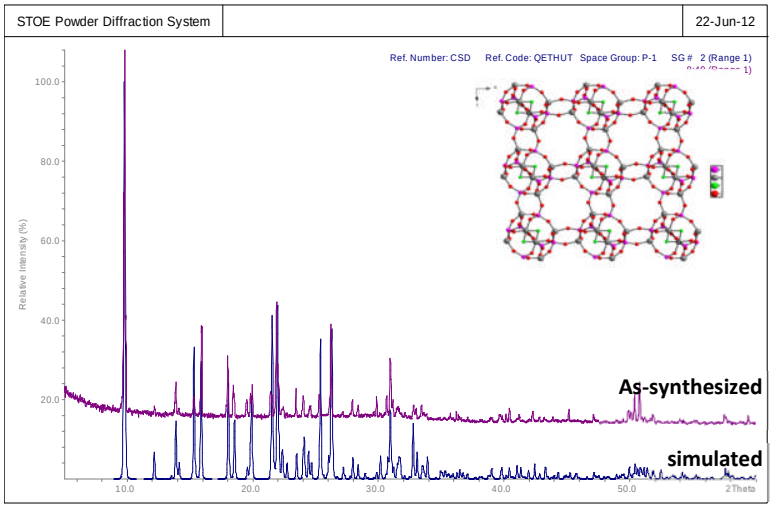


Figure 4.4: PXRD pattern of as-synthesized FeAPO-34 with triclinic CHA structure. Inset illustrates the CHA structure of AlPO-34.

'Le Bail' refinement method using GSAS program has been used to fit the powder pattern of as-synthesised FeAPO-34 as shown in Figure 4.5. The index refinement of this powder pattern was performed in space group P-1 generates triclinic unit cell parameter to FeAPO-34: a = 9.1142 (5) Å, b = 9.2281 (4) Å, c = 9.3089 (5) Å, α = 76.596 (4) $^{o}$, β = 87.136 (5) $^{o}$, γ = 89.337 (4) $^{o}$. The residual refinement acquired of $wRp$ = 0.0714 and $Rp$ = 0.0415. These unit cell parameters are closely to the triclinic unit cell parameter of CHA topology:[8] a = 9.0897 Å, b = 9.2075 Å, c = 9.2914 Å, α = 76.546 $^{o}$, β = 87.299 $^{o}$, γ = 89.411$^{o}$. The unit cell obtained shows that the FeAPO-34 cell is slightly larger than AlPO-34 which probably due to the presence of $Fe^{2+}$ ions in the FeAPO-34 framework.

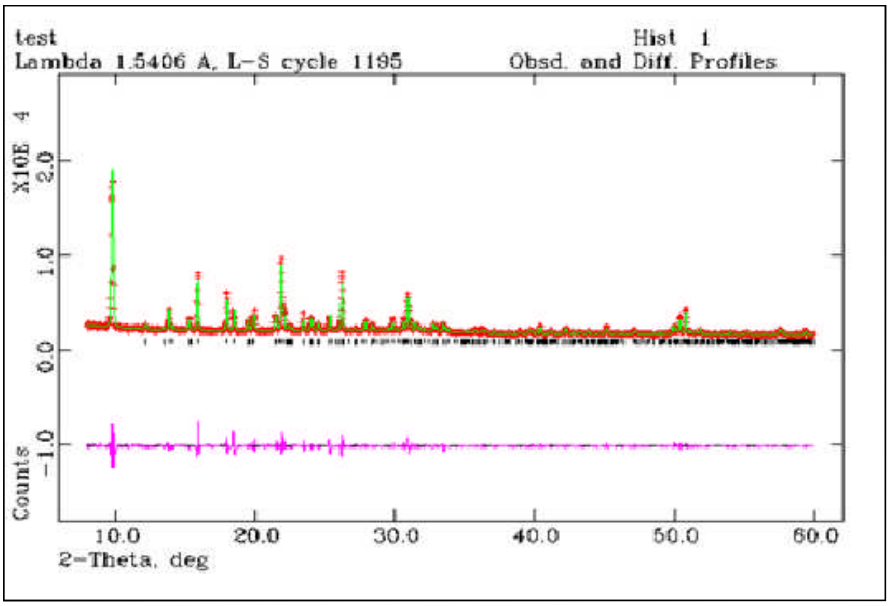


Figure 4.5: Structureless PXRD (and other figures of that type) 'Le Bail' refinement of as-synthesised FeAPO-34 (red crosses indicate experimental data, the green line is the calculated data and the purple line is the difference profile between them)

## 4.4.2: $^{13}$C CP/MAS NMR of FeAPO-34

The general formula of FeAPO-34 is $[Fe_xAl_{n-x}PO_4]_6F_2.R_2$, where n+x ≈ 1 and R is the template. In this study, the mol composition of iron in FeAPO-34 which obtained from EDX is approximately 0.08 %. Therefore, the empirical formula of FeAPO-34 can be considered as $[Fe_{0.08}Al_{0.92}PO_4]_6\ F_2.R_2$. This formula facilitates to determine the presence of templates in FeAPO-34 (Table 4.1).

$^{13}$C CP/MASS NMR measurement was carried out to determine the presence of templates in FeAPO-34. Figure 4.6 shows that $^{13}$C CP/MASS NMR spectrum of FeAPO-34 consists of three signals which correspondence to 1, 3-dimethylimidazolium cation ($DMIM^+$).[9] This spectrum

shows that the signal at 37.2 ppm is attributed to methyl ($CH_3$) groups of $C_1$ and $C_2$, while the resonance visible at 125.7 ppm is assigned to carbon atoms for both $C_3$ and $C_4$. The remaining signal at lowest field of 134.3 ppm is due to $C_5$. This spectrum also shows clearly there is no signal appears around 16.5 ppm which would be attributed to the methyl group from 1-ethyl-3-methylimidazolium cation ($EMIM^+$) (shown in Figure 4.21). This suggests that the template was occluded in the FeAPO-34 cages is $DMIM^+$ instead of the original cation of $EMIM^+$ from EMIMCl. It seems that in the presence of fluoride in the reaction, the methyl bond in $EMIM^+$ was broken and reformed under ionothermal synthesis condition, and that $DMIM^+$ was formed via metathesis of the alkylgroups. This was also seen SIZ 10 CHA when prepared ionothermally, whenin the presence of HF in the reaction, ionic liquids with alkyl chain lengths of 3 to 5 were broken and formed $DMIM^+$.[9] In this study the formation of FeAPO-34 CHA framework seems to be favorable the presence of $DMIM^+$ rather than $EMIM^+$, as compared to formation of CoAPO-34 which has discussed in Chapter 3, which is formed in the presence of $EMIM^+$ even though the fluoride is also present in the synthesis reaction.

In the spectrum shown in Figure 4.6, the $CH_2$ signal of EDA which was expected appears at 43.7 ppm is difficult to observe. So, there are two possibilities arise here; either this signal overlapped with the signal from the methyl group in $DMIM^+$ or it is not present in the FeAPO-34 framework. Therefore, CHN elemental analysis was carried out to clarify this. The CHN results given in Table 4.1 show experimental carbon, hydrogen and nitrogen percentages of 11.36%, 1.56 **%** and 5.62%, respectively. These are very close to theoretical values for $[Fe_{0.08}Al_{0.92}PO_4]_6F_2 .[C_5H_9N_2]_2$, suggesting that only $DMIM^+$ is present as template whilst both of EDA and $EMIM^+$ are absent. As same as HDA which has discussed in Chapter 3, although EDA is not occluded in the FeAPO-34 cages, it plays an important role in the reaction, where it fixes the solubility of $Fe^{2+}$ in the solution reaction and facilitates the $Fe^{2+}$ incorporation into the FeAPO-34 framework. Without EDA in the reaction, the white crystals of AlPO-34 were

preferentially obtained. The AlPO-34 CHA structure was confirmed by PXRD pattern shown in Figure 4.7. The mol composition of iron in AlPO-34 which obtained from EDX is less than 0.002 %, assuming that the iron is not present in the material. In this study, the $Fe^{2+}$ incorporation within the FeAPO-34 skeleton framework is confirmed by broadline $^{31}P$ NMR spin-echo which is discussed further in Section 4.4.8.

Table 4.1: Carbon, Hydrogen and Nitrogen Percentage of FeAPO-34

| Molecular Formula | Template expected | Calculation % | | | Experiment % | | |
|---|---|---|---|---|---|---|---|
| | | C | H | N | C | H | N |
| $[Fe_{0.08}Al_{0.92}PO_4]_6F_2.[C_6H_{11}N_2]_2.[C_2H_{10}N_2]_2$ | 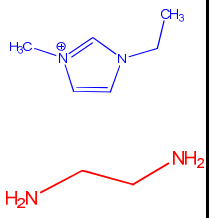 | 17.21 | 4.13 | 10.11 | 11.36 | 1.56 | 5.62 |
| $[Fe_{0.08}Al_{0.92}PO_4]_6F_2.[C_6H_{11}N_2]_2$ | 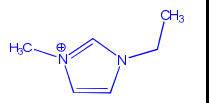 | 14.21 | 2.12 | 5.22 | | | |
| $[Fe_{0.08}Al_{0.92}PO_4]_6F_2.[C_5H_9N_2]\ C_2H_{10}N_2]$ | 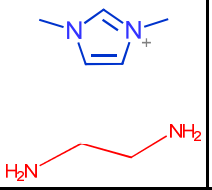 | 8.9 | 2.0 | 5.9 | | | |
| $[Fe_{0.08}Al_{0.92}PO_4]_6F_2.[C_5H_9N_2]_2$ | 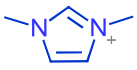 | 12.10 | 1.81 | 5.71 | | | |

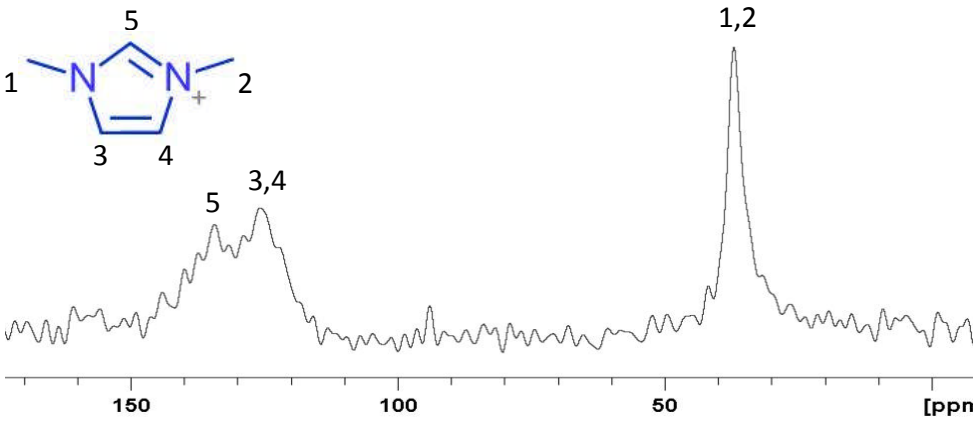


Figure 4.6: $^{13}C$ CP/MAS NMR spectrum of as-synthesized FeAPO-34

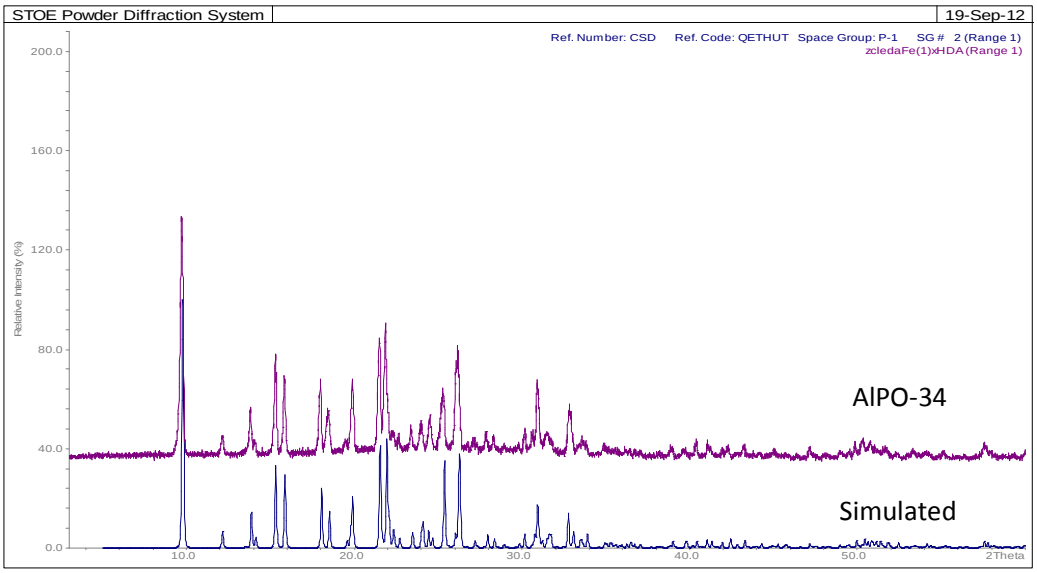


Figure 4.7: PXRD pattern of AlPO-34 obtained in the absence of EDA

## 4.4.3: Other elements included in experiment

In this study, several salts of metal acetate and silica ($SiO_2$) also used under the same condition as $Fe^{2+}$ to target different MAPOs and SAPO. However, most of the products obtained from these experiments are amorphous except for $Zn^{2+}$ and $Ni^{2+}$ which formed AlPO-34 (shown in Table 4.2). The presence of the EDA in the reactions might be not applicable under this condition to optimise the solubility of the metals and silicon in the solution reaction the $Zn^{2+}$ and $Ni^{2+}$ were used in the reaction, the $Zn^{2+}$ and $Ni^{2+}$ not incorporated within the skeleton of AlPO-34 framework but probably stayed in the solution. Thus, from these experiments can conclude that only FeAPO-34 and AlPO-34 are accessible under these conditions.

Table 4.2: Composition of products obtained from metals inclusion experiments

| Metal | Compound Obtained | Powder colour |
|---|---|---|
| $Zn^{2+}$ | AlPO-34 | White |
| $Ni^{2+}$ | AlPO-34 | White |
| $Mg^{2+}$ | amorphous | White |
| $Cu^{2+}$ | amorphous | White |
| $Co^{2+}$ | amorphous | White |
| $Si^{4+}$ | amorphous | White |

## 4.4.4: Thermogravimetric Analysis (TGA) of FeAPO-34

Thermogravimetric analysis (TGA) of as-synthesized FeAPO-34 material has been heated to 650 $^{o}$C. Figure 4.8 shows that two steps of weight loss appear in the TG curve of FeAPO-34. The first weight loss of 6.23% between 25 to 250$^{o}$C is due to the removal of physically adsorbed water. Approximately 19.96% of the expected weight loss appears between 250-550 $^{o}$C which is attributed to decomposition of fluoride ion and 1,3-dimethylimidazolium cation per $[Fe_{0.08}Al_{0.92}PO_4]_6$ formula unit (cal. 24%).[5]

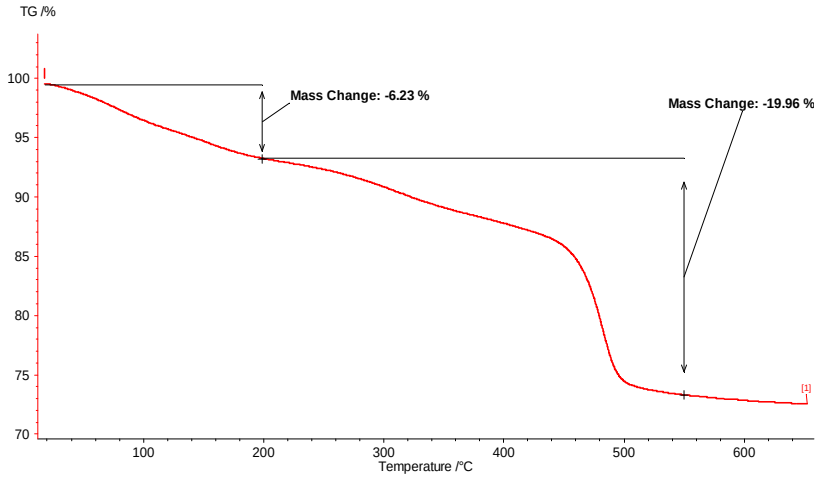


Figure 4.8: The TG curve of as-synthesised of FeAPO-34

## 4.4.5: PXRD pattern of calcined FeAPO-34

The as-synthesised FeAPO-34 was calcined at 550 $^{o}$C under air for 3 hours. After calcination, the template-free material of FeAPO-34 exhibits the sensitivity to humidity when exposed to the air; similar to calcined CoAPO-34 (In Chapter 3). The powder pattern of rehydrated FeAPO-34 contains the extra peaks shown in Figure 4.9 (i)) corresponding to two different hydrated phases of triclinic symmetry.[10] This sample was treated at 200 $^{o}$C under overnight vacuum and the powder pattern illustrated in Figure 4.9 (ii) is well matched with the rhombohedral structure of CHA.

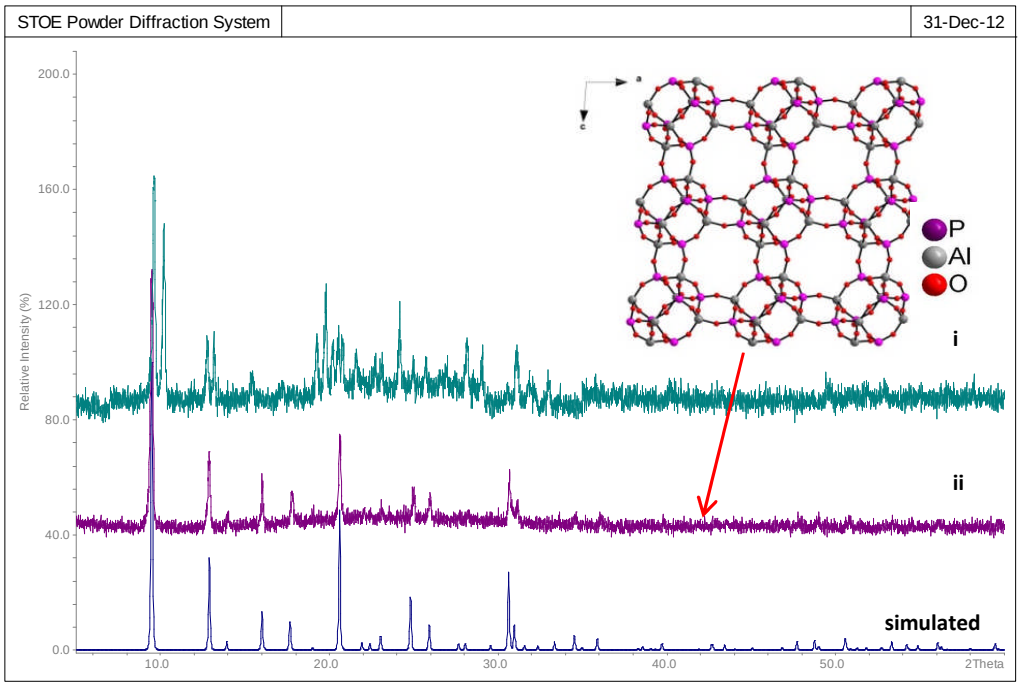


Figure 4.9: PXRD pattern of (i) rehydrated FeAPO-34 (ii) dehydrated FeAPO-34. Inset shows the rhombohedral CHA structure.

The powder pattern of dehydrated FeAPO-34 in Figure 4.10 was fitted using 'Le Bail' method. The unit cell refinement using space group R-3 demonstrated the rhombohedral lattice parameter for the FeAPO-34: a = 13.6919 (12) Å, b = 13.6919 (12) Å, c = 14.8953 (24) Å, α = 90 $^{o}$, β = 90 $^{o}$, γ = 120 $^{o}$ with agreement factor of wRp = 0.0977 and Rp = 0.0764. These cell parameters agree with the verified unit cell for the triclinic CHA topology: a = 13.6750 Å, b = 13.6750 Å, c = 14.7670 Å, α = 90 $^{o}$, β = 90 $^{o}$, γ = 120 $^{o}$.

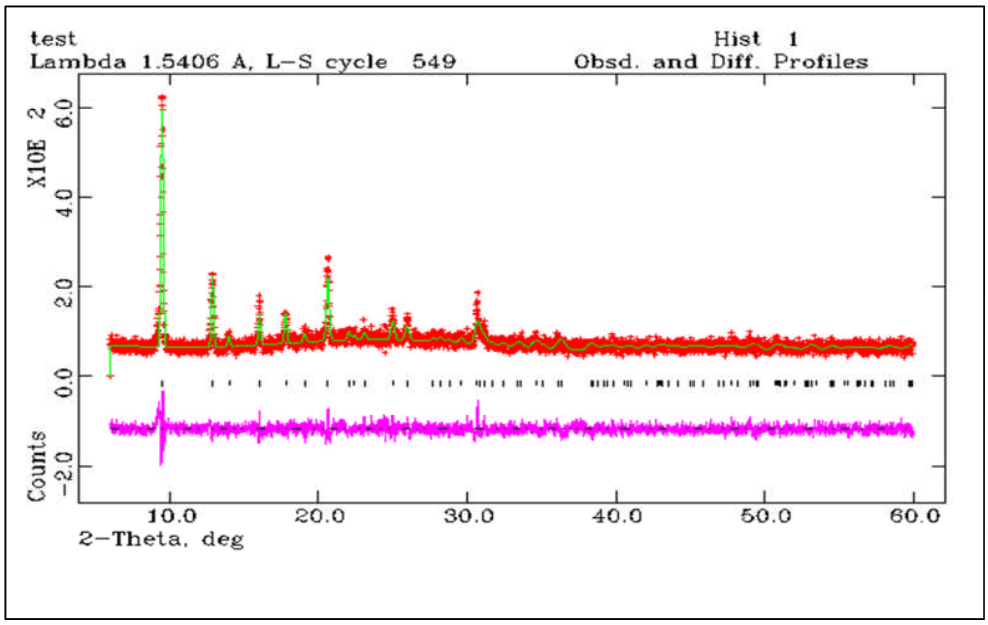


Figure 4.10: Structureless PXRD (and other figures of that type) 'Le Bail' refinement of dehydrated FeAPO-34 (red crosses indicate experimental data, the green line is the calculated data and the pink line (bottom) is the difference profile between them)

## 4.4.6: $^{27}$Al MAS NMR of FeAPO-34

Figure 4.11 (a) shows the $^{27}$Al MAS NMR of as-synthesised FeAPO-34. The chemical shift of $^{27}$Al spectra at 44.8 and -6.2 ppm are assigned to tetrahedral $Al(OP)_4$ and octahedral aluminium, respectively.[11] The octahedral coordination is attributed to $^{27}$Al bonded with two fluorines and four oxygens in the framework.[12] After calcination the rhombohedral structure of dehydrated FeAPO-34 only consists of tetrahedral signal at 37.8 ppm in Figure 4.11 (b)) which is attributed to the $AlO_4$ tetrahedral coordinated in the CHA framework.[11] The octahedral resonance has disappeared in this spectrum indicating that the bond between aluminium and two fluorines has been destroyed.[8] This is supported by the EDX analysis where no fluorine signal is displayed in

Figure 4.12(b). However, $^{27}$Al MAS NMRspectrum shows tiny shoulders at 41.5 ppm and 34.6 ppm which due to the presence of small hydrated species.[11]

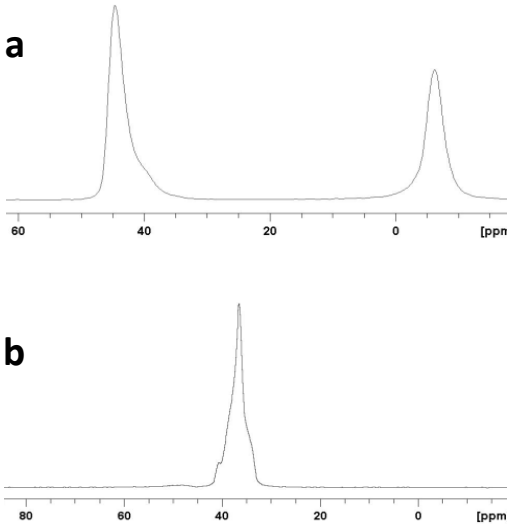


Figure 4.11: $^{27}$Al MAS NMR of (a) As-synthesized FeAPO-34 and (b) dehydrated FeAPO-34

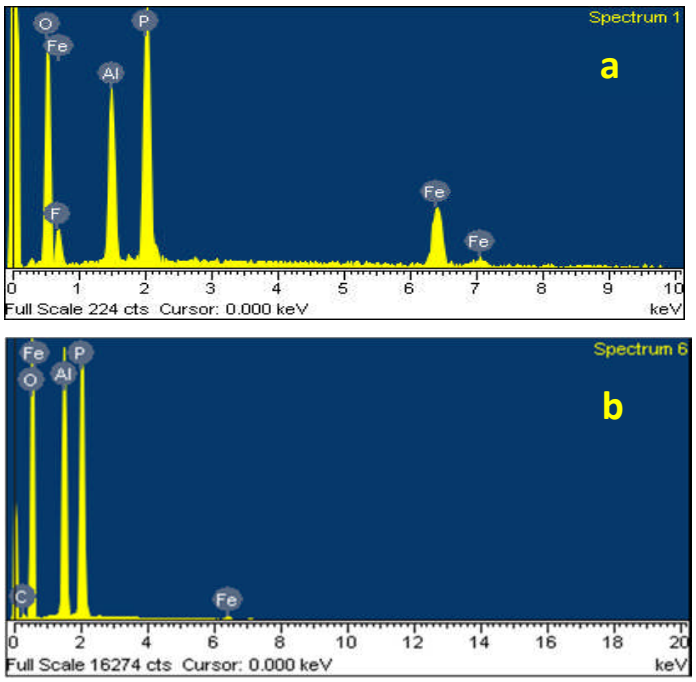


Figure 4.12: EDX spectrum of (a) As-synthesised FeAPO-34 and (b) Calcined FeAPO-34

## 4.4.7: $^{31}$P MAS NMR of FeAPO-34

The $^{31}$P MAS NMR spectrum of FeAPO-34 (Figure 4.13(a)) shows three sharp lines at -7.8, 23.6 and 29.5 ppm for the three phosphorus sites which are related to the P $(OAl)_4$ tetrahedral and is consistent with the triclinic structure of AlPO-34.[8] The chemical shift is also influenced by deshielding effect of fluorines in the framework. The very low field resonance at -7.5 ppm is attributed to the phosphorus nearest the fluoride bridges in the structure.[8, 12] Normally, the $^{31}$P NMR spectrum of calcined FeAPO-34 possess single signal around -30.3 ppm which is attributed to the one type distinguishable $P(OAl)_4$ tetrahedral environment [13] as shown in Figure 4.13(b).

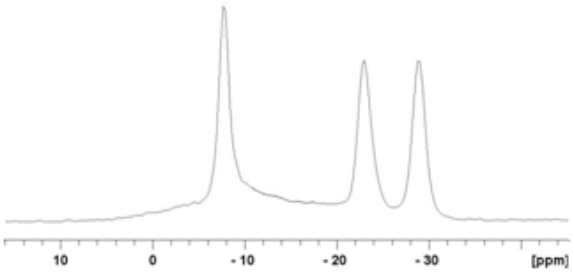


Figure 4.13(a): $^{31}$P MAS NMR spectrum of as-synthesized FeAPO-34

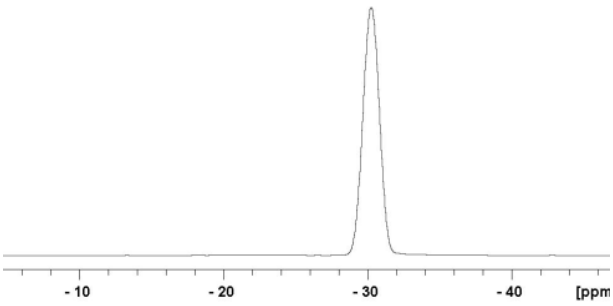


Figure 4.13(b): $^{31}$P MAS NMR spectrum of dehydrated FeAPO-34

## 4.4.8: Broad line $^{31}$P NMR of FeAPO-34

Figure 4.14 (a) shows the $^{31}$P MAS NMR spectra of both as-synthesised and calcined FeAPO-34. Since the conventional method of $^{31}$P MAS NMR is not suitable to detect the very low signal of paramagnetic Fe(II) or Fe(III) interacting with $^{31}$P nuclei, therefore, in this study once again the spin-echo mapping technique was used to determine the substitution of iron with aluminium in the FeAPO-34 framework. The hyperfine coupling and pseudocontact interaction of unpaired electrons of paramagnetic Fe(II) or Fe(III) ions with $^{31}$P nuclei in FeAPO-34 can be detected by the broad line $^{31}$P NMR spectrum. In this study, the broadline signal $^{31}$P NMR spectrum of both as-synthesised and calcined FeAPO-34 appears around 1000 to 14000 ppm (shown in Figure 4.14 (b)). From this spectrum it can be seen that the FeAPO-34 broadline signal was enlarged until 14000 ppm, which is larger than 5000 ppm of CoAPO-34 broadline signal (shown in Figure 3.24, in Chapter 3). The enlarging of the FeAPO-34 broadline signal is probably because Fe(II) or/and Fe(III) possess larger spin quantum numbers of $S$=2 and $S$= 5/2, respectively, compared to $S$=3/2 of Co(II). This result was also found on FeAPO-34 and CoAPO-34 which were hydrothermally prepared, reported by Mali *et. al*, 2005.[14] Another possible reason is the number of unpaired electrons that possessed by paramagnetic Fe(II)/Fe(III) is higher than that of the Co(II) ions, leading to an expansion of the paramagnetic shift of FeAPO-34 to 14000 ppm. This expansion paramagnetic shift could be caused by either of these two reasons or by a combination of both occurring at same time. In the figure, the slight humps also appear in the broad signal for both spectra of as-synthesised and calcined sample. This is might be due to the overlap of the number of slightly different and displaced CSA-like signals that belonging to the phosphorus nuclei that occupy in several crystallograpically distinct sites, experiencing interaction with iron ion sitting in several different positions in the framework that also depends on the Fe-O-P bond length or the bond angle. Shorter bonds length or closer angles induce stronger hyperfine coupling.[14]

As similar to CoAPO-34 ( discussed in Chapter 3), the single signal at δ ≈ 0 ppm in the spectrum of as-synthesised FeAPO-34 ( shown in Figure 4.14 (b(i)) can be attributed to the phosphorus nuclei within the $P(OAl)_4$ environment from three different crystallographic sites (shown in $^{31}P$ MAS NMR spectrum in Figure 4.14(a(i)), while for the calcined sample, the single signal at 0 ppm in the spectrum ( shown in Figure 4.14 b(ii)) is due to one different type of $P(OAl)_4$ environment present in the sample (shown in Figure 4.14(a(ii)). This $P(OAl)_4$ environment possesses slower transverse relaxation than for phosphorus nuclei in the $P(OAl)_{4-n}(OFe)_n$ environment. The chemical shift of broadline $^{31}P$ NMR signal of FeAPO-34 is depend on number of Fe atoms in the first coordination sphere around the P nucleus, where the signal will be shifted towards low fields in the order $P(OAl)(OFe)_3$>$P(OAl)_2(OFe)_2$>$P(OAl)_3(OFe)$, as well as proportional to the electronic density of Fe atoms on the P nucleus.[14] In this study the empirical formula of FeAPO-34 has been assumed as $[Fe_{0.08}Al_{0.92}PO_4]F_2$. $R_2$. Assuming that each site occupying is independent (i.e. there is no clustering of Fe etc), then the probability of any one Al being replaced by Co is 0.08. The probability of having a $P(OAl)_3(OFe)$ unit is therefore $4 \times 0.92^3 \times 0.08 = 0.24$.

Figure 4.14(b(ii)) shows that upon calcination, the broadline signal of FeAPO-34 exhibits broadening. In this study, the investigation of $^{31}P$ NMR line width of FeAPO-34 was not further done in detail, however, this line broadening also was found on calcined FeAPO-34 and FeAPO-36 reported by Mali *et.al* in 2005. They reported that this line broadening was due to the oxidation of Fe(II) ($S$=2) to Fe(III)($S$=5/2), indicating that higher spin quantum number ($S$) will increase the NMR line broadening. They also have suggested that probably some of iron leached out from the framework during calcination and were trapped within the cavities, since the amount of iron was found in the calcined sample from EDX analysis approximately same as the as-synthesised FeAPO-34. [14]

Overall, the presence of broadline signal around 1000 to14000 ppm in $^{31}P$ NMR spectrum of both as-synthesised and calcined FeAPO-34 confirm that the Fe(II)/Fe(III) ions were successfully incorporated within the skeleton of FeAPO-34 framework, indicating that the presence of Fe-O-P bridges in FeAPO-34 framework which is probably necessary to delocalise the unpaired electrons of iron metal on $^{31}P$ nuclei.

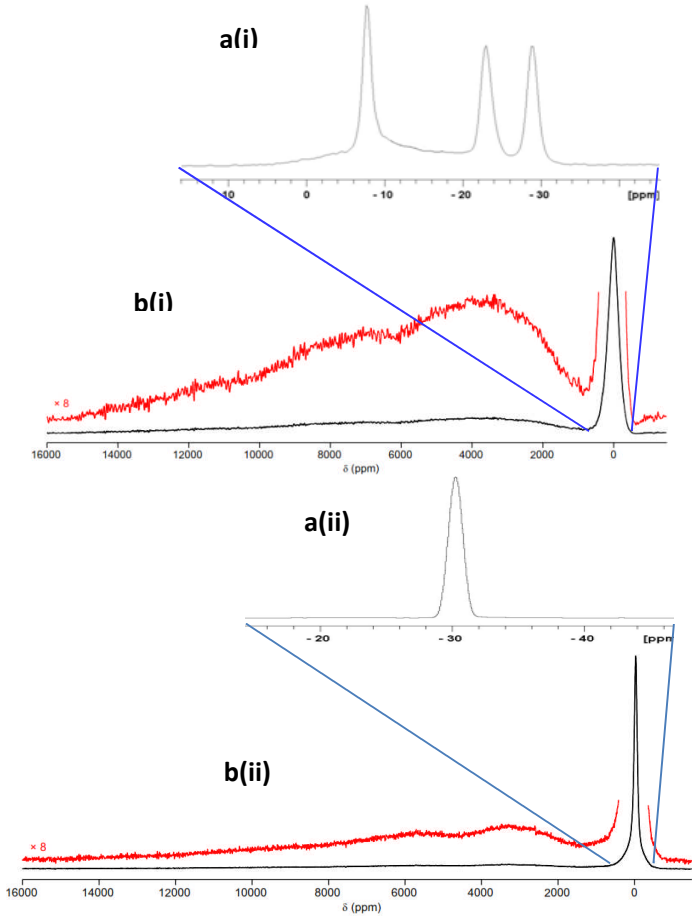


Figure 4.14: $^{31}P$ MAS NMR spectrum of (a(i)) As-synthesized, (a(ii)) Calcined FeAPO-34 , Static $^{31}$ P spin-echo spectrum of (b(i)) as-synthesised and (b(ii) calcined FeAPO-34. The red broad line spectrum was scaled up to 8 magnifications is identical with black spectrum

## 4.4.9: Morphology of FeAPO-34

The SEM characterisation of both as-synthesised and calcined CoAPO-34 was carried out to observe the morphology differences of the samples. Images of both samples taken at 200 x magnification are shown in Figure 4.15 a(i) and b(i). According to these images, that there is no significant difference between these two samples. These figures also show that the sample particles have no consistent shape or size. When the morphology images were taken at higher magnification of 600 x (shown in Figure 4.15 a(ii) and b(ii)), these figures show that the selected particle morphological structures seems formed by agglomeration of small particles and are stacked together. From these pictures, it is clear that the sample not only retains its crystallinity after calcination (see PXRD pattern in Figure 4.10), but also the morphologies of the particles remain mainly the same. Comparing the particle size of FeAPO-34 and CoAPO-34 (In Chapter 3, section 3.4.12) at 600 x magnification, the FeAPO-34 particles are bigger than CoAPO-34.

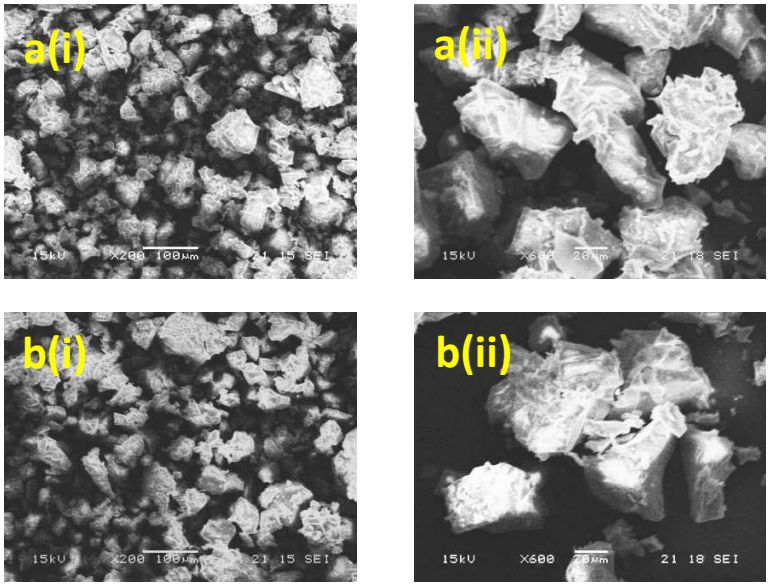


Figure 4.15: Morphology of FeAPO-34; as-synthesised a(i) 200x and (ii))600x; calcined b(i)) 200 and (b(ii)) 600 x magnification

## 4.4.10: Absence of HF

Initially, in this work, the synthesis of FeAPO-34 was carried out using HF. In order to see the difference, the same experimental method was attempted without HF. The product obtained from this experiment was white crystals of SIZ-6 layered aluminophosphate. As expected, the layered structure material can be achieved under this condition. This is because generally when the ionothermal synthesis was carried out fluoride free, the low dimensional structure is produced, while the presence of fluoride leads to the formation of fully connected frameworks.[15] Figure 4.16 illustrates the SIZ- 6 diffraction pattern is well matched with the theoretical pattern of SIZ 6.[16] The EDX elemental analysis shows that the iron percentage in SIZ-6 is less than 0.007%, suggesting that this metal is not present in the material. In this study the same experiment method was also carried out without using HF together with EDA, unfortunately there was no product obtained, which was only clear solution acquired in the Teflon line.

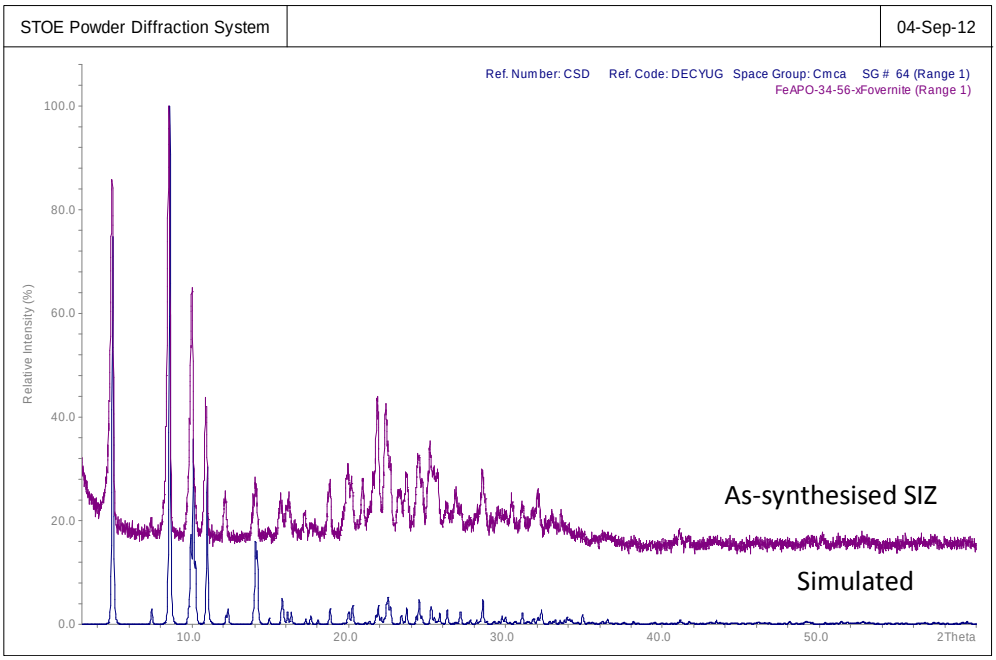


Figure 4.16: PXRD pattern of as-synthesised SIZ 6

Figure 4.17 displays the powder pattern of SIZ 6 was fitted by Le Bail method using GSAS program. The unit cell has refined using space group Cmca (no. 64) gave orthorhombic structure to SIZ 6 lattice parameters: a = 17.5146 (19) Å, b = 18.1083 (22) Å, c = 35.5237 (42) Å, α = β= γ= 90 $^{o}$ with agreement factor *wRp* = 0.0650 and *Rp* = 0.0445. These unit cell parameters matchto the verified unit cell of SIZ 6 structure:[16] a = 17.5472 Å, b = 18.0516 Å, c = 35.5602 Å, α = β= γ= 90 $^{o}$

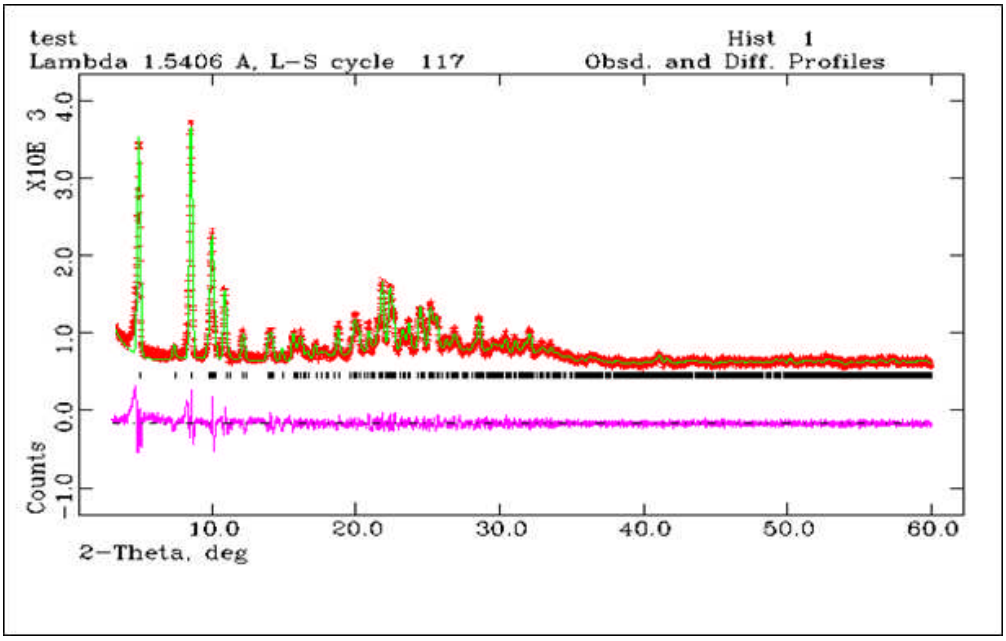


Figure 4.17: Structureless PXRD (and other figures of that type) 'Le Bail' refinement of Fe-SIZ 6 (red crosses indicate experimental data, the green line is the calculated data and the pink line (bottom) is the difference profile between them)

Previously, SIZ-6 was prepared using 1-ethyl-3-methylimidazoliumbromide (EMIMBr) by E.R Parnham *et.al* in 2006. The asymmetric unit of SIZ-6 framework can be demonstrated in Figure 4.18 where the structure contains of 7 and 5 of independent phosphorus and aluminum atoms,

respectively. All the phosphorus atoms display tetrahedral coordination by oxygen, while 3 atoms of aluminium are tetrahedral coordinated by oxygen and one in a regular octahedron Al5. The remaining aluminium atom of Al2 is mainly in five coordinated which is partially occupied by oxygen atom from the water molecule remaining from the phosphoric acid source.[16]

(a)

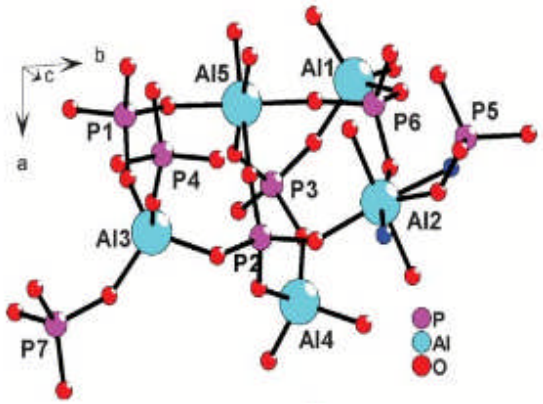


(b)

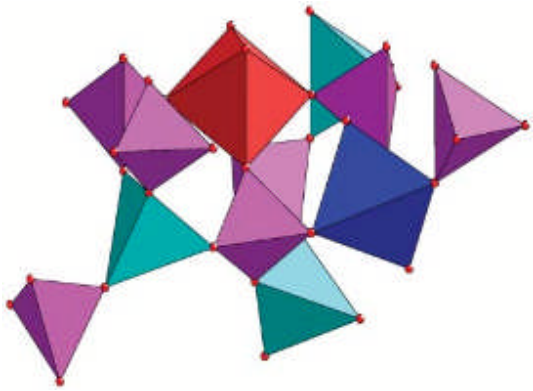

Figure 4.18: (a) Asymmetric unit of SIZ-6 with seven phosphorus and five aluminium atoms. The minor atoms of oxygen disorder present around Al2 are shown in blue, (b) Polyhedral representation of the symmetric unit displays one octahedral (red), three tetrahedral (cyan) and one pentacoordinate (blue) aluminium[16]

Overall the SIZ-6 structure is illustrated in Figure 4.19 comprises the anionic aluminophosphate layers of the chemical composition $Al_4(OH(PO_4)_3(HPO_4)(H_2PO_4)^-$. The layered structure containing 4, 6 and 8 rings and the 8-ring windows shown in Figure 4.20 are sufficient for the layers conceivably porous for the small molecules. The layers are held together by the strong relatively hydrogen bonding. This occurs because the two $H_2PO_4$ groups, one each from two adjacent layers generates dimeric unit with O-O distances across the hydrogen bond. The negative charge on the layers is balanced by one $EMIM^+$ cation which occupies in the interlayer space.[16]

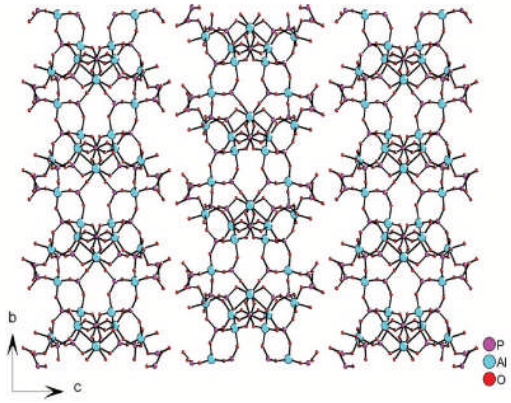


Figure 4.19: The layered structure of SIZ-6 held by $HPO_4$ dimers through hydrogen bonding

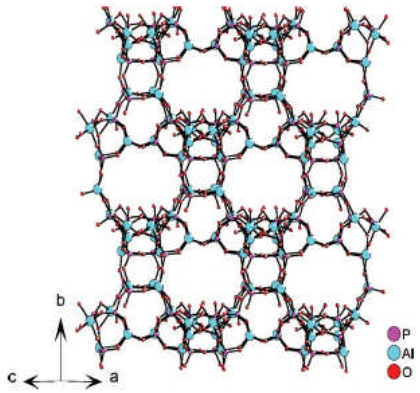


Figure 4.20: A view of 8-ring windows in the layer of SIZ-6

## 4.4.11: $^{13}$C CP/MAS NMR of SIZ-6

$^{13}$C CP/MAS NMR measurement was carried out to determine the presence of templates in SIZ-6 material. The solution $^{13}$C CP/NMR spectra of EMIMCl and EDA shown in Figure 4.21 are used as references to help this analysis. Figure 4.22 shows that the $^{13}$C MAS NMR spectrum of SIZ-6 consists of five distinct signals. These signals are corresponding to the 1-ethyl-3-methylimidazolium cation ($EMIM^+$) resonances. The first signal at highest field of 16.5 ppm is due the methyl group ($C_1$) while both signals at 37.3 and 45.5 ppm are assigned to $C_6$ and $C_2$, respectively. The signal appears at 128.6 ppm is attributed to the overlapping of $C_4$ and $C_5$ signals, whilst the remaining signal at lowest field of 135.2 ppm is assigned to $C_3$. In this spectrum it is difficult to observe $CH_2$ signal of EDA at 47.3 ppm. This gives two possibilities, either the $CH_2$ signal overlapped with ethyl group ($C_2$) from $EMIM^+$ or EDA is not present in the SIZ-6 framework. Thus, CHN analysis was carried out to clarify this. Table 4.3 shows the CHN results of SIZ-6. When comparing those results including the expected theoretical formulas of SIZ-6 from this table, the experimental carbon, hydrogen and nitrogen percentages of 9.5%, 1.9 **%** and 3.6%, respectively, are very near to theoretical values for $[Al_4(OH)(PO_4)_3(HPO_4)(H_2PO_4)(H_2O)_{0.2}][C_6H_{11}N_2]$. These results, strongly suggest that only $EMIM^+$ resides in the interlayer spaces or channels in SIZ-6 material, indicating that one $EMIM^+$ compensates the negative charge of per $[Al_4(OH)(PO_4)_3(HPO_4)(H_2PO_4)(H_2O)_{0.2}]^-$ formula unit, which is similar to SIZ-6 reported by Morris *et. al* in 2006.[16] These results also clearly show that EDA was not present in SIZ-6 and probably just stayed in the solution. This is also in agreement with TGA analysis where the weight loss percentage of organic compound from SIZ-6 is about 16.49%, which is very close to theoretical composition of $EMIM^+$ per $[Al_4(OH)(PO_4)_3(HPO_4)(H_2PO_4)(H_2O)_{0.2}]$ formula unit (cal. 15.4%). In this work, although EDA was not present as template or space filler in the SIZ-6, it plays important role, which seems to

help the nucleation process and crystalisation of SIZ-6. As mentioned in section 4.4.10, without EDA in the reaction there was no product obtained.

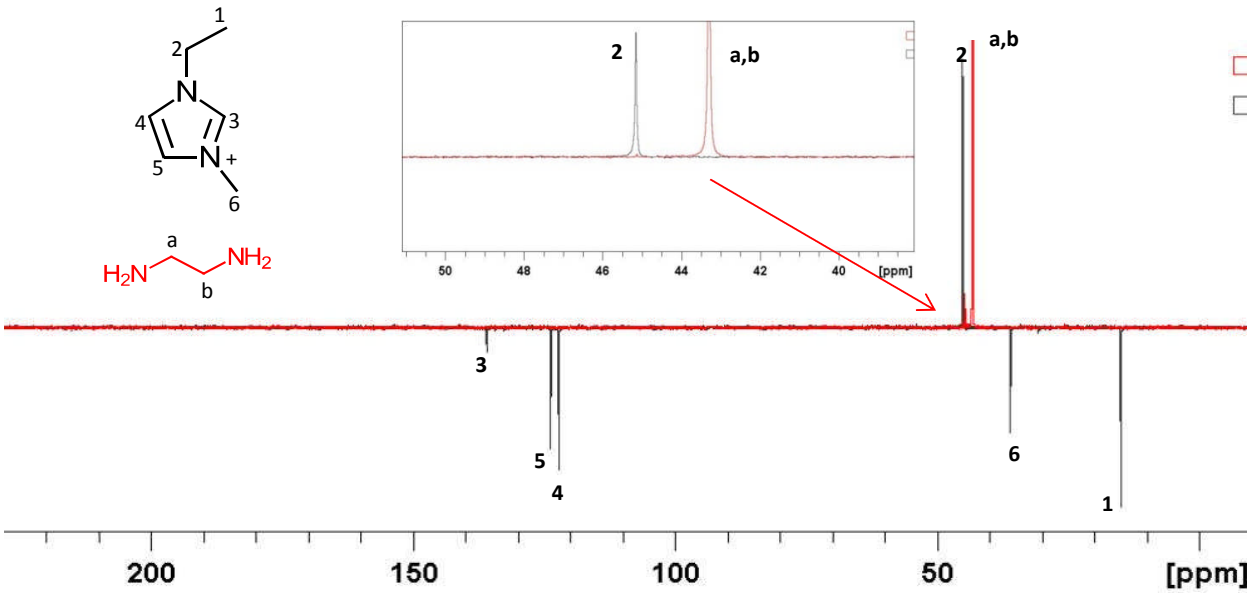


Figure 4.21: Solution $^{13}C$ DEPTQ CP/NMR spectrum of EMIMCl (black) and EDA (red)

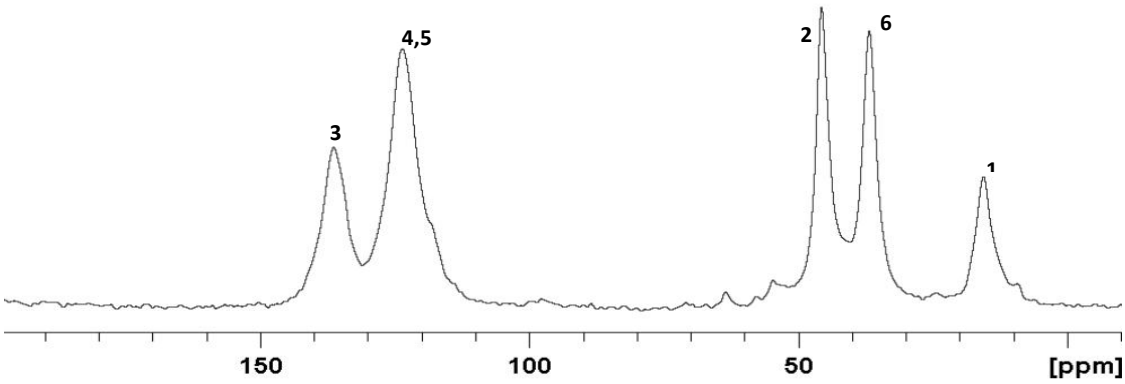


Figure 4.22: $^{13}C$ CP/MAS NMR spectrum of SIZ 6

Table 4.3: Carbon, Hydrogen and Nitrogen Percentage of SIZ 6

| Molecular Formula | Template expected | Calculation % | | | Experiment % | | |
|---|---|---|---|---|---|---|---|
| | | C | H | N | C | H | N |
| $[Al_4(OH)(PO_4)_3(HPO_4)(H_2PO_4)(H_2O)_{0.2}][C_6H_{11}N_2]$. $[C_2H_8N_2]$ | 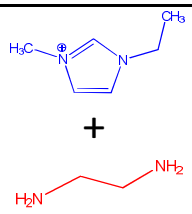 | 12.3 | 3.0 | 7.0 | 9.5 | 1.9 | 3.6 |
| $[Al_4(OH)(PO_4)_3(HPO_4)(H_2PO_4)(H_2O)_{0.2}][C_6H_{11}N_2]$ | 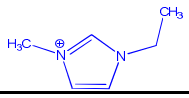 | 10.0 | 1.5 | 4.0 | | | |
| $[Al_4(OH)(PO_4)_3(HPO_4)(H_2PO_4)(H_2O)_{0.2}][C_2H_8N_2]$ |  | 3.0 | 1.2 | 4.2 | | | |

## 4.4.12: Thermal Analysis of SIZ 6

The Thermogravimetric (TG) curve of as-synthesised SIZ 6 is shown in Figure 4.23 and reveals two steps of mass loss. The first weight loss of 7.16 % occurs between 25 and 250 $^{o}$C is corresponding to water lost from formula unit plus water formed from the condensation of the hanging P-OH bonds and small amount of water bound to the aluminium in the sample.[16] The expected weight loss of 16.49 % occurs between 250 and 460$^{o}$C is assigned to the decomposition of 1-ethyl-3-methylimidazolium per formula unit '$[Al_4(OH)(PO_4)_3(HPO_4)(H_2PO_4)(H_2O)_{0.2}]$' (cal. 15.4%). From this curve also can be seen that the decomposition process still occurs above 460$^{o}$C, which can be attributed to the breaking down of the material framework when the condensation of the phosphate group takes place.[16] This supported by PXRD pattern of calcined SIZ-6 (shown in Figure 4.24 (b)), when this material was calcined to 460$^{o}$C, the SIZ-6 structure has undergone crystallographic collapse and eventually the amorphous structure was obtained. Normally the thermal stability of anionic framework

AlPOs such as 2D layered structures are less stable than three dimensional (3D) neutral framework AlPOs, which remain crystalline and exhibit great thermal stability between 400 to 600 $^{o}$C after removal of template.[17]

However, not all the layered AlPOs structure are collapsed after calcination, for example the calcination of layered [F, Tet-A]-AlPO-1 produced into 3D framework of AlPO-41 with AFO topology, which reported by Morris *et.al* in 2006. They proposed the idea that the first layers undergoing the a translation along the *a* and *b* axis of about 8.4 Å and 4.8 Å, respectively followed by condensation in the *c* –direction to produce AlPO-41 (shown in Figure 4.25).[18]

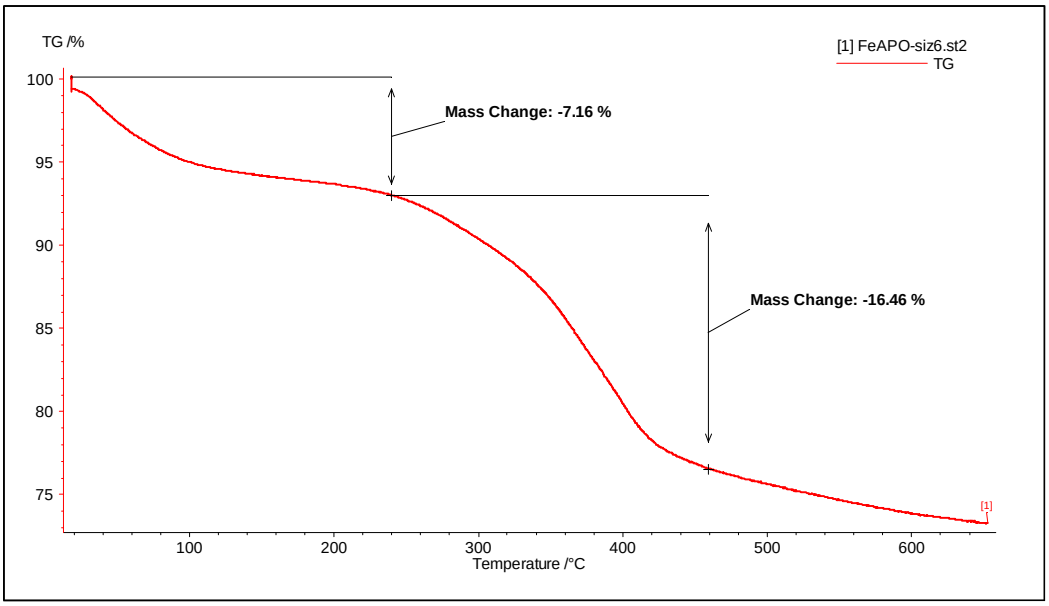


Figure 4.23: The TG curve of as-synthesised SIZ 6

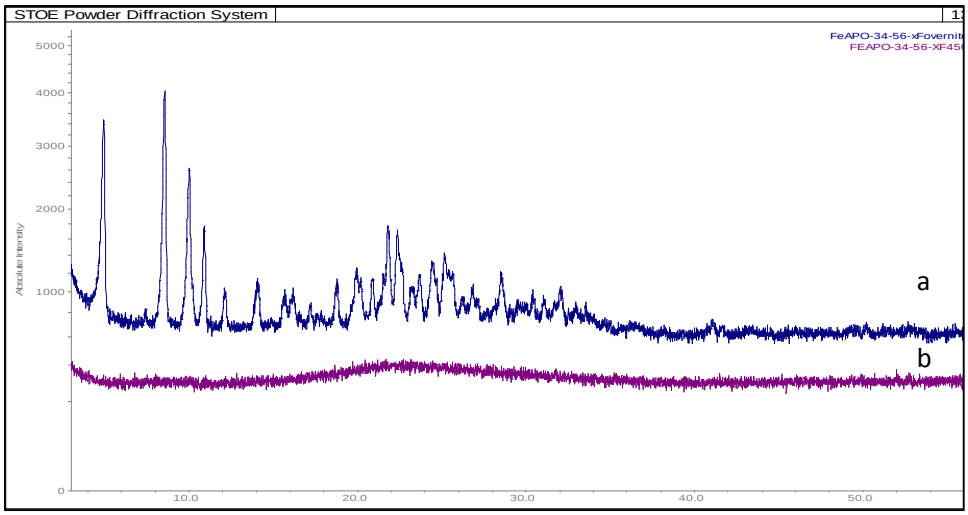


Figure 4.24: Powder pattern of (a) as-synthesised SIZ 6 and (b) calcined SIZ 6

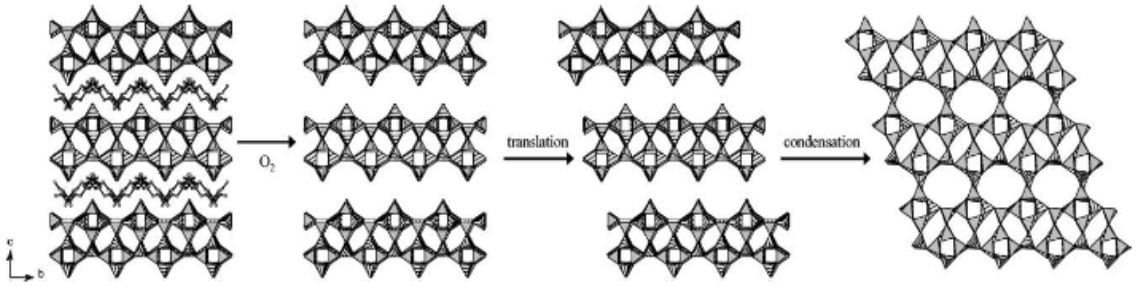


Figure 4.25: Transformation of [F, Tet-A]-AlPO-1 to AlPO-41 (AFO) by calcination[18]

The transformation of 2D layered into 3D framework structure by calcination process is not limited to AlPO materials, but it also include other materials such as borosilicate, ERB-1 with MWW topology, which formed from interlayer condensation of silanol groups present on layer surface (shown in Figure 4.26).[19] This type of transformation also occurs to aluminosilicate

ferrierite which called as PREFER transformed to tectosilicate, which was proved as FER-type zeolite.[20] Other layered materials containing ferrierite layer such as MCM-65 [21] can be calcined to produce another crystalline material of CDO framework topology whereas MCM-47 [22] exhibits marked reduction in sample crystallinity through calcination. Zeolite of RUB-41 with framework type code RRO topology also can be prepared from layered precursor, which had been synthesized by topotactic condensation of silicate layers by calcination process of the layer silicate RUB-39.[23]

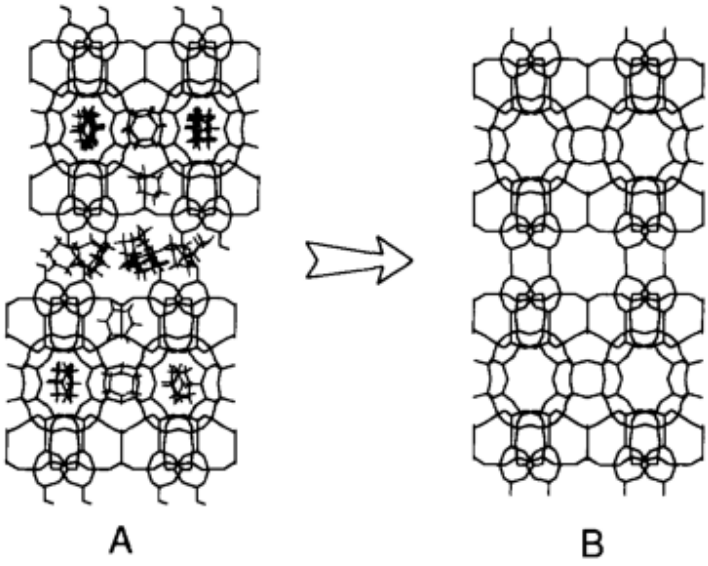


Figure 4.26: Schematic representation of the transformation of borosilicate 2D layered structure (A) to 3D structure of ERB-1[19]

## 4.5: Conclusion

As conclusion, in this study, FeAPO-34 with CHA topology has been successfully prepared under ionothermal condition using EMIMCl with addition of EDA. The pure CHA structure of FeAPO-34 was confirmed by the PXRD pattern. This indicates that FeAPO-34 also can be crystallised under low pressure instead of higher pressure associated with hydrothermal synthesis, providing an alternative way to form FeAPO-34.

Similar to CoAPO-34, FeAPO-34 also shows the typical properties of triclinic CHA structure which distorted to rhombohedral CHA structure through calcination process, removal of template of $DMIM^+$ and fluorine from the framework. This rhombohedral structure demonstrates particular sensitive to air moisture and generates the hydrated phase with triclinic symmetry. This structure can be rebuilt to original structure of rhombohedra CHA structure by evacuation at low temperature.

According to the $^{13}C$ NMR, CHN and TGA analyses, confirm that only $DMIM^+$ was occluded in the FeAPO-34 cage instead of $EMIM^+$ or/and EDA. Without EDA in the reaction, AlPO-34 was obtained, which seems that the EDA plays important role in fixing the solubility of $Fe^{2+}$ in the reaction solution to incorporate within the FeAPO-34 framework.

In this study, the similar experiment as same condition as $Fe^{2+}$ also was attempted using other metals ion (e.g. $Zn^{2+}$, $Ni^{2+}$, $Cu^{2+}$, $Co^{2+}$ and $Mg^{2+}$) and silicon to target MAPOs and SAPO. However, products obtained from this experiment are amorphous or AlPO-34 frameworks. This unsuccessful probably the method and conditions were not suitable to apply to those metals or silicon in order to crystallise MAPOs or SAPO. Additionally, EDA might be was not appropriate to solublise the metals or silicon in the solution reaction, thus, it were not incorporate into AlPO framework.

HF is important additive in the synthesis of FeAPO-34, without HF in the synthesis, low dimensional of 2D layered structure of SIZ-6 AlPO preferentially obtained. This material is less stable and collapsed after the removal of template of EMIM. Although EDA was used in the synthesis, it was not occluded as template or space filler in the channels of SIZ-6. However, EDA plays important role, which seems to help nucleation process of SIZ-6, without EDA no product was obtained.

The broadline signal of as-synthesised and calcined FeAPO-34 visible between 1000 and 14000 ppm in $^{31}$P NMR spectrum strongly suggests that the presence of Fe-O-P bridges in FeAPO-34 framework which is probably necessary to delocalize the unpaired electrons of the metal on $^{31}$ P nuclei. This confirms that $Fe^{2+}$ was successfully incorporated within skeleton of FeAPO-34 framework.

According to the SEM image, there was no significant difference between morphology of as-synthesised and calcined FeAPO-34. The particles of both samples have no consistent shape or size. The particle seems formed by agglomeration of small particles and the particle was bigger than CoAPO-34 ionothermally prepared.

## 4.6: References


1. V. Valtchev, S. Mintova and M. Tsapatsis, *Ordered Porous Solids: Recent Advances and Prospect,* 2009, 115.
2. L. Han, Y. Wang, C. Li, S. Zhang, X. Lu and M. Cao, *AIChE Journal*, 2008, **54**, 280-288.
3. X. Zhao, C. Kang, H. Wang, C. Luo, G. Li and X. Wang, *Journal of Porous Materials*, 2011, **18**, 615-621.
4. X. Zhao, H. Wang, B. Dong, Z. Sun, G. Li and X. Wang, *Microporous and Mesoporous Materials*, 2012, **151**, 56-63.
5. A. Ristić, N. N. Tušar, I. Arčon, F. T. Starzyk, D. Hanžel, J. Czyzniewska and V. Kaučič, *Microporous and Mesoporous Materials*, 2002, **56**, 303-315.
6. J. .J. Spivey, G. F. Froment, W.J.H. Dehertog and A. J. Marchi, *Catalysis*, 1992, **9**, 1-64.
7. A. Tuel, I. Arčon, N. N. Tušar, A. Meden and V. Kaučič, *Microporous Materials*, 1996, **7**, 271-284.
8. E. R. Cooper, C. D. Andrews, P. S. Wheatley, P. B. Webb, P. Wormald and R. E. Morris, *Nature*, 2004, **430**, 1012-1016.
9. E. R. Parnham and R. E. Morris, *Chemistry of Materials*, 2006, **18**, 4882-4887.
10. A. Tuel, S. Caldarelli, A. Meden, L. B. McCusker, C. Baerlocher, A. Ristic, N. Rajić, G. Mali and V. Kaucic, *The Journal of Physical Chemistry B*, 2000, **104**, 5697-5705.
11. N. Rajić, A. Ristić, A. Tuel and Kaučič, *Zeolites*, 1997, **18**, 115-118.
12. Z. Yan, B. Chen and Y. Huang, *Solid State Nuclear Magnetic Resonance*, 2009, **35**, 49-60.
13. N. N. Tušar, V. Kaučič, S. Geremia and G. Vlaic, *Zeolites*, 1995, **15**, 708-713.
14. G. Mali, A. Ristić and V. Kaučić, *The Journal of Physical Chemistry B*, 2005, **109**, 10711-10716.

15. R. E. Morris, *Chemical Communications*, 2009, 2990-2998.

16. E. R. Parnham, P. S. Wheatley and R. E. Morris, *Chemical Communications*, 2006, 380-382.

17. S. T. Wilson, B. M. Lok, C. A. Messina, T. R. Cannan and E.M. Flanigen, *Journal of the American Chemical Society*, 1982, **104**, 1146-1147.

18. P. S. Wheatley and R. E. Morris, *Journal of Materials Chemistry*, 2006, **16**, 1035-1037.

19. R. Millini, G. Perego, W. O. Parker Jr, G. Bellussi and L. Carluccio, *Microporous Materials*, 1995, **4**, 221-230.

20. L. Schreyeck, P. Caullet, J. C. Mougenel, J. L. Guth and B. Marler, *Microporous Materials*, 1996, **6**, 259-271.

21. D. L. Dorset and G. J. Kennedy, *The Journal of Physical Chemistry. B*, 2004, **108**, 15216-15222.

22. A. Burton, R. J. Accardi and R. F. Lobo, *Chemistry of Materials*, 2000, **12**, 2936-2942.

23. Y. X. Wang, H. Gies and B. Marler, *Chemistry of Materials*, 2005, **17**, 43-49.

# CHAPTER 5

# IONOTHERMAL SYNTHESIS OF Cu/DNL-1 AND ITS APPLICATION IN SIMULTANEOUS STORAGE AND PRODUCTION OF NO

## 5.1: Introduction

### 5.1.1: Extra Large Pore Materials

Large or extra-large pore crystalline materials continue to attract attention in industry and academia because of their potential application as molecular sieves in adsorption, separation and shape-selective catalysis. Extra-large pores are defined as rings consisting of greater than twelve tetrahedral atoms.[1] Table 5.1 shows the list of typical (not all listed) materials with structures containing rings of more than 12 tetrahedral atoms and most of them are phosphate-based. [2]

Table 5.1: Representative examples of crystalline materials with ring sizes above twelve[2]

| Material | Year reported | Main framework composition | Ring size (oxygen atoms) | Pore size (nm)* |
|---|---|---|---|---|
| VPI-5 | 1988 | $AlPO_4$ | 18 | 1.2 |
| AlPO4-8 | 1990 | $AlPO_4$ | 14 | <1.0 |
| Cloverite | 1991 | $GaPO_4$ | 20 | <1.0 |
| JDF-20 | 1992 | $AlPO_4$ | 20 | –† |

| | | | | |
|---|---|---|---|---|
| ULM-5 | 1994 | $GaPO_4$ | 16 | ND |
| UTD-1 | 1996 | SiO2 | 14 | ~1.0 |
| ULM-16 | 1996 | $GaPO_4$ | 16 | ND |
| CIT-5 | 1997 | SiO2 | 14 | 0.8 |
| ND-1 | 1999 | ZnPO | 24 | ND |
| FDU-4 | 2001 | $Ge_xO_y$ | 24 | ND |
| NTHU-1 | 2001 | $GaPO_4$ | 24 | ND |
| ITQ-37 [3] | 2009 | GeSi | 30 | ND |
| DNL-1 [4] | 2010 | AlPO4 | 20 | ND |

ND, Not determined. *By adsorption. -† Structural collapse upon removal of organic. Of these zeolitic materials, aluminophosphate molecular sieves are more interesting because of their high stability for used in various field and established processes.[4]

The first extra-large pore aluminophosphate to be discovered was VPI-5 with the VFI framework topology. This porous material consists of 18-ring pore and possesses free diameters of approximately 12-13 Å[1] as shown in Figure 5.1. VPI-5 can be prepared either with or without addition of organic amine into the gel.[5-7] Interestingly, when the synthesis is carried out in the presence of organic species, the organic species do not reside in the channel of the final product, instead, the void spaces in the sample are occupied by water molecules.[6] The thermal stability of VPI-5 is dependent on its preparation method; for instance the thermal and hydrothermal stability of VPI-5 are greater when it is made from tetrabutylammonium hydroxide than dipropylamine. At the some elevated temperatures VPI-5 can be transformed to a 14-ring molecular sieve, designated as AlPO-8.[8]

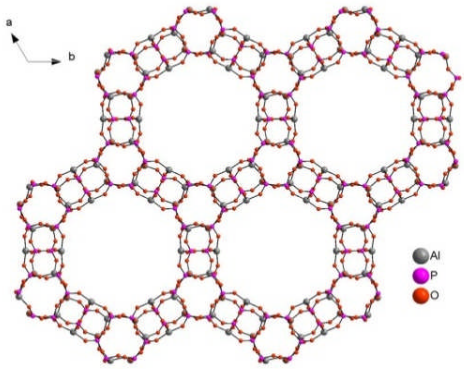


Figure 5.1: VPI-5 framework structure with 18-ring[9]

Larger pore openings in unusual microporous aluminophosphate were also discovered denoted as JDF-20 shown in Figure 5.2. This anionic aluminophosphate structure is composed of 20-ring elliptical channels with a free diameter of 6.2 by 14.5 Å intersected by smaller 10 and 8 membered rings.[10] However, this material could not be classified as a zeolite because its anionic framework with an Al/P ratio of 5:6 is unstable after removal of the template by calcination.[4]

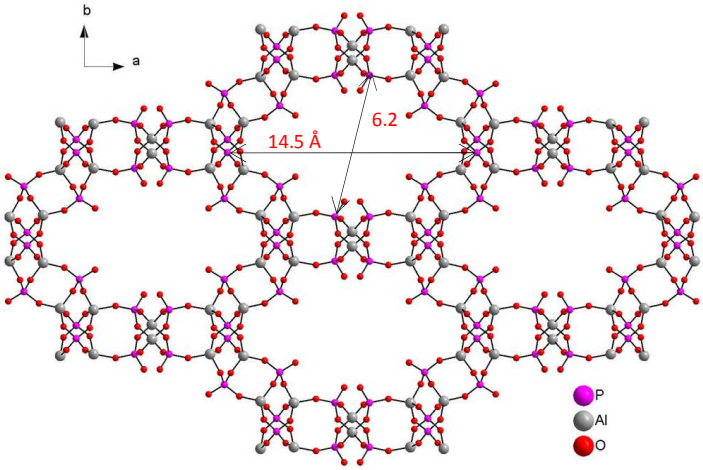


Figure 5.2: JDF-20 framework structure with 20-ring[10]

DNL-1 is the first aluminophosphate molecular sieve that contains extra-large pore of 20-ring. It has been prepared using ionothermal synthesis by Ying Wei *et.al* in 2010. This molecular sieve, shown in Figure 5.3, is isostructural to gallophosphate cloverite (-CLO) that is synthesised under hydrothermal condition. The DNL-1 framework can be described in terms of Al-O-P double four rings (D4Rs) having fluorides in the center and one half this D4Rs have two adjacent T-OH (Figure 5.4). The aluminium atoms distort inward and bond to the fluoride ions in the D4Rs, and therefore it becomes five coordinate, whereas the phosphorus atoms remain four coordinate. Generally, the whole DNL-1 structure can be described as: 1) two nonintersecting three-dimensional systems with 20-ring and 8-ring windows, respectively, 2) four terminal groups (Al-OH and P-OH) protruding into the 20-ring opening to generate a cloverleaf shape, 3) the super cages at the intersection of the 20-ring channels and 4) half of the D4R units not fully connected. The use of ionic liquid as the reaction solvent lead to the first Al-cloverite (DNL-1) that shows excellent stability compared to gallium cloverite. –CLO that decomposed at 700 $^{o}$C while DNL-1 remains intact up to 950 $^{o}$C. Above 950 $^{o}$C the DNL-1 structure changes to the AlPO trydymite dense phase. Therefore, this great stability coupled with extra-large pore size, DNL-1 opens up many potential applications such as catalysis, gas storage and separation.[11]

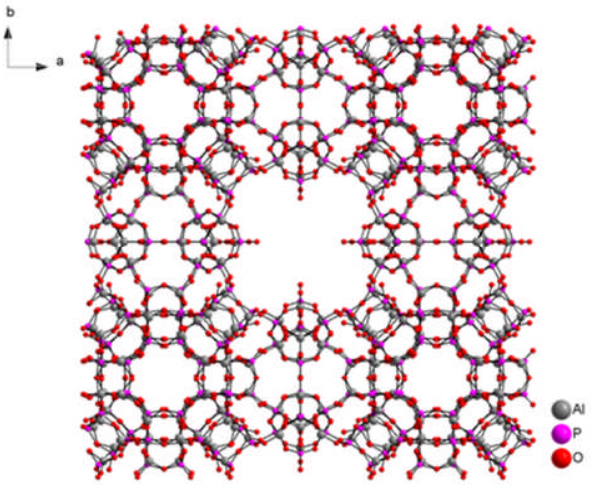


Figure 5.3: The DNL-1 framework structure with 20-ring [12]

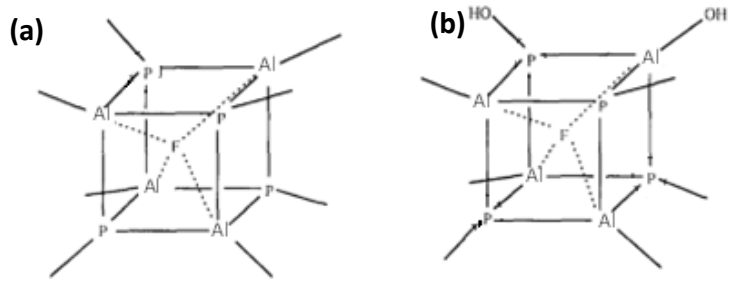


Figure 5.4: Depictions of the two types of double four rings (D4Rs) and the five types of T sites in DNL-1 (-CLO); (a) a D4R with no T-OH groups and (b) a D4R with two adjacent T-OH sites. Solid lines represent Al-O-P bonds except where terminal T-OH bonds are shown and dotted lines represent Al-F bonds.

## 5.1.2: Simultaneous storage and production of NO using zeolite

As mentioned in Chapter 1, zeolites and MOFs are good for NO storage and delivery agents for medical therapies such as preventing thrombus formation and inhibiting platelet aggregation amongst other properties. However, one of the drawbacks to achieve such gas storage and delivery in materials is the finite reservoir of stored NO in the materials and difficulty replacing the NO, especially for long term implants. As an alternative, active gas also can be delivered by producing the gas chemically from a suitable substrate.[13] [14] Morris and co-workers have reported that copper ion exchanged zeolites such as Cu-X , Cu-ZSM-5[15] and Cu-MCM-41[16] can be used to simultaneously store and produce NO from nitrite ($NO_2^-$) using an active Cu(I) species in the zeolites. The cooperative effect of NO storage and production give an exciting example of a strategy to increase and extend the gas delivery well beyond the time frame of possible gas storage materials alone. For instance, this effect is important to inhibit both infection and thrombosis formation in NO-delivery coated medical devices (e.g. catheters, stents and etc.) which remain in contact with blood for prolonged period of time. At present, there are

many efficient medical material coating devices that have been designed and used to deliver antithrombotic,[17] anti-inflammatory[18] and antibodies[19] which combine antibacterial and antiplatelet adhesion [20] properties. However, they all suffer from depletion of the active agent. Currently there are many research works focusing on the use of nitric oxide properties, since this active gas has been discovered as an effective inhibitor of platelet and bacterial adhesion.

Comparing Cu(I) and Cu(II) cations, Cu(I) containing materials are active in transferring an electron to nitrite ($NO_2^-$) to form NO, while Cu(II)-containing materials are not. This also was proven by Morris and co-workers in experiments measuring the NO release of stirred suspensions of Cu(II) and Cu(I) containing zeolites in nitrite solution. When the as-synthesised Cu(II)-containing zeolites were added into the buffer solution (control environment), copper ions were not reduced to Cu(I), and so were inactive for NO production from $NO_2^-$. Moreover, when the nitrite was added into the aqueous solution which only contained Cu(II), the NO was not released, illustrating that the critical role of Cu (I) cations.[15]

In nature, copper metals are always available in biological denitrification, probably because these metals are readily accessible and in stable oxidation states, which are capable binding and activating nitric oxide and may participate in electron-transfer processes. Indeed, nature always evolves the appropriate enzymes and active site chemistries to deliver the optimum function in a given organism.[21] The reaction mechanism of copper-containing nitrite reductases (NiR) of certain types of bacteria in denitrification process has been proposed on the basis of the results for number of biochemical, spectroscopic, and crystallographic studies.[22-26] The method of NO production using copper-containing zeolites, which initially began proposed by Morris *et.al* in 2008,[15] is one of the studies that mimic the bacterial nitrite reductase enzyme. The general mechanism of nitrite reduction is shown in Figure 5.5. In this mechanism, nitrite ($NO_2^-$) bound with reduced $Cu^I$ to form $Cu^I$-$NO_2$. Then, this species is protonated to produce

water and $Cu^{I}$-$NO^{+}$. $Cu^{I}$-$NO^{+}$ is equivalent to unstable species of $Cu^{II}$-N=O and finally it would decomposed to NO and $Cu^{II}$.[21]

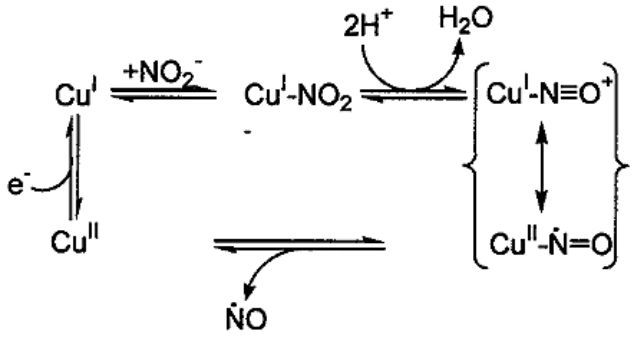


Figure 5.5: General mechanism for Cu-mediated reduction of nitrite[21]

Owing to the exciting method of simultaneously storing and delivering NO materials ( as mentioned above), and the great stability of 20 ring extra-large pore DNL-1 aluminophosphate, in this study the synthesis of copper containing aluminophosphate with cloverite type structure (Cu/DNL-1) was attractive to explore. Moreover, the investigation of simultaneous storage and production of NO from nitrite source of the resulting materials is also interesting. To date, there is no previous example of copper containing aluminophosphates (Cu/AlPOs) used to store and produce NO simultaneously to extend the lifetime of gas delivery.

## 5.2: Aims

The aim of this study is to synthesis Cu/DNL-1 under ionothermal condition using 1-ethyl-3-methylimidazoliumbromide (EMIMBr) in the presence of 1, 6-hexanediamine (HDA) as a co-structure directing agent (SDA). Any effects upon to the structure produced by using different

amounts of EMIMBr, absence of HDA and HF in the reaction are reported. The materials were characterised using PXRD, TGA, EDX, CHNS, SSNMR and SEM techniques. In addition, the research aim is to investigate simultaneously storage and production of NO using Cu/DNL-1.

## 5.3: Materials and Methodology

## 5.3.1: Ionothermal synthesis of Cu/DNL-1

A beaker was charged with $H_3PO_4$ (0.395 g, 0.004 mol, Sigma Aldrich, 99%), $Cu(CH_3COO)_2$ (0.22 g, 0.0012 mol, Acros, 98%), HF (0.175 g, 0.009 mol, Alfa Aesar, 48%), EMIMBr (26.4 g, 0.138 mol), 1,6 hexadiamine (HDA) (0.2 g, 0.0017 mol, Sigma Aldrich, 98%), and $Al[OCH(CH_3)_2]_3$ (0.547g, 0.0027 mol, Alfa Aesar, 98%)). The reaction was stirred and heated to 110 $^{o}$ C for 1 hour. Then the final mixture was transferred into Teflon-lined autoclaves and heated in the oven at 180 $^{o}$ C for 2 hours. The product was centrifuged, washed thoroughly with distilled water and methanol. Afterward, dried for overnight at 110 $^{o}$ C. Eventually the sample was calcined at 550 $^{o}$C for 3 hours under air condition.

## 5.3.2: Characterization

The Powder X-ray diffraction (PXRD) patterns were collected using a STOE STADIP diffractometer operated with monochromated CuKα X-ray (λ = 1.5406 Å) radiation. A JEOL JSM 5600 SEM, integrated with an EDX system was used to image morphology and for elemental analysis. The elemental analysis also was carried out using CHN analyser. Thermal analysis was conducted using Thermogravimetric Analyser (TGA) Netzsch STA 449C under air

condition. $^{27}$Al solid-state MAS NMR spectra of samples were acquired at a magnetic field strength of 14.1 T. The samples were packed into 4 mm rotors and rotated at MAS rates of 12.5-14 kHz. Signal averaging was carried out for 1024 transients and the spectra were acquired using recycle intervals of 0.1 s with typical rf field strengths of ~100 kHz. $^{31}$P solid-state MAS NMR spectra were acquired at a magnetic field strength of 14.1 T. Samples were packed into 4 mm rotors and rotated at MAS rates of 12.5-14 kHz. Signal averaging was carried out for 16 transients. The spectra were acquired using recycle intervals of 30 s with typical rf field strengths of 100-110 kHz. For $^{13}$C solid-state CP MAS NMR, the spectra were acquired at a magnetic field strength of 14.1 T. Samples were packed into 2.5 or 4 mm rotors and rotated at MAS rates of 12.5 kHz and the spectra were acquired using cross polarization (CP) from 1H using optimised contact pulse durations of 0.25 ms, ramped from 90-100% for $^{1}$H, and two-pulse phase modulation (TPPM) $^{1}$H decoupling during acquisition with an rf field strength of ~100 kHz. Signal averaging was carried out for 5120 transients with recycle intervals of 3 s. All the analyses of MAS NMR were performed using a 400MHz HFXY Bruker Avance III spectrometer. Spin-echo of $^{31}$P NMR mapping technique was carried out to determine the presence of copper atom in the Cu/DNL-1 skeleton framework. The experiment was conducted using Bruker Avance II spectrometer equipped with a 9.4 T wide-bore superconducting magnet, operating at Larmor frequency of 161.976 MHz for $^{31}$P. The radio frequency power was ~180 kHz (90 degree pulse of 1.4 ms) and the echo delay was 10 ms. Signal averaging was carried out for 10240 transients for each frequency step with a repeat interval of 0.1 s. Frequency stepping was carried out as needed and spectra for each frequency step were processed and then codded to give the final spectrum.

## 5.3.3: Pressed Disk

0.02 g Cu/DNL-1 powder with 23.3 % of polytetrafluoroethylene (PTFE) were compressed to pellet with diameter of 5 mm and pressed about 30 second by using Specac Pellet Press, 2 tons.

## 5.3.4: Nitric Oxide Loading

Cu/DNL-1 (0.02 g) was dehydrated for overnight at 200 $^{o}$C under vacuum (1mmHg) in glass ampoule. The samples were cooled at room temperature and afterward exposed to nitric oxide (99.5 %, vol., Air liquid, 2 bars) for 1 hour. Vials were evacuated and exposed to dry argon to purge excess free nitric oxide in the vials and then sealed.

## 5.3.5: Nitric Oxide Adsorption/Desorption Isotherm

The adsorption/desorption of nitric oxide gas in the sample was measured using gravimetric system. A CI Electronic Ltd microbalance was thermally stabilized to eliminate external environment effects. The sensitivity of microbalance was 0.1 µg with load reproducibility 0.01%. The adsorption system pressure was monitored by two BOC Edwards Active gauges in the range of 1 x $10^{-8}$ -1 x $10^{-2}$ and 1 x $10^{-4}$ -1 x $10^{3}$ mbar, respectively. ~30 mg of calcined Cu/DNL-1 was initially outgassed at 573 K under 1 x $10^{-4}$ mbar during 24 hours until no further weight loss was observed. The sample temperature was then decreased to 298 K and kept constant by a circulation water bath with temperature accuracy 0.02 K. The counterbalance temperature was kept at same as that of the sample to minimize the influence of the temperature difference on weight readings, and the sample temperature was monitored using a K type thermocouple, located close to sample bucket (<5 mm). The fluctuation of temperature was minimal less than 0.2 K throughout the experiment. NO gas was introduced into the system until the desired

pressure was achieved, and the mass uptake of the sample was measured as a function of time until the adsorption equilibrium was achieved. The adsorption isotherm was obtained by noting the equilibrium sample mass gain for each incremental temperature increase. Desorption of nitric oxide isotherm was achieved by gradual decrease of the system pressure (until $2 \times 10^{-2}$ mbar)[16]

## 5.3.6: Quantification of Nitric Oxide Release by Chemiluminescence

Initially, the instrument was calibrated by first passing air through a zero filter (Sievers, <1 ppb NO) and afterward 91.0 parts per million (PPM) NO gas (Air Products, balance nitrogen). The flow rate was set to 200 mL/min with a cell pressure of 8.5 torr and an oxygen pressure of 6.1 psig.

After the calibration, 2.5 ml of buffer (pH ~ 7.4, Fisher) was placed in the vial equipped with a stirring bar and degasing the solution by flowing the nitrogen about 15 minutes. Next, 0.02 g of Cu/DNL-1 was promptly transferred from the glass ampoule to the glass vial and sealed it. 25 µl (0.005 M) of sodium nitrite ($NaNO_2$) was injected. The sample solution was stirred and measurement recorded immediately. NO release measurements were carried out using a Sievers NOA 280i chemiluminescence Nitric Oxide Analyser.

## 5.4: Results and Discussion

### 5.4.1: Powder X-ray Diffraction (PXRD) pattern Cu/DNL-1

Figure 5.6 illustrates that the X-ray diffraction patterns of both as-synthesized and calcined Cu/DNL-1 are perfectly matched with the simulated pattern of DNL-1 with the -CLO structure. This figure also shows that the calcined sample remains higher crystallinity even after heated to 550 $^{o}$C. Figure 5.7 shows that the powder pattern of calcined Cu/DNL-1 was fitted by 'Le Bail' refinement method using GSAS program. The refinement of unit cell was performed in space group Fm3c generates cubic unit cell parameter to Cu/DNL1: a = 50.8714(10) Å and α = 90 $^{o}$. The residual of the refinement were *wRp* = 0.0955 and *Rp* = 0.0705. These unit cell parameters are slightly smaller but still closely match the cubic structure of DNL-1 topology: a = 51.363 Å and α = 90 $^{o}$.[4]

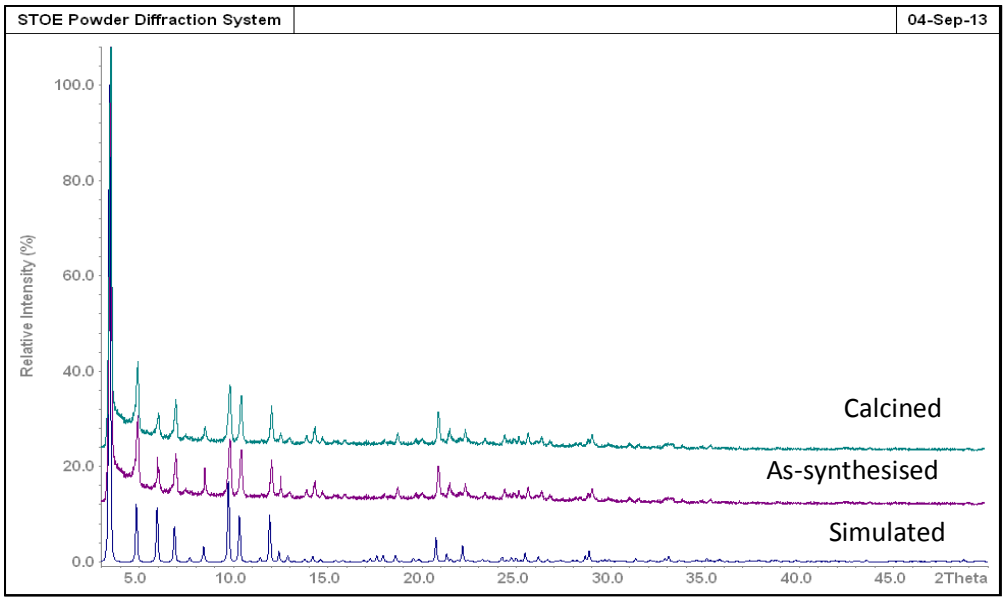


Figure 5.6: PXRD pattern of as-synthesized and calcined Cu/DNL-1

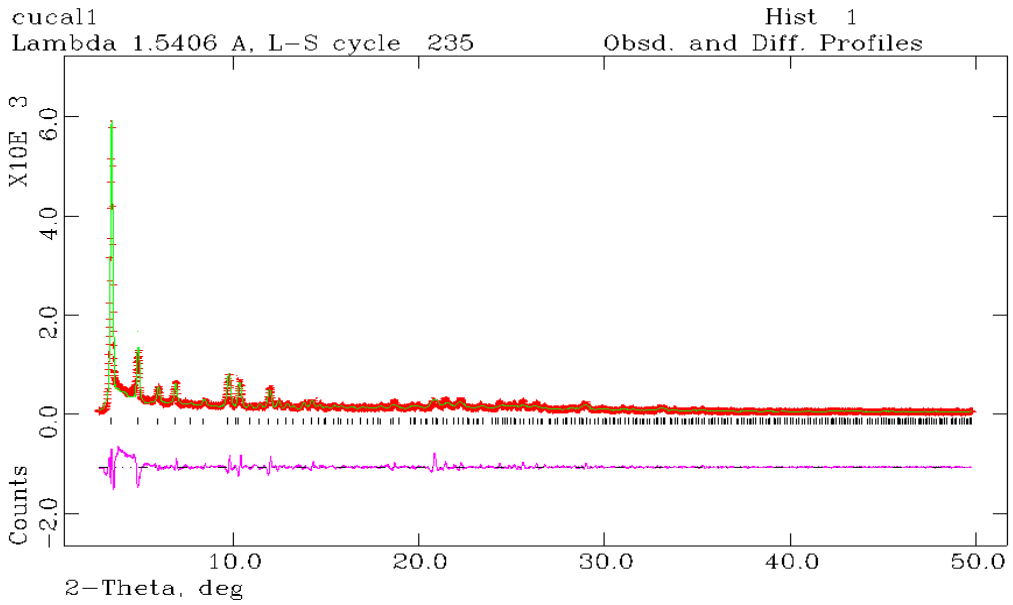


Figure 5.7: Structureless PXRD (and other figures of that type) 'Le Bail' refinement of calcined Cu/DNL-1 (red crosses indicate experimental data, the green line is the calculated data and the pink line (bottom) is the difference profile between them)

## 5.4.2: Elemental Analysis and $^{13}$C CP/MAS NMR of Cu/DNL-1

Figure 5.8 shows that the copper signals appear in both EDX spectra of as-synthesised and calcined Cu/DNL-1. Based on EDX result and referring to the DNL-1 molecular formula $[Al_{768}P_{768}O_{2976}(OH)_{192}F_{288}].[H_2O]_{910}.R$, the average molar ratio of copper in the Cu/DNL-1 has calculated and the mol obtained of the metal in the sample is approximately 40 moles Cu per unit cell of Cu/DNL-1. The copper atoms present in the samples are expected reside in Cu/DNL-1 channels as extra-framework cations and not occupy in the skeleton framework. This was confirmed by spin-echo technique of $^{31}$P NMR which is discussed further in Section 5.4.6. From these result, the chemical formula of Cu/DNL-1 can be assumed as

$[Al_{768}P_{768}O_{2976}(OH)_{192}F_{288}].Cu_{39.24}.[H_2O]_{910}.R.$[11] In this study, this formula is used to help in determining the templates presence in the Cu/DNL-1 material. For the molar ratio of copper in calcined Cu/DNL-1 was obtained to be approximately 39.09 moles Cu per unit cell. Therefore, the empirical formula of calcined Cu/DNL-1 can be assumed as $[Al_{768}P_{768}O_{2976}(OH)_{192}]$. $Cu_{39.09.}$

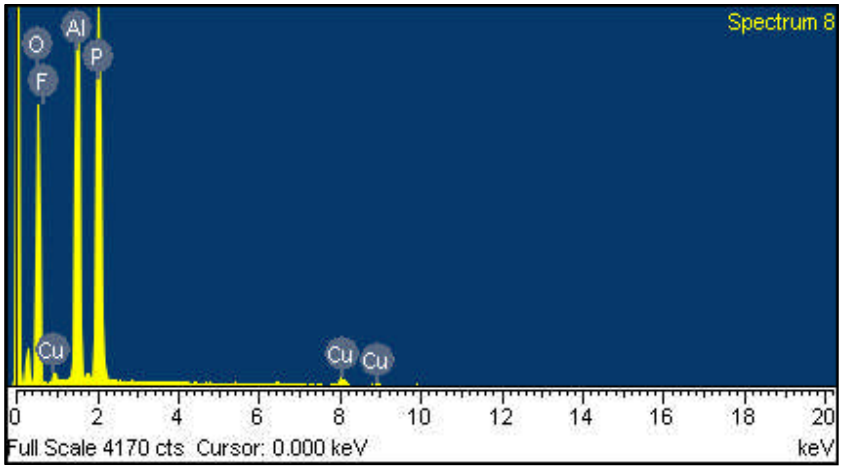


Figure 5.8 (a): EDX spectrum of as-synthesised Cu/DNL-1

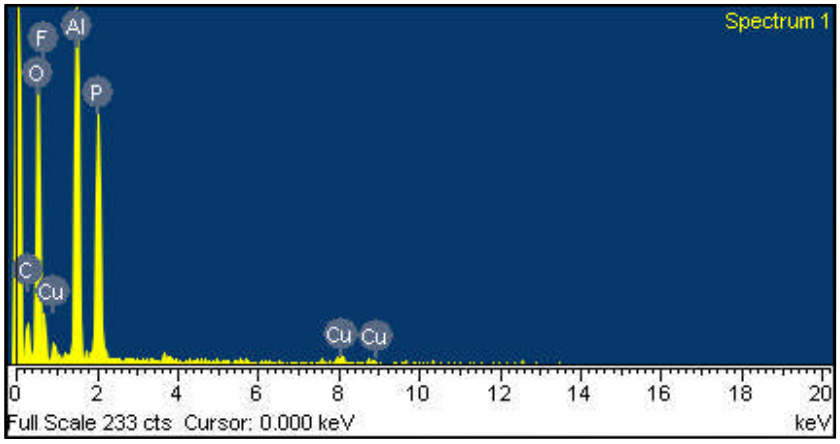


Figure 5.8 (b): EDX spectrum of calcined Cu/DNL-1

The presence of templates in the Cu/DNL-1 was determined using $^{13}C$ CP/MASS NMR. The solution $^{13}C$ NMR spectra of EMIMBr and HDA (Figure 5.9) are used as references to facilitate in determining the templates in the material pores. According to$^{13}C$ CP/MASS NMR spectrum shown in Figure 5.10, the resonances for all carbons of $EMIM^+$ clearly appear in the spectrum as well as the signal at 25.3 ppm of $C_b$ and $C_c$ of HDA. The $C_a$ signal of HDA is also can be seen at 40.5 ppm although it is quite close to $C_2$ signal of $EMIMBr^+$ at 45.5 ppm. This observation reveals that both $EMIM^+$ and protonated HDA remain occluded inside the Cu/DNL-1 channels. This is supported by CHN results (shown in Table 5.2), where the experimental carbon, hydrogen and nitrogen percentages of 10.02%, 3.72% and 4.03%, respectively, are near to the theoretical values obtained for $[Al_{768}P_{768}O_{2976}(OH)_{192}F_{288}].Cu_{40}.[H_2O]_{910}.[C_6H_{11}N_2]_{80}.[C_6H_{16}N_2]_{104}$. Without HDA in the synthesis, AlPO-11 with AEL topology structure was preferentially acquired instead of Cu/DNL-1 as shown in Figure 5.11. This also occurs when Co (II) nitrate was taken place in reaction at 210 $^oC$, which was discussed in Chapter 3. The AEL structure of AlPO-11 in the inset of Figure 5.15 has described in Section 3.4.4. The EDX elemental result showed that the molar percentage of copper obtained in the AlPO-11 material is 0%, indicating there was no copper atom present in the material. According to these results, HDA is considered as an essential co-template and co-structure directing agent (co-SDA) in crystallisation of Cu/DNL-1. However, the presence of HDA in the synthesis does not appear to help in 'fixing' the solubility of $Cu^{2+}$ ions in the solution to incorporate them into the AlPO framework, in contrast to the synthesis of CoAPO-34 (discussed in Chapter 3). It looks like HDA is important for the metal ions in all cases, where when the metal ions favor the tetrahedral coordination for example $Co^{2+}$ they go in the framework, while when they don't like tetrahedral ( e.g. $Cu^{2+}$) they prefer to reside the channels. Another reason why the copper ions were not incorporated in framework of Cu/DNL-1 is the copper ions may have been strongly restricted by chelating properties of acetate ligand, since

the copper (II) acetate is known to not function as a source of copper for incorporation into AlPOs framework.[27] However, this reason still has not been clearly established.[28]

In this study, the syntheses reaction were also carried out with free HF /and HDA. The products obtained from these syntheses were amorphous. This indicates that the presence of both HF and HDA in the synthesis reaction is important to help the nucleation process and crystallisation of Cu/DNL-1 material.

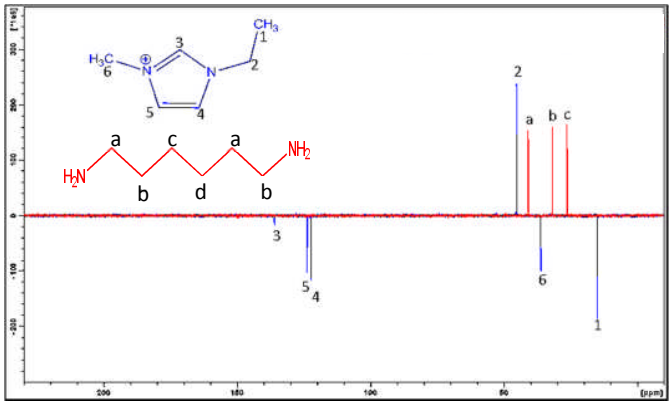


Figure 5.9: Solution $^{13}C$ DEPTQ CP/NMR spectrum of EMIMBr (blue) and HDA (red)

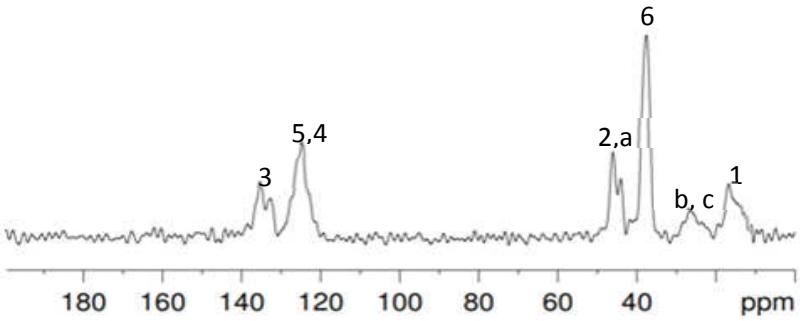


Figure 5.10: $^{13}C$ MAS/NMR spectrum of $EMIM^{+}$ and HDA in Cu/DNL-1

Table 5.2: Elemental Analysis: Carbon, Hydrogen and Nitrogen Percentage of Cu/DNL-1

| Molecular Formula | Template expected | Calculation % | | | Experiment % | | |
|---|---|---|---|---|---|---|---|
| | | C | H | N | C | H | N |
| $[Al_{768}P_{768}O_{2976}(OH)_{192}F_{288}].Cu_{40}.[H_2O]_{910}.[C_6H_{11}N_2]._{80}[C_6H_{16}N_2]_{104}$ | 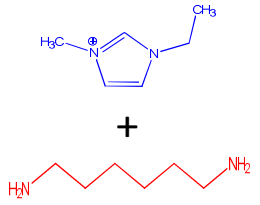 | 9.58 | 3.31 | 3.73 | 10.02 | 3.72 | 4.03 |
| $[Al_{768}P_{768}O_{2976}(OH)_{192}F_{288}].Cu_{40}.[H_2O]_{910}.[C_6H_{11}N_2]_{80}$ | 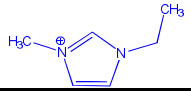 | 4.17 | 2.29 | 1.78 | | | |
| $[Al_{768}P_{768}O_{2976}(OH)_{192}F_{288}].Cu_{40}.[H_2O]_{910}.[C_6H_{16}N_2]_{104}$ |  | 5.79 | 2.84 | 2.25 | | | |

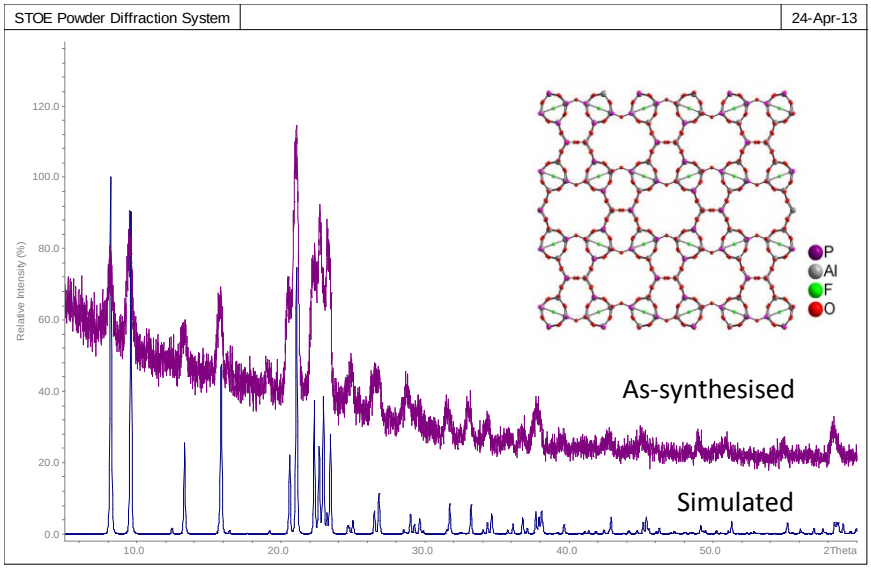


Figure 5.11: PXRD pattern of as-synthesised AlPO-11 prepared with absence of HDA, inset shows the AEL structure AlPO-11

## 5.4.3: Thermogravimetric Analysis (TGA) of Cu/DNL-1

Thermogravimetric (TG) analysis of as-synthesised Cu/ DNL-1 material has been performed at 900 $^{o}$ C. The TG curve of this material is presented in Figure 5.12 shows that the two steps of weight loss. The initial weight loss of 13.6% occurs between 25 and 300$^{o}$C is due to physically adsorbed water[29] plus water from the formula unit (cal.11.17%). The second remaining weight loss occurs between 300 and 550 $^{o}$ C is attributed to decomposition of 14.2 % of both organic templates of 1-ethyl-3-methylimidazolium and 1,6-hexadiamine accompanied with the elimination of HF per unit structure of $[Al_{768}P_{768}O_{2976}(OH)_{192}F_{288}].Cu_{40}.[H_2O]_{910}$. (cal. 15.15%)[4], This gives agreement that the both templates of $EMIM^{+}$ and HDA present in Cu/DNL-1.

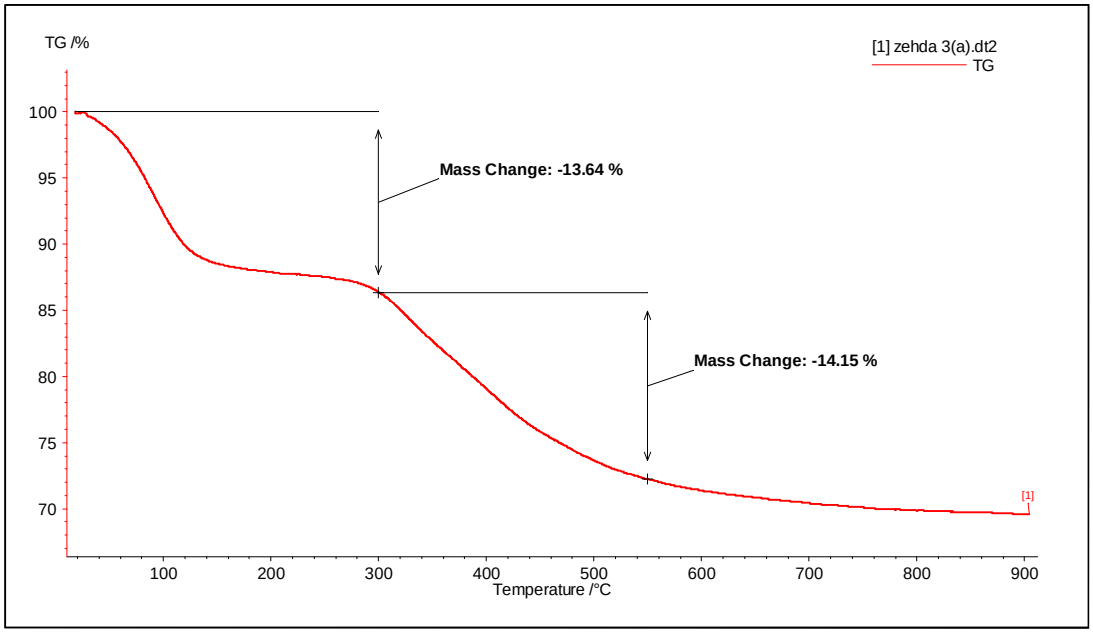


Figure 5.12: The TG curve of as-synthesised Cu/DNL-1

## 5.4.4: $^{27}$Al MAS NMR of Cu/DNL-1

Figure 5.13 (a) shows the $^{27}$Al MAS NMR spectrum of as-synthesised Cu/DNL-1. This spectrum shows that the intense resonance at 37.5 ppm is corresponding to the tetrahedral coordinated $Al(OP)_4$ in the aluminophosphate framework. The remaining of two signals at 23.5 ppm and -6.7 ppm are due to five and six coordinated aluminium, respectively, which are caused by Al interaction with fluorides ion and water. After calcination, there are three signals which appear in the spectrum of calcined sample (Figure 5.13(b)), where the first signal at 40 ppm is attributed to tetrahedral coordination of $Al(OP)_4$ while the second signal appears at -14.7 ppm is assigned to octahedral resonance which corresponding to the presence of hydrated species in the sample framework.[11, 30] This is possibly due to the sample being exposed to air. The small remaining signal appears at 17.5 ppm is suggesting that due to the five-coordinated Al that possesses linking with fluoride[11] This shows that not all the fluoride ions were removed from the sample upon calcination.

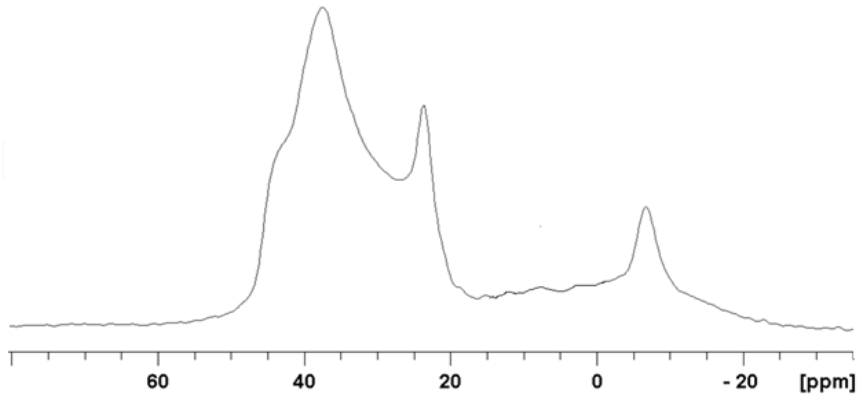


Figure 5.13 (a): $^{27}$Al MAS NMR spectrum of as-synthesized Cu/DNL-1

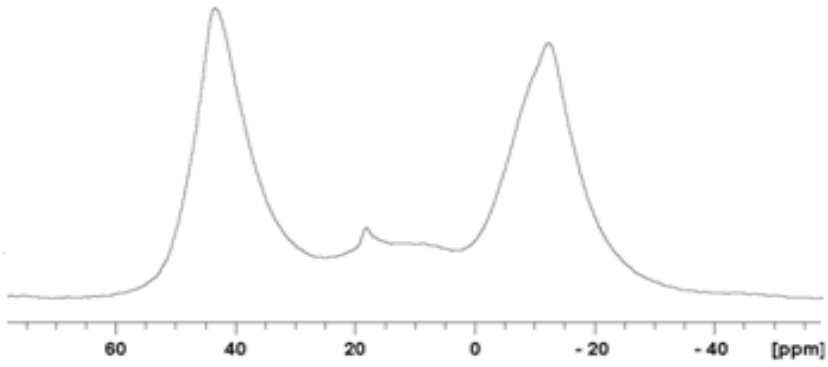


Figure 5.13 (b): $^{27}$Al MAS NMR spectrum of calcined Cu/DNL-1

## 5.4.5: $^{31}$P MAS NMR of Cu/DNL-1

Figure 5.14 (a) shows that the $^{31}$P MAS NMR spectrum of as-synthesised Cu/DNL-1. This spectrum shows that the signal appears at -11.5 ppm is corresponding to phosphorus site in the $P(OAl)_3OH$ environment in the framework while the intense resonance that appears at -18.8 ppm is attributed to $P(OAl)_4$ tetrahedral coordination. Figure 5.14(b) shows that, the $^{31}$P MAS NMR spectrum of calcined sample possesses only single broad resonance at -25.2 ppm which is assigned to tetrahedrally coordinated $P(OAl)_4$.[4] However, the line shape is rather asymmetric, indicating that the structure is perhaps not highly ordered.

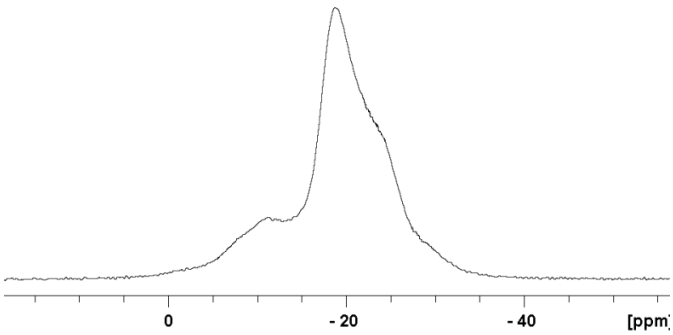


Figure 5.14 (a): $^{31}$P MAS NMR spectrum of as-synthesized Cu/DNL-1

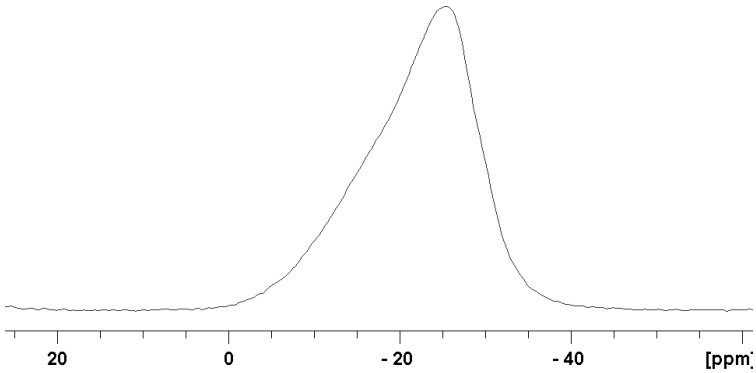


Figure 5.14 (b): $^{31}$P MAS NMR spectrum of calcined Cu/DNL-1

## 5.4.6: Broad line $^{31}$P NMR spin-echo

Figure 5.15(a) shows the $^{31}$P MAS NMR spectra of both as-synthesised and calcined Cu/DNL-1. Since the signal of pseudocontact and hyperfine interaction between unpaired electrons of paramagnetic transition metal with $^{31}$P nuclei cannot be detected by $^{31}$ P MAS NMR sequence, therefore, in this study, once again spin-echo mapping technique of $^{31}$P NMR was carried out to determine the presence of copper ions in the skeleton of Cu/DNL-1 framework, as the EDX result shows that the significant amount of copper present in this material.

Figure 5.15(b(i)) shows that the single signal that appears at δ ≈ 0 ppm results from extensive overlap of the two different phosphorus crystallographic sites of $P(OAl)_3OH$ and $P(OAl)_4$ environments in the as-synthesised Cu/DNL-1 (shown in $^{31}$P MAS NMR spectrum in Figure 5.15 (a(i)), while the single signal that appears at δ ≈ 0 ppm in the spectrum of calcined sample (shown in Figure 5.15(b(ii)) is attributed to one distinguishable type of $P(OAl)_4$ environment present in the sample (shown in $^{31}$P MAS NMR spectrum in Figure 5.15 a(ii)). Both single signals of such phosphorus environments possess very low time relaxation compared to phosphorus nuclei within $P(OAl)_{4-n}(OMe)_n$ environment.[31]

Figure 5.15(b) clearly shows that the broadline signal that attributed to phosphorus nuclei within the $P(OAl)_{4-n}(OMe)_n$ environment does not appear in both static spin-echo $^{31}P$ NMR spectra of synthesised and calcined Cu/DNL-1. Normally the chemical shift of broadline signal of $P(OAl)_{4-n}(OMe)_n$ environment emerges at > 500 ppm,[31] as demonstrated by CoAPO-34 and FeAPO-34 in Chapter 3 and 4, respectively. This suggests that the hyperfine and pseudocontact interaction between $^{31}P$ nuclei with unpaired electron from $Cu^{2+}$ ions were not present in the material, indicating that the copper ions were not bound in the AlPO skeleton framework of Cu/DNL-1. Therefore, the copper ions are expected to occupy site in the channels, and interacting with light atoms such as oxygen from non-framework or/and framework atoms,[28, 32] to form various distorted octahedral or square planar symmetries, as found in many copper containing zeolites (e.g. Cu/ZSM-5, Cu/NaA, Cu/MFI).[33-35] Burton *et.al* in 2001 have reported that the extra-framework of $Cu^{2+}$ ions in the channel of calcined copper containing AlPO-5 were present as six coordinated of $[Cu\text{-}(O)_4\text{-}(OAl/P\text{-})_2]$.[28] It is also possible for this to occur to the copper atoms in the channels of calcined Cu/DNL-1 framework. In $^{31}P$ NMR measurement, the signals are really detected from the transition metal occupying aluminum sites in MAPOs framework and do not consider the transition metal trapped within the cavities.[31] Hence, this once again gives a fact that $Cu^{2+}$ ions are only present as extra-framework cation in Cu/DNL-1 channels, indicating that the substitution between of $Al^{3+}$ with $Cu^{2+}$ ions in the Cu/DNL-1 frameworks was not successful.

Even though in principle the lattice of AlPO (Al/P =1) materials are neutral such as DNL-1, which is formed from alternating of $AlO^-$ and $PO^+$ tetrahedra, the presence of a small amount of weak acidity can also arise that may be attributed to structural imperfection.[36-38] This may be one of the possible reasons why sometimes the cations could occupy sites in the channel of AlPO framework and compensate the framework charge.

In this study, copper ions specifically Cu(I) species are present as extra-framework cation in Cu/DNL-1 cavities give an interesting of property to the material, which is able to convert $NO_2^-$ to NO. The presence of Cu(I) ions in material can be detected by NO release from the material which is discussed further in Section 5.4.11.

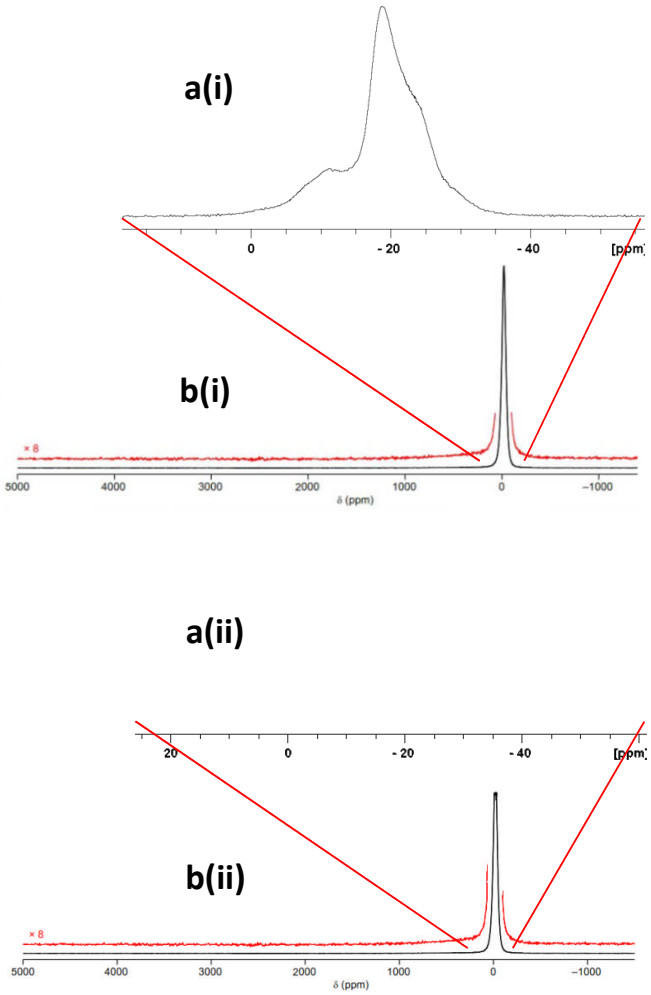


Figure 5.15: $^{31}$P MAS NMR spectrum of (a(i)) As-synthesized, (a(ii)) Calcined Cu/DNL-1 , Static $^{31}$ P spin-echo spectrum of (b(i)) as-synthesised and (b(ii) calcined Cu/DNL-1. The red line spectrum was scaled up to 8 magnifications is identical with black spectrum.

## 5.4.7: Morphology of Cu/DNL-1

SEM characterisation was carried out to observe the morphology difference between as-synthesised and calcined Cu/DNL-1. The morphology image of both samples were taken at 2000 x magnification are shown in Figure 5.16. These pictures clearly show that there is no significant difference between these two samples. These figures also show that the sample particles possess cubic shape with different sizes. According to these images, after calcination, Cu/DNL-1 not only retains its particle morphology, but it also retains its crystallinity which is confirmed by the PXRD pattern shown in Figure 5.7.

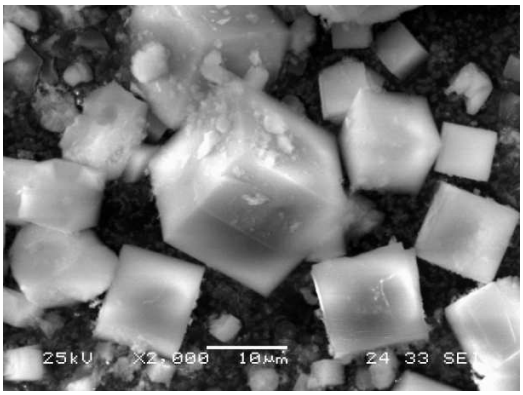


Figure 5.16 (a): SEM morphology of as-synthesised Cu/DNL-1 at x 2000 magnification

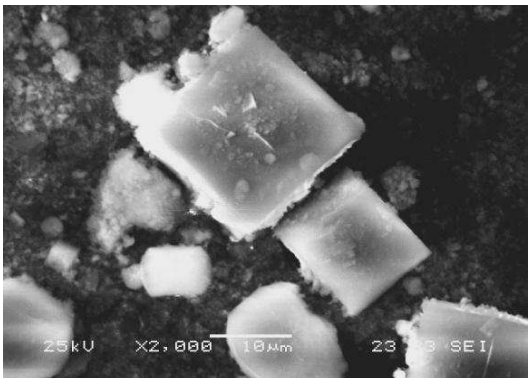


Figure 5.16 (b): SEM morphology of calcined Cu/DNL-1 at x2000 magnification

## 5.4.8: Effect of amount EMIMBr in synthesis

Initially, the preparation of Cu/DNL-1 was carried out using 26.4 g of EMIMBr. Since this amount of ionic liquid (IL) is relatively large for the synthesis, in this study the quantity of EMIMBr was reduced to different amounts, mainly reason of economy. Figure 5.17 shows the powder patterns of materials made with different amounts of EMIMBr. This figure also shows that Cu/DNL-1 material (Figure 5.17(b)) still can be obtained even when the synthesis was carried out using 20 g of EMIMBr, which saves 24% of the original amount of EMIMBr that was used. However, when the syntheses were performed using less than 20 g of ionic liquid, the amorphous products were preferentially obtained (shown in Figure 5.17(c) and (d)). It is likely when the syntheses using higher amount of IL, the mixture concentration is lower, and so the starting materials were more easily solubilized. This result is still preliminary and the synthesis work on Cu/DNL-1 is still under investigation in order to achieve more pleasant technique to form this material. In this present work the focus is more on the formation of Cu/DNL-1 and so far the amount of EMIMBr can be reduced only by 6.4 g to achieve this material.

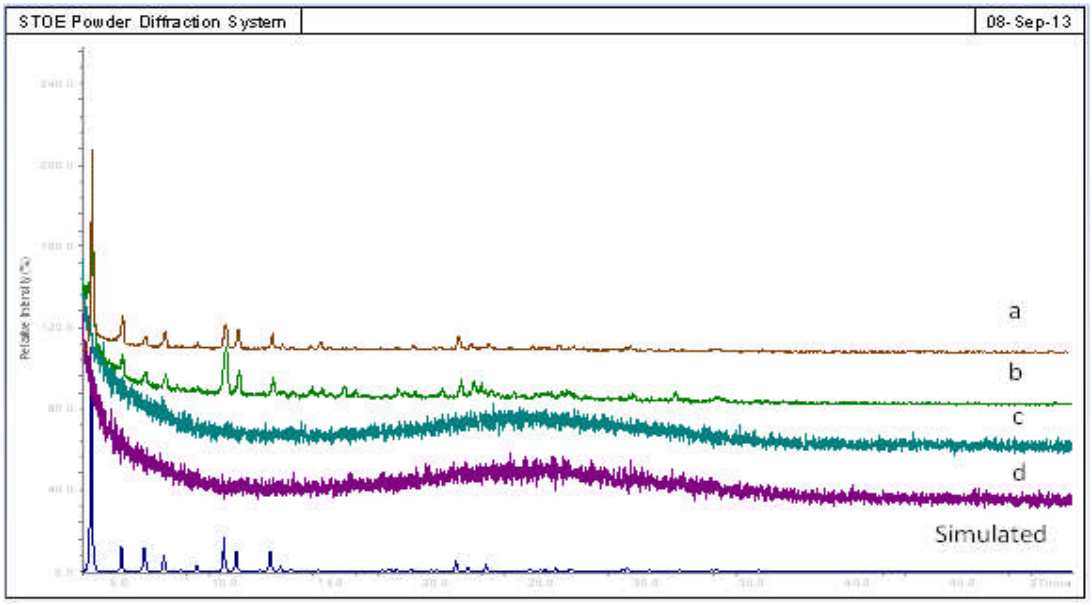


Figure 5.17: PXRD pattern of Cu/DNL-1 at different amounts of EMIMBr; (a) 26.4 g, (b) 20 g, (c) 15 g and (d) 10 g.

## 5.4.9: NO Adsorption/Desorption isotherm of Cu/DNL-1

The NO adsorption/ desorption isotherm profile of calcined Cu/DNL-1 is shown in Figure 5.18. This profile shows that the sample could adsorb a maximum 1 mmol/g of NO. When the pressure is reduced, the irreversible adsorbed NO obtained in the sample is ~0.83 mmol/g. It is more likely that the NO interacts with the extra-framework copper cations (chemisorbed) to form dinitrosyl complexes in the Cu/DNL-1. This irreversibly adsorbed NO is held relatively strongly and it is not spontaneously released from the material even at low pressure. Therefore, irreversible adsorption is such a good method of storing gas in this material since it is not easily released.[39] From this, the experimental value of irreversible adsorbed NO (0.83 mmol/g) is close to the calculated amount of NO uptake (~ 0.78 mmol/g), which is twice the amount of Cu

in calcined Cu/DNL-1 with the formula $[Al_{768}P_{768}O_{2976}(OH)_{192}]$. $Cu_{39.09}$ (0.39 mmol/g). The large hysteresis between arms of adsorption and desorption appears in the isotherm indicating the presence of strong bond between NO and metal sites in the Cu/DNL-1 material.[16]

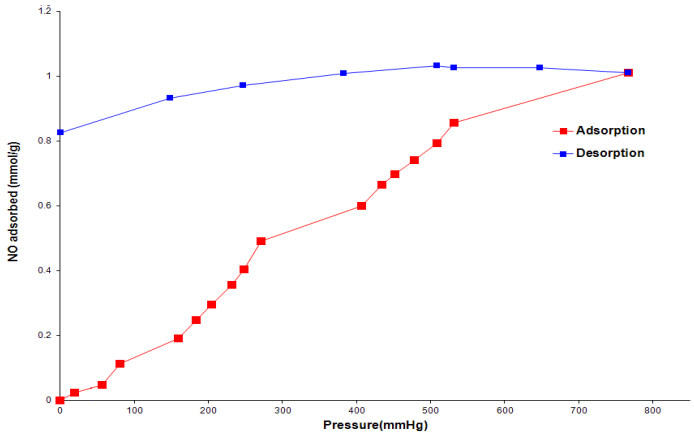


Figure 5.18: Adsorption/ desorption isotherms for NO on the calcined Cu/DNL-1. The hysteresis shape of the curve indicates an irreversible adsorption of NO within the sample

## 5.4.10: NO storage and release within Cu/DNL-1

The strategy for triggering release of NO from Cu/DNL-1 is exposure to water, which is similar technique that applied on zeolites as mentioned in Chapter 1. Water acts as nucleophile to displace NO at the copper site. Figure 5.19 (a) shows the profile of NO storage release within Cu/DNL-1. This profile shows that the NO release is a relatively short-lived burst, followed by steadily decreasing release of small amount of NO and lasting for about 60 minutes (shown in inset). Within this time the material is able to release up 3.10 x $10^{-6}$ mol NO per g of solid (shown in Figure 5.19(b)) before the reservoir of NO is completely depleted. This shows that less than 1% of stored NO was released from the material on contact with water at ambient temperature, indicating that there was still a significant amount of gas inside the material that irreversibly adsorbed even in the presence of water.[16] A similar situation also observed on NO

adsorption on zeolites such as Cu/MCM-41,[16] Cu/ZSM-5 and Cu/X,[15] as well as on some of metal organic framework (MOF) materials (e.g. HKUST-1, Ni- and Co-MOF).[40, 41] The reasoning for this could be either that steric effect prevent water from displacing NO at the copper site (structure deformation upon NO adsorption), Cu-NO adduct has a strong interaction energy[42] or that NO reacts with copper to form another species. Moreover, it also seems that the restricting step for the NO release probably due to the accessibility of water to the NO-metal cations sites and/or kinetics of diffusion within the material, suggesting that the framework topology also lead a huge influence to the rate of gas release.[39, 43, 44]

In this study, the small amount (<1%) of stored NO released might be enough for biological activity since it requires only a very low flux of NO. In healthy circulatory systems, the thrombus formation is inhibited by small quantities (approximately 1 pmol $min^{-1}$ $mm^{-2}$) of NO by the endothelial cells.[45] Morris *et.al* in 2007 have reported that the release of NO in small portion (<0.05%) from HKUST-1 was still enough to completely inhibit platelet aggregation in biological experiments. [43]

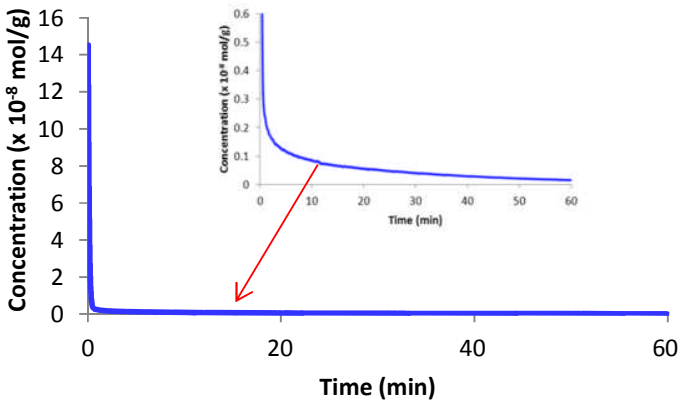


Figure 5.19 (a): NO release profile of Cu-DNL-1 loaded with nitric oxide. Inset shows the small amount of NO steadily released from the material. Inset is a zoom up the steadily decrease of NO released.

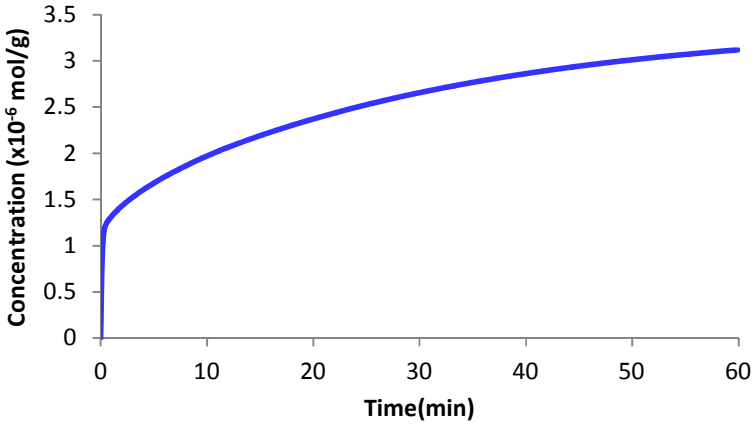


Figure 5.19 (b): Total amounts of NO released by Cu/DNL-1 within 60 minutes.

## 5.4.11: Simultaneous NO storage and NO Production Analysis using Cu/DNL-1

Even though there is a significant amount of NO released from Cu/DNL-1 is suitable for the biological applications as mentioned in Section 5.4.10, the form of NO release profile of the material, which consists of a large burst of NO and followed by steady release at very low level, is less suitable method to mimic the more constant of NO delivery from endothelial cells. The NO reservoir in the material is finite and it is difficult to replace particularly for longer-term implants. Therefore, since the copper (I) species in material which are active in transformation of $NO_2^-$ to NO (as mentioned in Section 5.1.2), in this study, such a strategy was used on Cu/DNL-1 as the aim to extend the life time delivery of NO from the gas storage material.

Initially, in this work, the analysis of the simultaneous NO storage and NO production from nitrite source was carried out using as-synthesised Cu/DNL-1 without any pre-loaded NO. Figure 5.20 shows the NO release profile of as-synthesised Cu/DNL-1. According to this profile, at the first minute, very minimal amount of NO (2.2 x $10^{-13}$ mol NO/g) was released from the material as

1.25 x $10^{-7}$ mol of sodium nitrite ($NaNO_2$) was injected into the solution. Then the graph remains steady even more amount of nitrites were added. It is assumed that the as-synthesised sample does not consist of Cu(I) ions which are involved in the production of NO from $NO_2^-$, as also found on as-synthesised Cu(II)-containing zeolites which obtained directly from ion-exchange.[15, 16] Another possible reason why as-synthesised sample was not active in producing NO is probably due to the sample does not have any space for nitrite reduced to NO as presence of templates in sample. Therefore, as-synthesised Cu/DNL-1 is suggested to be unsuitable for use in the extension of NO delivery.

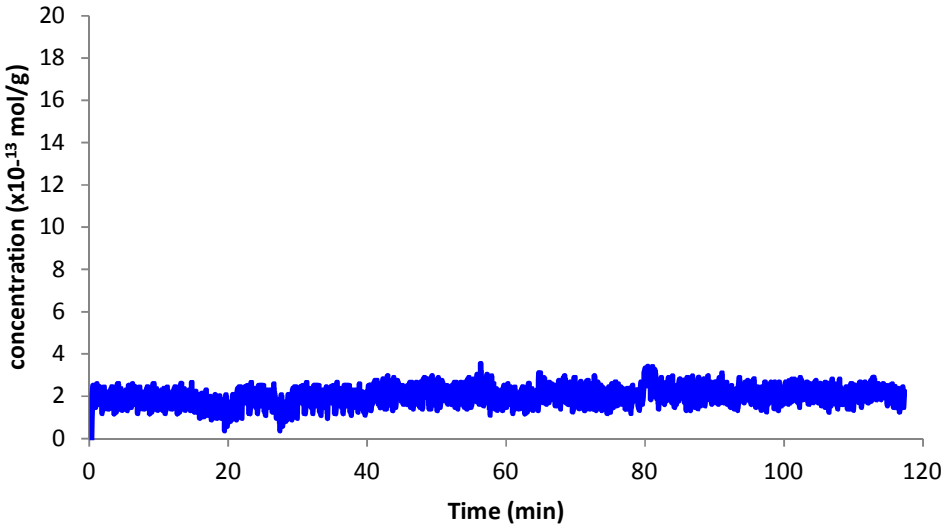


Figure 5.20: Dose-response profile of as-synthesised Cu/DNL1 releasing NO with addition of 25 µl of $NaNO_2$ (0.005 M) for every 20 minutes in 2 hours.

The NO production analysis also was carried out with addition of nitrites into solution containing calcined Cu/DNL-1 sample. Figure 5.21 demonstrates the dose-response profile of calcined Cu/DNL-1 releasing NO using two different concentrations of $NaNO_2$. This profile shows that at the first minute (Peak A) the NO was released up to 2.08 x $10^{-9}$ mol NO/g as 1.25 x $10^{-7}$ mol of $NaNO_2$ was added into the solution. This amount of NO released is much higher than that produced within the as-synthesised sample, due to more Cu(I) species have formed in the sample after treated by thermal activation at 550$^{o}$C. Hence, more $NO_2^-$ ions were reduced by Cu(I) in the material to produce NO. This is comparable with early works on calcined Cu/X, Cu/MCM-41[16] and Cu/ZSM-5[33] zeolites in releasing NO from $NO_2^-$. The reduction of $NO_2^-$ by Cu (I) can be described in equation 5.1.

$$NO_2^- + Cu(I) + 2H^+ \rightarrow NO + H_2O + Cu(II) \qquad (5.1)$$

The thermal activation of copper containing material which lead to form Cu(I) is called as 'self-reduction' reaction. Self-reduction reaction comprises several different steps as material are heated. The reaction includes a complex reorganization of the copper ion sites as the water of hydration is eliminated, then it followed by reduction from Cu(II) to Cu(I) at higher temperatures (normally beyond 473 K) and then followed by structural rearrangement to maintain neutrality.[33, 46] This is found in many copper-exchange zeolites such as Cu/ZSM-5, Cu/MCM-1, Cu/X, Cu-β and Cu/SSZ-13 upon calcination.[46]

The same profile also shows that after the initial spike (Peak A) by the first addition of $NO_2^-$, the NO release profile shows a rapid decrease to 2.76 x $10^{-10}$ mol NO/g. This is likely probably due to a depletion of either the $NO_2^-$ anions or the Cu(I) centres required to reduce the $NO_2^-$ to NO, or to a combination of both. The total amount of NO released within this time (about 20 minutes)

is 7.6 x $10^{-9}$ mol NO/g. Further additions of equimolar amounts of $NO_2^-$ at 40 and 60 minutes (Peaks B and C, respectively) also produced sharp increases in the NO release, but the amount of NO releases grew progressively lower. This indicates that most probably there were fewer Cu(I) species remaining in the sample that were able to react with $NO_2^-$. The addition of the same volume (25µl) of a nitrite solution with ten times higher concentration (0.05 M) than that used in the first three steps, producing 4.21 x $10^{-10}$ mol/g of NO (Peak D) that was significantly higher than either Peak B or C. This might be due to higher excess of nitrite leads to more chance that the few remaining Cu(I) sites will encounter an $NO_2^-$ anion to produce NO. In this profile, also shows that the decreasing trend of subsequent NO release profile of Peaks E, F and G follow a similar trend as for Peaks A, B and C. This profile also shows that the higher concentration of nitrite seems provides enough time to stabilize the delivery, giving a good sign to prolong the gas delivery.

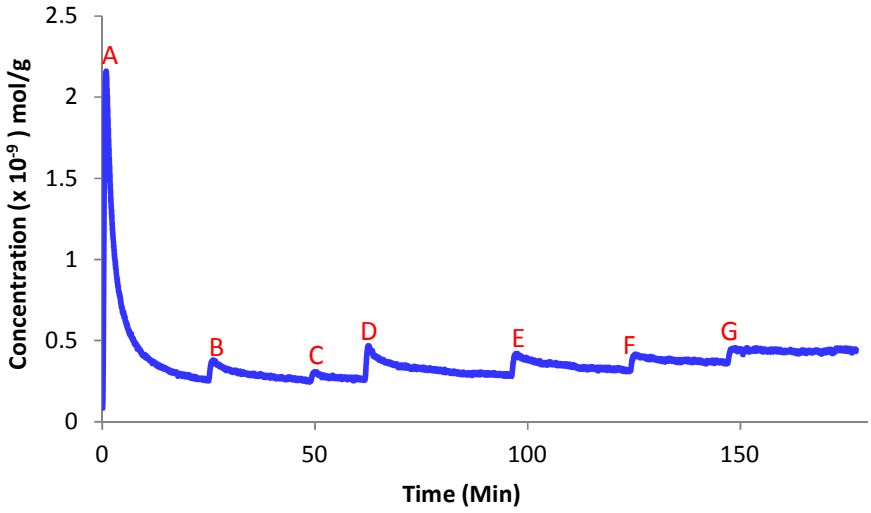


Figure 5.21: Dose-response file of calcined Cu/DNL-1 releasing NO from small concentration of $NaNO_2$. The first three steps are correspond to 25 µl of $NaNO_2$ (0.005 M) and the following steps account for 25 µl of $NaNO_2$ (0.05 M).

In this study, the dose-response measurement of NO was also monitored for calcined Cu/DNL-1 with pre-loaded NO, followed by production of NO (see Figure 5.22). According to this figure, the stored NO was released instantly (Peak A) followed by rapid decline and steadily decreasing of small amount of NO released, within 20 minutes the total amount of pre-loaded NO release is about 3.43 x $10^{-6}$ mol NO/g. To prolong the gas delivery, 1.25 x $10^{-7}$ mol of $NaNO_2$ was added into the solution, as expected, the significant amount of NO production increases immediately from 6.8 x $10^{-10}$ mol NO/g to 1.9 x $10^{-9}$ mol NO/g (Peak B), indicating that the Cu(I) species present in the material reduces $NO_2^-$ to NO. From this profile also can be observed that after the addition of nitrite into the solution on contact with pre-loaded NO in the material, the gas delivery does not decrease rapidly and remains constant longer than non-loaded NO material. The very quick deactivation of Cu(I) in non-NO loaded Cu/DNL-1 (Figure 5.22, Peak A to B) is probably due to rapid re-oxidation of Cu(I) to inactive Cu(II), as also found on Cu/ZSM-5 zeolite.[15] This kind of rapid re-oxidation requires the presence of both water and oxygen. Oxygen that is only present by itself is not sufficient to oxidise Cu(I) to Cu(II) at room temperature.[33] For the pre-loaded NO material, the lifetime conversion of nitrite to NO to be extended by Cu(I) is most probably because of the oxidation of Cu(I) to Cu(II) is restricted by the presence of the pre-loaded NO (i.e. it is clear that the re-oxidation in NO-preloaded sample (Figure 5.22, shown in inset) is much slower than non-loaded NO sample (see Figure 5.21) ). It seems that the irreversibly stored NO (the remaining of NO in the material that not released on contact with water) slows the oxidation of Cu(I) by restricting the interaction with water,[15] extending the lifetime of the Cu(I) species and NO delivery.

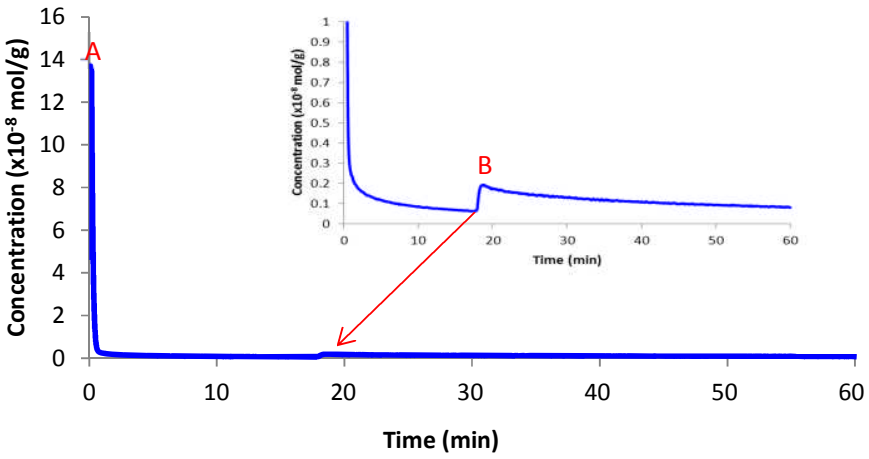


Figure 5.22: NO release profile of NO-loaded calcined Cu/DNL-1 followed by catalytic production of NO using 25µl of $NaNO_2$ (0.005M). The inset is a zoom up the second step of NO release.

In practice, the powdered sample is difficult to handle. It is more likely that the powdered porous material will be formulated into a compact form which is easier to handle (e.g. pellet, polymer and etc). To test the behavior of the NO release in this sample form, a disk pellet of calcined Cu/DNL-1 was made to check the gas delivery of stored and catalytically produced NO. The NO released profile of this experiment is shown in Figure 5.23. This profile shows that the amount of loaded NO released is about 9.26 x $10^{-7}$ mol NO/g during 20 minutes. As 25 µl of nitrite (0.005 M) was injected into the solution, the NO released increases from 3.82 x $10^{-10}$ mol NO/g to 5.75 x $10^{-10}$ mol NO/g (Peak Y). The total amount of NO released from this experiment is about 1.83 x $10^{-6}$ mol NO/g. According to these results, NO production and delivery in pellet are lower than the one obtained with powder since the accessibility to the surface area and porosity are reduced. However, this amount of NO released is satisfactory because, as

mentioned, the NO produced by endothelial cells is approximately 1 pmol $min^{-1}$ $mm^{-2}$ to inhibit thrombus formation.

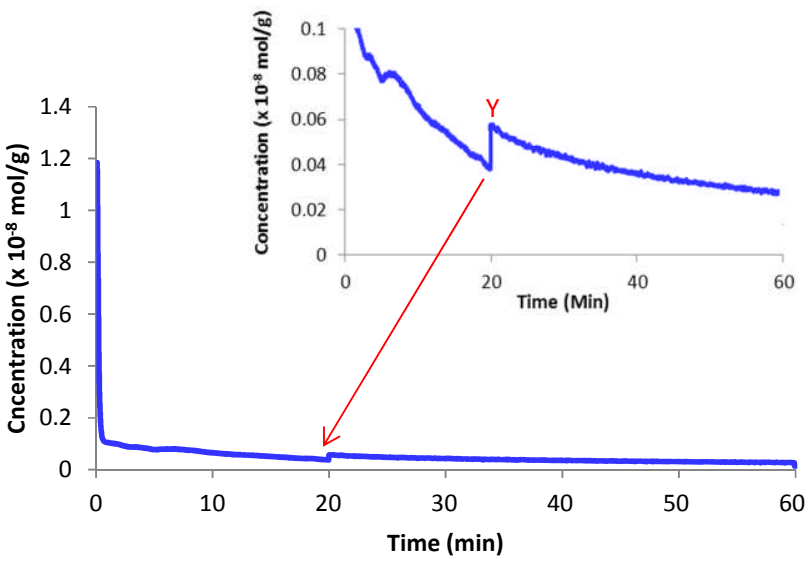


Figure 5.23: NO release profile of NO-loaded pellet made from calcined Cu/DNL-1. The first peak corresponds to the delivery of NO stored while the second peak corresponding to NO release from catalytic production by 25µL of $NaNO_2$ (0.005 M) injection. Inset a zoom up the second step of the NO release.

## 5.5: Conclusion

In summary, in this study, Cu/DNL-1 which is identical structure to DNL-1 (-CLO topology) was successfully prepared under ionothermal synthesis using of EMIMBr in the presence of HDA. The pure - CLO structure of Cu/DNL-1 was confirmed by the PXRD pattern. Without HDA in the reaction, AlPO-11 was preferentially obtained while in the absence of HF or combination of both HF and HDA, amorphous products were acquired. This indicates that the presence of HF and HDA are important additives to crystallise Cu/DNL-1. According to $^{13}C$ MAS NMR, CHN and

TGA analyses has confirmed that both templates of $EMIM^+$ and protonated HDA occluded into the Cu/DNL-1 cavities as template and co-template, respectively. After removal the templates by calcination, the structures of Cu/DNL-1 remain intact with -CLO structure and there was no significant different morphology obtained compared to as-synthesised sample, where the both samples possess cubic shape. Although HDA is important additive in order to form Cu/DNL-1, however, it was not appear to helps in 'optimising' the solubility of the $Cu^{2+}$ in the solution to incorporate in the Cu/DNL-1 skeleton framework. Thus, the copper ions are suggested to only be present as extra-framework cations located in the Cu/DNL-1 cavities. This was confirmed by the absence of the broad line signal in spin-echo $^{31}$ P NMR spectra of both as-synthesised and calcined sample, indicating that the hyperfine and pseudocontact interaction between $^{31}P$ nuclei with unpaired electron from $Cu^{2+}$ ions were not present in the material.

In this study it has been demonstrated that the extra-framework of Cu(I) species that were formed by high temperature calcination of Cu/DNL-1 are active to convert $NO_2^-$ to NO. Hence, calcined Cu/DNL-1 can be used in simultaneously storing and producing NO from nitrite source. This could potentially significantly extend the lifetime of gas delivery in the material and the amount of NO released from this material is potentially enough to prevent thrombus formation. Of course, to make use of a material as a gas storage and production medium is depending on the exact nature of the target application. However, in this study, the focus is only to test in terms of the materials that actively release NO from Cu(I)-containing aluminophosphate of Cu/DNL-1 that have potential for antithrombotic behavior. This method is an exciting example of technique that may be particularly important in some cases, for example, where it is difficult to recharge the NO in the material (coated medical devices) that remain contact in blood for an extended period (e.g. dwelling stents, catheters) to inhibit infection and/or thrombosis formation. Another exciting that can be acquired from this technique is the substrate (nitrite) that also present in blood potential to recharge NO naturally in NO-releasing materials.

Nevertheless, before the material is applied to the devices; the leaching of copper from zeolite must also be taken into account because due to the insignificant amount of copper present in the body it may be cause toxic in high doses[16] and this is still under investigation.

## 5.6: References


1. M. E. Davis, C. Montes, J. Garces and C. Crowdert, *Nature*, 1988, **331**, 698 - 699.
2. M. E. Davis, *Nature*, 2002, **417**, 813-821.
3. J. Sun, C. Bonneau, Á. Cantín, A. Corma, M. J. D. Cabañas, M. Moliner, D. Zhang ,M. Li and X. Zou, *Nature*, 2009, **458**, 1154-1157.
4. Y. Wei, Z. Tian, H. Gies, R. Xu, H. Ma, R. Pei, W. Zhang, Y. Xu, L. Wang, K. Li, B. Wang, G. Wen and L. Lin, *Angewandte Chemie International Edition*, 2010, **49**, 5200-5200.
5. M. E. Davis, C. Montes, P. E. Hathaway, J. P. Arhancet, D. L. Hasha and J. M. Garces, *Journal of the American Chemical Society*, 1989, **111**, 3919-3924.
6. M. E. Davis, C. Montes, P. E. Hathaway and J. M. Garces, *Studies in Surface Science and Catalysis*, Elsevier, 1989, **49**, 199-214.
7. B. Duncan, R. Szostak, K. Sorby and J. G. Ulan, *Catalysis Letters*, 1990, **7**, 367-375.
8. H. X. Li and M. E. Davis, *Journal of the Chemical Society, Faraday Transactions*, 1993, **89**, 957-964.
9. Ch. Baerlocher and L.B. McCuster, *Database of Zeolite Structures*:*http://www.iza-structure.org/databases/*.
10. R. H. Jones, J. M. Thomas, J. Chen, R. Xu, Q. Huo, S. Li, Z. Ma and A. M. Chippindale, *Journal of Solid State Chemistry*, 1993, **102**, 204-208.
11. Y. Wei, H. Gies, Z. Tian, B. Marler, Y. Xu, L. Wang, H. Ma, R. Pei, K. Li and B. Wang, *Inorganic Chemistry Communications*, 2010, **13**, 1357-1360.
12. M. Estermann, L. B. Mccusker, C. Baerlocher, A. Merrouche and H. Kessler, *Nature*, 1991, **352**, 320 - 323.
13. G. A. Deluga, J. R. Salge, L. D. Schmidt and X. E. Verykios, *Science*, 2004, **303**, 993-997.

14. B. K. Oh and M. E. Meyerhoff, *Biomaterials*, 2004, **25**, 283-293.

15. A. K. Boes, P. S. Wheatley, B. Xiao, I. L. Megson and R. E. Morris, *Chemical Communications*, 2008, 6146-6148.

16. A. K. Boës, B. Xiao, I. Megson and R. E. Morris, *Topics in Catalysis*, 2009, **52**, 35-41.

17. R. K. Aggarwal, D. C. Ireland, M. A. Azrin, M. D. Ezekowitz, D. P. de Bono, and A. H. Gershlick, *Circulation*, 1996, **94**, 3311-3317.

18. E.P. Strecker, A. Gabelmann, I. Boos, C. Lucas, Z. Xu, J. Haberstroh, N. Freudenberg, H. Stricker, M. Langer and E. Betz, *CardioVascular and Interventional Radiology*, 1998, **21**, 487-496.

19. E. M. Hetrick and M. H. Schoenfisch, *Chemical Society Reviews*, 2006, **35**, 780-789.

20. J. H. Shin and M. H. Schoenfisch, *Analyst*, 2006, **131**, 609-615.

21. I. M. Wasser, S. de Vries, P. M. Loccoz, I. Schroder and K. D. Karlin, *Chemical Reviews*, 2002, **102**, 1201-1234.

22. M. Kujime and H. Fujii, *Angewandte Chemie International Edition*, 2006, **45**, 1089-1092.

23. A. Burg, E. Lozinsky, H. Cohen and D. Meyerstein, *European Journal of Inorganic Chemistry*, 2004, **2004**, 3675-3680.

24. I. M. Wasser, S. de Vries, P. M. Loccoz, I. Schroder and K. D. Karlin, *Chemical Reviews*, 2002, **102**, 1201-1234.

25. Y. Zhao, D. A. Lukoyanov, Y. V. Toropov, K. Wu, J. P. Shapleigh and C. P. Scholes, *Biochemistry*, 2002, **41**, 7464-7474.

26. S. V. Antonyuk, R. W. Strange, G. Sawers, R. R. Eady and S. S. Hasnain, *Proceedings of the National Academy of Sciences of the United States of America*, 2005, **102**, 12041-12046.

27. T. Munoz, A. M. Prakash, L. Kevan and K. J. Balkus, *The Journal of Physical Chemistry. B*, 1998, **102**, 1379-1386.

28. I. D. Burton, J. S. J. Hargreaves, D. G. Nicholson, M. H. Nilsen and M. Stockenhubera, *Journal of Materials Chemistry*, 2001, **11**, 1441-1446.

29. M. Karthik, A. Vinu, A. K. Tripathi, N. M. Gupta, M. Palanichamy and V. Murugesan, *Microporous and Mesoporous Materials*, 2004, **70**, 15-25.

30. N. Rajić, A. Ristić, A. Tuel and A. Kaučič, *Zeolites*, 1997, **18**, 115-118.

31. G. Mali, A. Ristić and V. Kaućić, *The Journal of Physical Chemistry B*, 2005, **109**, 10711-10716.

32. D. G. Nicholson and M. H. Nilsen, *Journal of Materials Chemistry*, 2000, **10**, 1965-1971.

33. G. T. Palomino, P. Fisicaro, S. Bordiga and A. Zecchina, *The Journal of Physical Chemistry. B*, 2000, **104**, 4064-4073.

34. H. So, K. Ha, Y.J. Lee, K. B. Yoon and R. L. Belford, *The Journal of Physical Chemistry. B*, 2003, **107**, 8281-8284.

35. H. Yahiro and M. Iwamoto, *Applied Catalysis A: General*, 2001, **222**, 163-181.

36. N. J. Tapp, N. B. Milestone and D. M. Bibby, *Studies in Surface Science and Catalysis*, Elsevier, 1988, 37, 393-402.

37. C. Halik, J. A. Lercher and H. Mayer, *Journal of the Chemical Society, Faraday Transactions 1: Physical Chemistry in Condensed Phases*, 1988, **84**, 4457-4469.

38. G. Dworezkov, G. Rumplmayr, J. Lercher and H. Mayer, *Studies in Surface Science and Catalysis*, Elsevier, 1985, **21**, 163-172.

39. P. S. Wheatley, A. R. Butler, M. S. Crane, S. Fox, B. Xiao, A. G. Rossi, I. L. Megson and R. E. Morris, *Journal of the American Chemical Society*, 2006, **128**, 502-509.

40. B. Xiao, P. S. Wheatley, X. Zhao, A. J. Fletcher, S. Fox, A. G. Rossi, I. L. Megson, S. Bordiga, L. Regli, K. M. Thomas and R. E. Morris, *Journal of the American Chemical Society*, 2007, **129**, 1203-1209.

41. A. C. McKinlay, B. Xiao, D. S. Wragg, P. S. Wheatley, I. L. Megson and R. E. Morris, *Journal of the American Chemical Society*, 2008, **130**, 10440-10444.

42. S. Bordiga, L. Regli, F. Bonino, E. Groppo, C. Lamberti, B. Xiao, P. S. Wheatley, R. E. Morris and A. Zecchina, *Physical Chemistry Chemical Physics*, 2007, **9**, 2676-2685.

43. B. Xiao, P. S. Wheatley, X. Zhao, A. J. Fletcher, S. Fox, A. G. Rossi, I. L. Megson, S. Bordiga, L. Regli, K. M. Thomas and R. E. Morris, *Journal of the American Chemical Society*, 2007, **129**, 1203-1209.

44. P. S. Wheatley, A. C. McKinlay and R. E. Morris, *Studies in Surface Science and Catalysis*, Elsevier, 2008, **174**, 441-446.

45. L. K. Keefer, *Nature Materials*, 2003, **2**, 357 - 358.

46. F. Giordanino, P. N. R. Vennestrøm, L. F. Lundegaard, F. N. Stappen, S. Mossin, P. Beato, S. Bordiga and C. Lamberti, *Dalton Transactions*, 2013, **42**, 12741-12761.

# CHAPTER 6

# CONCLUSION AND FUTURE WORK

## 6.1: Conclusion

In this study, CoAPO-34 and FeAPO-34 have been successfully prepared under ionothermal synthesis in the presence of amine either HDA or EDA, which is demonstrated in Chapter 3 and Chapter 4, respectively. This indicates that CoAPO-34 and FeAPO-34 can be prepared under low pressure instead of higher pressure associated with hydrothermal or solvothermal synthesis. Although both materials have CHA topology, they were formed using different ionic liquids and organic amines. CoAPO-34 is formed using 1-ethyl-3-methylimidazolium bromide (EMIMBr) with presence of HDA, while FeAPO-34 is formed using 1-ethyl-3-methylimidazoliumchloride (EMIMCl) with addition of EDA.

The incorporation of $Co^{2+}$ and $Fe^{2+}$ into CoAPO-34 and FeAPO-34 skeleton frameworks, respectively, were confirmed by broad line signal that appear at > 500 ppm in spin-echo $^{31}P$ NMR spectrum. The broadline signal belongs to phosphorus in the $P(OAl)_3(OMe)$ environment, (Me= $Co^{2+}$ or $Fe^{2+}$), attributed to the hyperfine interaction between unpaired electrons from the transition metals ions ($Co^{2+}$ or $Fe^{2+}$) and phosphorus nucleus.[1]

In the CoAPO-34 framework, $EMIM^+$ is present as a template in the channels, while HDA acted as co-structure directing agent (SDA). In the absence of HDA, AlPO-11 was preferentially formed rather than CoAPO-34. In FeAPO-34, $DMIM^+$ was occluded as template in the cavities. Without EDA in the synthesis, AlPO-34 was preferentially obtained. As described in Chapter 3 and 4, the presence of HDA and EDA are important in the formation CoAPO-34 and FeAPO-34,

respectively. Both amines seem to help in 'fixing' the solubility of $Co^{2+}$ and $Fe^{2+}$ in the solution in order to incorporate these metal ions into the skeleton framework CoAPO-34 and FeAPO-34, respectively.

This study also found that HF is an important additive in the formation of CoAPO-34 and FeAPO-34. Without HF in the synthesis of CoAPO-34, the amorphous product was obtained, whilst in the HF free synthesis of FeAPO-34, the 2D layered structure of SIZ-6 material was obtained.

According to the SEM characterisation, CoAPO-34 particles formed in variety of shapes and the most common being cubic, while the FeAPO-34 particles have no consistent shape or size. After calcination, no change in morphology was observed for either. This study found that the particle size of FeAPO-34 is larger than CoAPO-34.

In Chapter 5, Cu/DNL-1 was successfully prepared under ionothermal condition using EMIMBr in the presence of HDA. Both $EMIM^{+}$ and protonated HDA templates were occluded in CuDNL-1 channels. Without HDA in the synthesis, AlPO-11 was preferentially obtained. In this study has found that the broad line signal were absence in both $^{31}P$ NMR of spin- echo spectra of as-synthesised and calcined Cu/DNL-1. This indicates that the copper ions were not incorporated into the AlPO skeleton framework of Cu/DNL-1. Based on the EDX analysis, it is expected that the copper ions are present as extra-framework cations in the Cu/DNL-1 cavities. In addition, this chapter has also demonstrated that the calcined Cu/DNL-1 containing Cu(I)species is simultaneously active in storing NO and producing it catalytically from a nitrite source. This has the potential to significantly extend the lifetime of gas delivery in the material.

## 6.2: Future work

The present work has shown that $Co^{2+}$ and $Fe^{2+}$ ion have been successfully incorporated into CoAPO-34 and FeAPO-34 frameworks, respectively, under ionothermal conditions in the presence of amines. Similar conditions were used to incorporate silicon into the AlPO framework to form SAPO, however only unreacted silica (Chapter 3, Section 3.5.3) or an amorphous solid (Chapter 4, Section 4.4.3) was obtained . This problem is primarily due to the poor solubility of silica starting material in ionic liquid (IL) solution of EMIMBr or EMIMCl. Therefore, for future studies, using ILs that contains a hydroxide anion, for example EMIMOH, is suggested for use in the synthesis which would be expected to have better chemistry suited to the dissolution of silica, resulting in production of SAPO material. ILs containing hydroxide anion are chosen because their chemistry mimics traditional hydrothermal synthesis. The first silica based material was successfully synthesised using an IL containing a hydroxide anion is siliceous zeolite, reported by Morris *et.al* 2010.[2] This material was prepared using 1-butyl-3-methylimidazolium hydroxide.

In Chapter 5, ionothermal synthesis and characterisation of Cu/DNL-1 were discussed. Since the Cu(I) species in Cu/DNL-1 are responsible for the production of NO from $NO_2^-$, it would be interesting for the future study to investigate the behavior, location and interaction of the extra-framework copper ions ($Cu^+$ and $Cu^{2+}$) with the local environment of Cu/DNL-1. These characteristics can be characterised using Electron Spin Resonance.

Cysteine is among of amino acids that present in human blood plasma.[3] It is naturally produced from biosynthesis reaction in the human body and has ability to reduce Cu(II) to Cu(I).[4] This gives an avenue idea for future study to make a series of experiments which are biologically relevant by involving cysteine to chemically reduce Cu(II) to Cu(I) in Cu/DNL-1, producing NO from $NO_2^-$. Morris and co-workers have demonstrated that the addition of cysteine into

suspension of Cu/MCM-1 in aqueous $NaNO_2$ led to higher production of NO, indicating that Cu(II) was reduced to Cu(I) by cysteine.[5] This technique is potentially to be used for longer term implant since both of Cu(I) and $NO_2^-$ that involve in simultaneous storage and catalytic production of NO can be recharged naturally when contact with blood.

## 6.3: References


1. G. Mali, A. Ristić and V. Kaučić, *The Journal of Physical Chemistry B*, 2005, **109**, 10711-10716.
2. P. S. Wheatley, P. K. Allan, S. J. Teat, S. E. Ashbrook and R. E. Morris, *Chemical Science*, 2010, **1**, 483-487.
3. M. P. Brigham, W. H. Stein and S. Moore, *The Journal of Clinical Investigation*, 1960, **39**, 1633-1638.
4. L. Pecci, G. Montefoschi, G. Musci and D. Cavallini, *Amino Acids*, 1997, **13**, 355-367.
5. A.K. Boës, B. Xiao, I. L. Megson and R. E. Morris, *Topics in Catalysis*, 2009, **52**, 35-41.